Supersymmetry Search in Multilepton Final States with Taus Using the CMS Detector at the LHC

By

Sho Maruyama

B.S. (University of California, Davis) 2005

DISSERTATION

Submitted in partial satisfaction of the requirements for the degree of

DOCTOR OF PHILOSOPHY

in

Physics

in the

OFFICE OF GRADUATE STUDIES

of the

UNIVERSITY OF CALIFORNIA

DAVIS

Approved:

Maxwell Chertok, Chair

John Conway

Mani Tripathi

Committee in Charge

2011

Abstract

This dissertation presents a search for SUperSYmmetry (SUSY) in multilepton final states with a data set corresponding to 34.9 pb^{-1} collected in 2010 with the Compact Muon Solenoid (CMS) detector at the Large Hadron Collider (LHC) running at a center-of-mass energy of 7 TeV. The analysis channels contain combinations of at least three leptons: electrons, muons, and hadronically decaying taus that are reconstructed using a particle-flow technique. The minimal SUperGRAvity (mSUGRA) model and co-Next-to-the-Lightest-SUSY-Particle (co-NLSP) scenario in the Gauge-Mediated SUSY Breaking (GMSB) model are considered. To identify SUSY signal events, signal and Standard Model (SM) background processes are studied with full detector simulation and systematics uncertainties are evaluated. Relevant SM backgrounds include Z boson + jets, diboson, $t\bar{t}$, and QCD processes. The separation between the signal and background is performed using a cut-based selection. Good agreement between simulated samples and data is obtained, in particular for the significant Z boson + jets background. With the chosen event selection, we observe three events in data, consistent with the SM prediction within statistical fluctuations. Therefore, we set exclusion limits on both models using Bayesian statistics. For the SUSY parameters of m_0 = 60 GeV, A_0 = 0, $tan\beta$ = 3, and $\mu >$ 0, chargino masses below 163 GeV are excluded in the mSUGRA model. In GMSB, gluino masses up to 1040 GeV are excluded in co-NLSP scenario.

Acknowledgments

I would like to express my gratitude to Maxwell Chertok, who has been an excellent supervisor, and has supported me in every way since my senior year in undergraduate. He has been a real inspiration for taking a creative and innovative approach in high energy experiments like CMS at the LHC. I have also benefited from his policy of providing his students with the opportunity to study at laboratories: meeting a wide variety of people in the field has definitely been a great help to me.

Within our group at U.C. Davis, I would like to thank: John Conway, Robin Erbacher, Richard Lander, Mani Tripathi, John Gunion, Joseph Kiskis, and Hsin-Chia Cheng who taught me a lot about high energy physics; Sasha Baroiant, Ricardo Vasquez, and Christian Veelken who guided me in researches. I have also been benefited indirectly from David Pellett, Richard Breedon, Timothy Cox, John Smith, Maria Borgia, Sushil Singh Chauhan, Tia Miceli, James Dolen, Alexandra Kopecky, Evan Friis, Michael Squires, Stanley Forrester, Robert Forrest, Charles Cox, David Cox, Paulo Afonso, Juan Lizarazo, Peter Marleau, and John Stilley in various ways. I feel indebted to Laura Peterson who has done extra paper work for me while I was away from the main campus and on filing fee status.

There are many people who have helped me on my way here: Enrique Izaguirre who was the leader of my first research group; Brock Weiss and David Webb who were my undergraduate advisers and made practical suggestions on Ph.D. programs; Maxwell Chertok and Mani Tripathi who supervised my undergraduate thesis.

I have met great people while I was away from Davis as well: Alexei Safonov and Chi Nhan Nguyen who worked with me on level 1 tau trigger while I was at FNAL; the WBM team – Kaori Maeshima, William Badgett, Juan Lopez Perez, Aron Soha, Balys Sulmanas, Zongru Wan, and Irakli Chakaberia – to which I have belonged for years; Simone Gennai who invited me to Scuola Normale Superiore di Pisa to work on the level 2 tau trigger; Massimiliano Chiorboli and Alexander Tapper who gave me practical advices on SUSY trigger work.

FNAL and LPC staffs –Terry Read, Carrie Farver, Tami Kramer, Tina Vernon, Yasemin Uzunefe-

Yazgan, Jacqueline Cyko, Patrick Gartung, and Eric Vaandering – were always kind and helpful. They definitely deserve to be mentioned.

I would also like to thank my other friends with whom were always fun to hang out: William Johnson who lived with me and went out together while I was at FNAL; Michael Case and Mikhail Makouski who lived with me and cooked together while I was in one of the LPC Houses; Tia Miceli, James Dolen, and Alexandra Kopecky who lived with me in Saint Genis-Pouilly, France; Souvik Das who was someone like me working until three a.m. in a CERN office even on Christmas Day; Piyabut Burikham, Tutanon Sinthuprasith, Kittikul Kovitanggoon, and Chuanzhe Lin who partied with me in Geneva; Aron Soha's cat Verity, Kaori Maeshima's cat Sam and dog Foxy, and my mother's dog Hal who always enlightened my gloomy day.

Several other groups contributed to the SUSY multilepton searches with the CMS detector. I would like to thank: the University of California at Santa Barbara group, Finn Rebassoo and David Stuart who worked on the Configurable Analysis (cfA) ntuples which provided a common ground for cross check among different analysis codes; Sanjay Padhi from University of California at San Diego who produced SUSY parameter scan files which provided meaningful comparison with other experiments like those at LEP and the Tevatron; the University of Colorado group, Chris Edelmaier, William Ford, and James Smith who performed an important cross check; the Rutgers University group, Richard Gray, Dmitry Hits, Steve Schnetzer, Sunil Somalwar, and Scott Thomas who performed a check and brought a different perspective; the Karlsruhe Institute of Technology group, Wim de Boer, Martin Niegel, Fedor Ratnikov, and Valery Zhukov who performed finer SUSY parameter scan. The participation of the Colorado, Karlsruhe, and Rutgers groups was critical in getting the multilepton analysis approved by the CMS collaboration.

Finally, I would like to dedicate this dissertation to my parents: my mother who always wanted me to be an engineer; my father who always wanted me to be a geologist and told me I should move to U.S. if I was serious about science. I hope they will be proud of their son on completion of this dissertation, because I could not come this far without their advice and support.

Contents

1 Brief Introduction

This dissertation is to find an experimental evidence of yet undiscovered theory, the SUper-SYmmetry (SUSY) at the LHC. Such a discovery may be archived by studying various final states with different advantages and disadvantages. In particular, this dissertation focuses on multilepton final states, mainly because its experimental cleanness. The models considered in the analysis are shortly reviewed here and then the structure of the dissertation is given at the end of this section.

In the minimal Supergravity (mSUGRA) and Gauge Mediated Supersymmetry Breaking (GMSB) models, the sleptons, lighter chargino, and lighter neutralinos typically are less massive than the gluinos and squarks. These lighter states have substantial decay widths to leptons, along with neutrinos and the Lightest SUSY Particles (which are often lightest neutralinos). Thus, a promising mode for Supersymmetry discovery at hadron colliders is that of strongly-produced gluino and squark pairs, with cascades leading to multilepton events along with substantial jet activity and $E_{\mathrm{T}}^{\mathrm{miss}}$ from the non-interacting LSPs and neutralinos. These are rare signatures with the benefit of very low Standard Model (SM) backgrounds.

In the case of high $\tan\beta$ SUSY, the lighter supersymmetric tau ($\widetilde{\tau}_1$) becomes light and can greatly enhance the branching ratios of the gauginos into taus. Indeed, multitau events dominate in certain regions of parameter space, while produced mixtures of the lepton types are also prevalent. Due to the tau's instability, e's, μ's, and hadronic tau decays are reconstructed in the final state, where the latter requires dedicated techniques. Hadronic tau decays are analyzed using the CMS particle-flow algorithm. This analysis searches for events containing at least three leptons in the data from the first run of the LHC, at $\sqrt{s} = 7$ TeV. Electrons, muons, and hadronic tau decays are used to maximize the reach for a variety of SUSY scenarios.

This dissertation is divided into four parts: theoretical foundation, experimental apparatus, event reconstruction, and analysis. The theoretical foundation consists of an introduction to the SM, and the new physics under study: mSUGRA and GMSB in Sec. 2. Then, the experimental setup is reviewed containing three parts: the LHC, the CMS, reconstruction of high level

physics objects, in Sec. 3 and 4. The detector simulation and MC event generation are outlined in Sec. 5.1 and 5.1.1. The main aspect of this dissertation, the analysis is presented in Sec. 5.

1.1 Units and Conventions

In the theory chapter, natural units are used which are defined by setting $\hbar = c = 1$. However, SI units (like cm, $Tesla$, and $1/s = Hz$) may be used in the detector chapter. With the natural units, energy, mass, momentum, time, and length are measured in the following dimensions of electron Volt: $[energy] = [mass] = [momentum] = [time]^{-1} = [length]^{-1} =$ eV where 1 eV is the energy gain of an electron traversing a potential difference of 1 Volt.

Furthermore where not specified otherwise, the following conventions are used: $Z^0 = Z$, $W^{\pm} = W$, lepton = anti-lepton ($i.e.$, $e\bar{e} = ee$) depending on its context.

The transverse momentum and missing transverse energy are written as p_T, and $E_{\mathrm{T}}^{\mathrm{miss}}$ respectively, where the transverse direction is the direction perpendicular to the beam line. In experimental high energy physics, $\Delta R = \sqrt{\eta^2 + \phi^2}$ is commonly used as a distance between two objects. The detail is given in the detector Sec. 3.

2 Theoretical Foundations

In this chapter, the Standard Model (SM) is briefly reviewed first. An emphasis is on its group theoretical structure although the SM, like most theories, has parameters which must be set by experimental results. As a matter of fact, usually what experimentalists are interested in is not the group theoretical structure itself but its particle contents and the resulting phenomenology. The particle content of the SM is reviewed first and then the local gauge theories are reviewed. SUSY models are reviewed briefly as a 'natural' extension to the SM. Most of ideas and concepts are re-used from the SM part.

The section is mostly following references [1, 2, 3, 4, 5].

2.1 The Standard Model

The Standard Model (SM) is regarded as one of the main achievements in physics of the last century. It successfully describes the electromagnetic, weak, and strong interactions, with high accuracy and stands numerous experimental tests, for example, LEP electroweak measurements.

2.1.1 Particles

An elementary particle can be defined as a point-like object. The particle is point-like in a sense it does not have any internal substructure. There are two types of spin-1/2 fermions that are elementary particles: quarks and leptons. The quarks are never observed alone but in groups of two or three, mesons and baryons respectively. Proton (uud) and neutron (udd) are widely known as basic building blocks of atoms. All other combinations form a zoo of particles, which are formed in processes of sufficiently high energy and decay quickly according to their short life times. This is clearly different from the case of leptons which do not form lots of stable bound states with other leptons.

The leptons form two groups of different character; electrically charged and massive, and electrically neutral and massless (or at least much lighter than the other massive ones). The lightest charged massive one is the electron, which is stable and an important ingredient of atoms. The other two electrically charged massive ones, muon and tau, decay into other particles. Three electrically neutral neutrinos, which can penetrate deeply though most of matter without interacting with its surroundings at all, and have a special trait of transforming into another. Mixing is considered as an evidence of massive neutrinos. The reason of its weak interacting nature can be attributed to its neutral electric charge. However it carries another type of charge, weak isospin, and thus it interacts with other particles weakly. The fermions, quarks and leptons, form baryonic matters.

There are four kinds of interactions between these particles realized as the gravitational, weak, electromagnetic, and strong forces. The SM describes three of the four forces, and the exception is gravity which was the first one studied in detail by human beings and yet resists against quantization as of today. A force is mediated by bosons between particles which have certain charge: the electric, color, and weak, for the electromagnetic, strong, and weak force respectively. The force carriers are graviton, photon, massive vector bosons, and gluons for the gravitational, electromagnetic, weak, and strong forces respectively. The strength of the four forces presented in coupling strengths are shown in Table 1.

force type	relative strength	range $[m]$	carrier
strong	1	10^{-15}	gluons(g)
electromagnetic	10^{-2}	∞	photon(γ)
weak	10^{-13}	10^{-18}	W and Z
gravitational	10^{-38}	∞	graviton

Table 1: Properties of the four forces. Approximate effective ranges and relative strengths at low energy are listed. A graviton has never been observed, but motivated by quantum gravity.

Gravity is different from other forces in terms of charge. Gravity can couple to mass, which is an equivalent to energy and thus it affects all particles. However, its strength is much smaller with respect to other forces. And thus it is negligible in high Transverse Momentum (p_T) physics at colliders like the LHC. In this dissertation, the effect of gravity is completely ignored.

The weak force affects all fermions except right-handed neutrinos. This comes from experi-

mental results ($i.e.$, no right-handed neutrino ever observed) rather than theoretical demands. In high energy scale, the electromagnetic and weak forces can be unified as the electroweak force.

The weak interaction is so short range due to its massive boson as force carrier. The strong force is also short range for a different reason: its force carriers self-interact with other gluons because they carry non-zero color charge. Both the gravitational and electromagnetic forces have infinite interaction range as their potential decreases as inverse of distance from charged object.

The forces except gravity, can be described by local gauge theories (and that is the SM), wherein the interactions are mediated by spin-1 gauge bosons. Gravity may be described by spin-2 boson, although no evidence of such a particle yet observed. Local gauge theories are reviewed in the next section.

All the four forces are experienced either directly or indirectly every day.

- Gravity: an apple falling down to ground, and beautiful movements of celestial bodies observed at night
- Strong force: binding quarks into a nucleon (via strong interaction), and nucleons to nuclei (via residual strong interaction); a mystery before studies of the strong force ($i.e.$, why neutrons are bound together?)
- Electromagnetic force: telecommunication devices and technologies, ranging from a classic vacuum tube radio to high speed internet using optical cables, and binding nuclei and electrons to form atoms
- Weak force: decay of radioactive materials like natural radon gas as a health hazard, scintigraphy which is a two-dimensional imaging technique commonly used in hospital for diagnosis, and the first step of the nuclear fusion reaction that fuels the Sun

As stated above, baryonic matter is made of fermions, and force carriers are bosons. A noteworthy feature of the SM is this role assignment to a fermion and boson. It seems there is no

obvious theoretical reason to treat a fermion and boson this way. This fundamental question is revisited in the SUSY section below. The elemental particles' properties are summarized in Table 2.

fermion family	up-type quark	down-type quark	charged lepton	neutral lepton
1^{st} generation	u (2 MeV)	d (5 MeV)	e (511 MeV)	ν_e
2^{nd} generation	c (1.25 GeV)	s (95 MeV)	μ (106 MeV)	ν_μ
3^{rd} generation	t (172.5 GeV)	b (4.2 GeV)	τ (1.78 GeV)	ν_τ
electric charge	2/3	-1/3	-1	0
boson	γ (massless)	gluon (massless)	W (80 GeV) Z (91 GeV)	graviton
electric charge	0	0	$\pm 1, 0$	0
force	electromagnetic	strong	weak	gravitational

Table 2: Summary of fundamental particles in the SM. Approximate masses of fermion and bosons are given except neutrinos. Its mass is less than 2 MeV from mixing experiments. Each one of them has an antiparticle, which has the opposite charges of it, but the mass is the same between them.

Experiments reveal a three generation structure for fermions, differing only by mass and flavor quantum number but having the same gauge interactions. Leptons and neutrinos have been grouped with up and down type quarks, as they are the lightest members of each type. The same mass-ordering scheme has been applied for the other two generations.

$$\begin{bmatrix} \nu_e & u \\ e & d \end{bmatrix}, \begin{bmatrix} \nu_\mu & c \\ \mu & s \end{bmatrix}, \begin{bmatrix} \nu_\tau & t \\ \tau & b \end{bmatrix}.$$

The helicity of a particle is called right-handed if the direction of its spin is the same as the direction of its motion. Each family is ordered in SU(2), which is the group of 2×2 unitary matrices with determinant 1, doublets and singlets for left-handed and right-handed helicity, respectively. It may not be clear why the particles have to be ordered in this way at first sight. The reason is that the chiral spinors are the fundamental and anti-fundamental representations of fermions.

The quarks appear with an extra quantum number, color, which can be denoted red, green, and

blue. One generation can be decomposed as

$$\begin{bmatrix} \nu_l & q_u \\ l & q_d \end{bmatrix} = \begin{pmatrix} \nu_l \\ l \end{pmatrix}_L + \begin{pmatrix} q_u \\ q_d \end{pmatrix}_L + l_R + q_{uR} + q_{dR},$$

where the color index is dropped as it has nothing to do with the ordering of the fermions.

2.1.2 Local Gauge Theories

In the SM, fundamental particles are described by space and time dependent fields $\psi(x)$, where x denotes both space and time. Noether's theorem states any symmetry leads to a conserved quantity under an associated transformation. A simple example is translational symmetry, $i.e.$, the outcome of an experiment at CERN today will be the same if repeated elsewhere and whenever.

Before getting into details of local gauge theories, a general procedure is outlined here.

- First, start with a free massive Dirac equation:

$$0 = i\gamma^\mu \partial_\mu(x)\psi(x) - m\psi(x), \tag{1}$$

  where γ^μ are gamma matrices, and m is the mass of the particle.

- Second, decide what kind of symmetry to be applied to the equation
- Third, transform the equation
- Fourth, introduce additional fields so that gauge invariance is maintained

The last step is a tricky part in two ways. First, one may argue that the introduction of additional fields may not be needed. In the case of global symmetry, the transformation does not depend on space-time. Then, the invariance of global quantities can be identified as charge of the symmetry. Second, one may argue that it is not necessarily easy to find additional fields which make the equation invariant. There is a systematic way of deriving those fields although it

may get complicated depending on what kind of symmetry is imposed. The heart of above the procedure is the use of symmetry, which have been extensively used and been proved to be useful in statistical and solid state physics, and thermodynamics.

One may start with the global U(1) symmetry ($i.e.$, unitary transformation) as the simplest example in the high energy physics theory. The Lagrangian of a free massive Dirac fermion is

$$L_0 = i\bar{\psi}(x)\gamma^\mu\partial_\mu(x)\psi(x) - m\bar{\psi}(x)\psi(x). \tag{2}$$

Now consider a unitary transformation, where unitary operator is defined as

$$U^{-1} = U^\dagger. \tag{3}$$

In words, the adjoint operator of unitary operator is the inverse of unitary operator. The field transforms like

$$\psi(x) \rightarrow \psi'(x) = exp\{iQ\theta\}\psi(x), \tag{4}$$

where $Q\theta$ is a pure convention-dependent quantity. θ is the phase and Q can in general be identified with the fermion charge number. The phases are canceled out in the L_0 as expected (there are ψ and $\bar{\psi}$). This global symmetry would be considered as an origin of a charge, which does not change wherever and whenever it is placed.

The next simplest example is the local U(1) symmetry, where the phase depends on location in space-time. In other words, it requires symmetry under local phase transformation $\theta(x)$. L_0 changes under such a local gauge transformation because a partial derivative of the phase would be present. To restore local symmetry, one introduces a new spin-1 field A_μ which transforms as

$$A_\mu(x) \rightarrow A'_\mu = A_\mu(x) - \frac{1}{e}\partial_\mu\theta(x) \tag{5}$$

and the covariant derivative is defined as

$$D_\mu\psi(x) = [\partial_\mu + ieQA_\mu(x)]\psi(x). \tag{6}$$

As desired, D_μ transforms as the field itself and the Lagrangian,

$$L = i\bar{\psi}(x)\gamma^\mu D_\mu \psi(x) - m\bar{\psi}(x)\psi(x) \tag{7}$$

holds the required invariance under local U(1) transformation. The introduced field A_μ is invoked by the gauge principle and couples to charged fermions with strength eQ. For completeness a gauge invariant kinetic term of the field is added to the Lagrangian,

$$L_{kin} = -\frac{1}{4}F_{\mu\nu}(x)F^{\mu\nu}(x), \tag{8}$$

where $F_{\mu\nu} = \partial_\mu A_\nu - \partial_\nu$, and A_μ can be identified as the electromagnetic field strength from the classic electromagnetism.

As the photon is massless, one would like to check if a mass term

$$L_{mass} = \frac{1}{2}m^2 A_\mu A^\mu \tag{9}$$

is forbidden by gauge principle. Indeed, the term is not invariant under the transformation, meaning we cannot add this term to the Lagrangian. And thus the U(1) local symmetry is associated to Quantum ElectroDynamics (QED). The surprising part is that the gauge principle works so well. One may expect that the electromagnetic field needs phases which depend on space-time to account the polarization of electromagnetic field, known since the time of Faraday.

2.1.3 Quantum Chromodynamics

After a great success of local gauge theory for QED, now we turn our attention to Quantum ChromoDynamics (QCD) which is the theory of the strong interactions. As mentioned earlier, there are various mesons and baryons which are quite different from the leptons. This difference could be seen as a hint of the underlying symmetry in QCD, which is different from the symmetry in QED. Assuming mesons to be bound qq states and baryons to be bound qqq states,

where q is a quark or anti-quark and some states may be mixed within themselves. Since there are three quarks at most, one may guess that the underlying symmetry is SU(3) which is the group of 3×3 unitary matrices with determinant 1.

However states have been observed are predicted by symmetry but forbidden by Fermi-Dirac statistics. The Δ^{++} is a spin-3/2 state composed of three u-quarks with the spin configuration $|\uparrow\uparrow\uparrow>$. Quantum mechanics does not allow this state if all u-quarks carry the identical quantum numbers. In other words, it can be thought as an evidence of a new quantum number, which must have three different values at least. The color quantum number is introduced as Red, Green, and Blue. Therefore baryons can be written as $|q_\alpha q_\beta q_\gamma >$, and mesons as $|q_\alpha \bar{q_\beta} >$, where α, β, and γ are color indices. This would drastically increases the number of predicted states.

Although one of experimental mysteries is resolved, there is still another one: why is there no colored mesons or baryons? The color is always white (as a superposition of RBG, or color-anticolor pair) or quarks are confined. In other words, all asymptotic states are singlets under rotations in color space ($i.e.$, invariant under such a transformation). Thus the baryon and meson states are written as

$$B = \frac{1}{\sqrt{6}} \epsilon^{\alpha\beta\gamma} |q_\alpha q_\beta q_\gamma >, \tag{10}$$

$$M = \frac{1}{\sqrt{3}} \delta^{\alpha\beta} |q_\alpha \bar{q_\beta} >, \tag{11}$$

where $\delta^{\alpha\beta}$ is Kronecker delta, and $\epsilon^{\alpha\beta\gamma}$ is Levi-Civita symbol.

The number of colors as assumed to be three has been tested in experiments. If heavy particles can decay into leptons and quarks, branching ratios depend on number of lepton and quark states. The branching ratio is the ratio of a partial decay width divided by the total decay width of the particle. At an ee collider the ratio of hadronic and muonic cross sections is

$$R_{ee} = \frac{\sigma(ee \to hadron)}{\sigma(ee \to \mu\mu)}. \tag{12}$$

As the number of colors increases, the number of possible hadronic final states increases as well. Therefore the ratio should be sensitive to N_C. Below the Z mass peak where the photon propagator (which mediates the interaction) dominates for both $ee \rightarrow qq$ and $ee \rightarrow \mu\mu$, the electric charge is mainly responsible for the coupling. The ratio is given by the sum of quark electric charge squared:

$$R_{ee} \sim N_C \sum_{f=1}^{N_f} Q_f^2, \tag{13}$$

where N_f is the number of quark flavors actually allowed to be produced in the phase space ($i.e.$, the mass of a pair of fermions with respect to the available energy). The measured world average on R_{ee} shows that $N_C \sim 3$.

As in QED one can repeat the procedure outlined earlier: deriving the Lagrangian that includes interaction term starting from a free massive Dirac equation and then apply local symmetry transformation, which is $SU(3)_C$, and finally restore the invariance by introducing additional fields. The difference to the QED case is that one has to deal with 3×3 instead of 1×1 matrices which leads to $3 \times 3 - 1$ = 8 fields instead of one. Furthermore 3×3 matrices do not commute. This non-abelian behavior leads to additional terms involving triple and quartic gluon interaction. This is a different trait compared to photon as a mediator of electromagnetic force.

As a colored object, gluons can interact with other gluons. Despite its massless feature, strong force is short range. Quarks behave like free particles at short distance, and acquire energy when forced to separate. The stored energy eventually produces a quark-antiquark pair, which is a color singlet. The asymptotic freedom, quarks moving as free objects at short distance, and the confinement of quarks, no isolated single quark discovered in nature, can be understood in this context.

With q_f^α representing a quark of flavor f and color α and a vector in color space $q_f^T = (q_f^1, q_f^2, q_f^3)$, one can write the invariant Lagrangian of QCD as

$$L_{QCD} = -\frac{1}{4} G_\alpha^{\mu\nu} G_{\mu\nu}^\alpha + \Sigma \bar{q_f} (i\gamma^\mu D_\mu - m_f) q_f \tag{14}$$

with $D^{\mu}_{q_f} = \left[\partial^{\mu} + ig_s \frac{\lambda^{\alpha}}{2} G^{\mu\nu}_{\alpha}(x)\right] \cdot q_f$, and $G^{\mu\nu}_{\alpha}$ are the gluon field strengths. The covariant derivative D_{μ} contains the eight gluon fields $G^{\mu\nu}_{\alpha}$ and the eight generators of the the fundamental representation of the SU(3). These are $\frac{1}{2}\lambda^{\alpha}$ fulfilling the commutation relations

$$\left[\frac{\lambda^a}{2}, \frac{\lambda^b}{2}\right] = if^{abc}\frac{\lambda^c}{2}, \tag{15}$$

where f^{abc} are the SU(3) structure constants. The existence of gluons was confirmed in three jets events at PETRA in 1979.

2.1.4 Quantum Flavor Dynamics

In the QED review above, it was not mentioned how QED applies to muons and taus. QED describes the interactions of heavier electrically charged leptons as well. However, these leptons decay, and this is not explained by QED. The same applies to QCD, which describes all quarks in the same way. However, QCD does not describe how heavier quarks decay into lighter ones.

Historical puzzles include β decay of nuclei, and energy production in the Sun cannot be explained either by QED or QCD alone. Needed here is a theory of flavor changing processes: Quantum Flavor Dynamics (QFD). There are two complications: the electric charge can be changed as well as the flavor, and neutrino happens to be always left-handed. The latter one encourages us to assign a weak isospin of 1/2 to left-handed fermions (doublet) and 0 to right-handed fermions (singlet) to match a theory to experimental results. Two out of three $(2\times 2-1)$ vector bosons can be combined to $W^{\pm}$ bosons.

$$W^{\pm} = \frac{1}{\sqrt{2}}(W_1 \mp iW_2). \tag{16}$$

The remaining boson must satisfy the following conditions: electrically neutral and massive to match it to the neutral weak force mediator, and thus it cannot be photon, and it should couple to left-handed fermions only, and thus it cannot be Z^0 boson, which can decay into a qq or ll pair.

The breakthrough comes as an additional U(1) symmetry is introduced. A new massless boson

couples to particles carrying weak hypercharge Y, where $Y = Q - T_3$. One may start with any weak isospin doublet, and the result can be applied to the rest of doublets. For example, for u and d-quarks

$$\psi_1(x) = \begin{pmatrix} u & d_L \end{pmatrix}, \; \psi_2(x) = u_R, \; \psi_3(x) = d_R. \tag{17}$$

The free Lagrangian is

$$L_0 = \Sigma i \bar{\psi}_j(x) \gamma^\mu \partial_\mu \psi_j(x) \tag{18}$$

and the fields transform under the global symmetry as

$$\psi_1(x) \rightarrow \psi_1'(x) = exp\{iy_1\beta\} U_L \psi_1(x) \tag{19}$$

$$\psi_{2,3}(x) \rightarrow \psi_{2,3}'(x) = exp\{iy_{2,3}\beta\} \psi_{2,3}(x), \tag{20}$$

where $U_L = exp\{i\frac{\sigma_i}{2}\alpha^i\}$ with i = 1,2,3 acting only on the doublet. In analogy to QED the $y_{j=1,2,3}$ are called hypercharges and $\alpha^i(x)$, $\beta(x)$ are the space-time dependent phases of the transformation. The σ_i are the generators of the fundamental representation of $SU(2)_L$. Again they do not commute (as matrices do not commute in general), and thus it leads to self-interactions between the induced fields. The induced fields appear, as in the QED and QCD cases, in the covariant derivative once local gauge symmetry is required

$$D_\mu \psi_1 = [\partial_\mu + ig\widetilde{W_\mu}(x) + ig' y_1 B_\mu(x)] \psi_1(x) \tag{21}$$

$$D_\mu \psi_{2,3} = [\partial_\mu + ig' y_{2,3} B_\mu(x)] \psi_{2,3}(x), \tag{22}$$

where $\widetilde{W_\mu}(x) = \frac{\sigma_i}{2} W_\mu^i(x)$ is a $SU(2)_L$ matrix field.

One obtains four spin-1 fields for four gauge parameters α_i, β. W_μ^1 and W_μ^2 mediate the observed charged current interaction with $W^\pm$, the two neutral fields are W_μ^3 and B_μ. These are not the physical γ and Z states, as can be easily be seen since $g' y_j = eQ_j$ in the case where B_μ represents the photon but additionally $y_i = y_2 = y_3$ as the photon couples to left-handed and right-handed fields equally. These two requirements cannot be fulfilled simultaneously. The neutral current Lagrangian can be re-written in terms of linear combinations of a new boson B

from U(1) and the one from SU(2). Those particles can be matched to photon and possible Z boson.

$$\gamma = B \cdot cos\theta_W + W^3 \cdot sin\theta_W \tag{23}$$

$$Z = -B \cdot sin\theta_W + W^3 \cdot cos\theta_W, \tag{24}$$

where θ_W is Weinberg angle and appears in boson mass and coupling terms as well.

However, at this point the vector bosons are massless. Let us stop here and summarize. The forces considered so far in the previous two sections have one thing in common: massless boson as mediator. When we turn to the electroweak force, however this is no longer as desired. The $SU(2)\times U(1)_Y$ group is sufficient to describe interactions of β decay where electrically charged leptons become electrically neutral leptons, but the mediators need to be massless to conserve gauge invariance (this is why we cannot add the mass term by hands).

As a retrospect, there was at least one reason to believe weak force was mediated by massive vector bosons as the force is observed short range. As discussed in the previous section, the short range does not necessarily imply the mediators massive. However, unstable lepton bound states can be described by QED alone ($e.g.$, the life time of ground state positronium is $\frac{2\hbar}{m_e c^2 \alpha^5}$), and then the self-interaction shall be weak enough, and thus it should be massive. Also it is fair to note that there were other theories based on different symmetry groups like SO(3), before the discovery of W and Z, and thus the choice of SU(2) was not so obvious.

To proceed, we need a different assumption: something breaks the symmetry and as a result the mediators acquire non-zero mass and that the neutral mass eigenstates are a mixture of W^3_μ and B_μ as a result of the symmetry breaking. The neutral current Lagrangian re-written in terms of Z_μ and A_μ reads

$$L_{NC} = -\Sigma\bar{\psi}_j\gamma^\mu A_\mu \left[g\frac{\sigma_3}{2}sin\theta_W + g'y_j cos\theta_W\right] + Z_\mu \left[g\frac{\sigma_3}{2}cos\theta_w - g'y_j sin\theta_W\right]\psi_j. \tag{25}$$

The A_μ piece describes QED if the following conditions are imposed

$$gsin\theta_W = gcos\theta_W = e. \tag{26}$$

Note that the first equation relates the $SU(2)_L$ and $U(1)_Y$ couplings to the electromagnetic coupling, unifying both two forces in one electroweak force. A summary of these quantum numbers for all fermions within one family is given in Table 3.

	Q	T_3	Y
l_L	-1	-1/2	-1/2
l_R	-1	0	-1
ν_L	0	+1/2	-1/2
ν_R	0	0	0
q_{uL}	+2/3	+1/2	+1/6
q_{uR}	+2/3	0	+2/3
q_{dL}	-1/3	-1/2	+1/6
q_{dR}	-1/3	0	-1/3

Table 3: Quantum number assignment for fermions, where u and d denotes up and down type quarks, and L and R denotes handed-ness of fermions.

Including the gauge-invariant kinetic terms for the gauge fields again by constructing corresponding field strengths $B_{\mu\nu}$ and $W^i_{\mu\nu}$ the massless invariant Lagrangian reads

$$L_{QFD,m=0} = \sum i\bar{\psi_j}(x)\gamma^\mu D_\mu \psi_j(x) - \frac{1}{4}B^{\mu\nu}B_{\mu\nu} - \frac{1}{4}W_i^{\mu\nu}W^i_{\mu\nu}. \tag{27}$$

2.1.5 Higgs Mechanism

In the SM, masses are free parameters. However, explicit mass terms would violate gauge invariance. Therefore another approach is needed to give masses to particles in the SM and still keep renormalizability of the theory.

One way to solve this problem is to introduce yet another field which breaks electroweak symmetry spontaneously and successfully giving masses to vector bosons. In other words, the electromagnetic and weak forces are unified at higher energy scale, but the symmetry is broken by the Higgs mechanism, resulting in massive particles in the SM. One simple remedy, among others, is to introduce $SU(2)_L$ doublet of complex scalar fields

$$\Phi(x) = \begin{pmatrix} \Phi^+(x) & \Phi^0(x) \end{pmatrix} \tag{28}$$

with a gauged scalar Lagrangian of the form

$$L_S = (D_\mu \Phi)^\dagger D^\mu \Phi - \mu^2 \Phi^\dagger \Phi - h(\Phi^\dagger \Phi)^2, \; (h > 0, \; \mu^2 < 0) \tag{29}$$

$$D^\mu \Phi = [\partial^\mu + ig\widetilde{W^\mu} + ig' y_\Phi B^\mu]\Phi, \; y_\Phi Q_\Phi - T_3 = \frac{1}{2}, \tag{30}$$

which is invariant under $SU(2)_L \times U(1)_Y$ transformations. It introduces an infinite set of degenerate states with minimum energy

$$| < 0|\Phi^0|0 > | = \sqrt{\frac{-\mu^2}{2h}} = \frac{v}{\sqrt{2}}, \tag{31}$$

where the conditions, $h > 0, \; \mu^2 < 0$, must be true. Otherwise, the minimum energy is imaginary (non-physical). In this minimal extension where only one SU(2) doublet is introduced, the charged component Φ^+ cannot acquire a vacuum expectation value as a charge is a conserved quantity. The introduced doublet contains four degrees of freedom (each complex scalar has two degrees of freedom) and three of those are used to give the massless vector bosons an extra degree of freedom which means that they can have a longitudinal component of spin.

An acquisition of a longitudinal component implies an acquisition of mass since massless particles, which inevitably travel at the speed of light, do not have a rest frame. It can be seen for photons as a consequence of the equation of motion

$$0 = k^\mu \epsilon_\mu \tag{32}$$

where k^μ is a photon 4-vector and ϵ_μ is a polarization vector that the possible polarization is transverse only. There is one degree of freedom left from the complex scalar field. This leftover can be realized as a spin-0 particle called the Higgs boson.

A consequence of the symmetry properties of L_S is the prediction of the relation between the two boson masses M_Z and M_W

$$M_Z cos\theta_W = M_W = \frac{1}{2} vg, \tag{33}$$

which is confirmed by experimental results. The Higgs boson mass remains as a free parameter in the SM, and the discovery of which is a central goal of the LHC. The mass range of Higgs is

$$114GeV/c^2 < m_H < 158GeV/c^2 \tag{34}$$

set by LEP [6] and Tevatron [7] at 95% Confidence Level (CL).

Higgs mechanism thus solves the problems in QFD and also offers a bonus. Via the Yukawa interaction (scalar field), the Higgs gives masses to fermions as well. Quark masses measured in experiments are eigenstates (diagonal terms) of the Yukawa couplings.

2.2 Beyond the SM

The SM is rather successful in describing physics at moderate energy scales (from O(MeV) to O(100 GeV)). The only undetected particle in the SM is the Higgs, and one may wonder: is it the end of high energy physics once it will be discovered at the LHC? The answer seems to be 'no' because of various reasons. One set of 'nos' arises from high energy physics, and the other one, surprisingly, comes from cosmology.

For a moment, let us consider the possibility that the experiments accidentally coincides with the theory. This possibility soon turns out implausible when it comes to WW scattering, although the Higgs boson has never been observed yet. Without Higgs contributions, the perturbative unitarity is violated in the process at higher energy scale. And thus there shall be a Higgs boson. In this context, there is another problem, which the perturbative treatment stops working as Higgs mass becomes larger since Higgs loops start decoupling from tree level diagrams. And thus the Higgs cannot be too heavy O(TeV). By combing two considerations, LEP limit and the perturbative unitarity, the Higgs mass must be somewhere between O(100 GeV) and O(1TeV).

However most probable mass for the Higgs is derived to be around 89^{+35}_{-26} GeV in the electroweak fit (which combines low and high Q^2 experiments and finds the best value for the mass) [8]. That is inconsistent with the LEP bound although it is only 1σ deviation and hence

statistically insignificant. Furthermore, the electroweak precision measurements at LEP revealed a nearly 3σ deviation in the prediction for the forward-backward asymmetry parameter A_{FB} to its measured value [9]. This is again statistically insignificant.

One may start thinking about these results hinting something beyond the SM. There must be a Higgs, but the SM Higgs is the leftover of the complex scalar doublet, which was introduced as a minimal requirement to have the symmetry breaking. There could be, for instance, more than one Higgs boson which may have different properties and masses of the SM Higgs ($e.g.$, BR can be altered). This kind of speculation may fit better with the LEP results, but it must be tested of course.

2.2.1 Cold Dark Matter

Dark matter has a long history in cosmology, first postulated by Fritz Zwicky in 1933 [10]. His observation was based on Newtonian dynamics: orbital velocities of galaxies in clusters turned out to be too fast. If the matter in the clusters is all luminous and so that it could be computed, then the galaxies at cluster peripheral would drift away since they are moving too fast. However, galaxies are held together somehow. One of possible explanation, as given by Zwicky, is that there is 'dark' matter which providing additional gravitational force to keep galaxies together.

This dark matter must be 'cold' thus moving with non-relativistic speed, otherwise structure formation in the early universe cannot be explained. Measurements by Wilkinson Microwave Anisotropy Probe (WMAP) show only about 5% of the total mass-energy density of the universe is ordinary baryonic matter. Another 23% is dark matter, and the rest is dark energy associated with Einstein's cosmological constant [11].

Looking at the SM particle list by assuming it is made of a particle, there is no suitable candidate for the dark matter, but there is one which has some of desirable characteristics. The neutrino is electrically neutral, weakly interacting, and stable. The only problem as a dark matter candidate is its mass (nearly massless), and its abundance. The total contribution from neutrinos is far less than the required. One may postulate that there may be a heavier copy of neutrino which

is a perfect candidate as a dark matter. However this possibility is exclude by LEP results as no missing resonance found [12].

2.2.2 Unification of Couplings

The unification of all forces, so far observed twice in the course of history: first the unification of electricity and magnetism, and second the unification of the electromagnetic and weak force. There is nothing wrong having different forces: however we just write down a term for each force in a Lagrangian.

However, nature has already demonstrated such an unification not once but twice at least. Then not just theorists but all physicists may think of the grand unification theory where all forces are unified, except gravity for time being. The extrapolation of the couplings in the SM is shown in Fig. 1, where the couplings do not meet at one point, which means that there is no grand unification ($i.e.$, it is said the forces are grand unified if all the couplings have the same value).

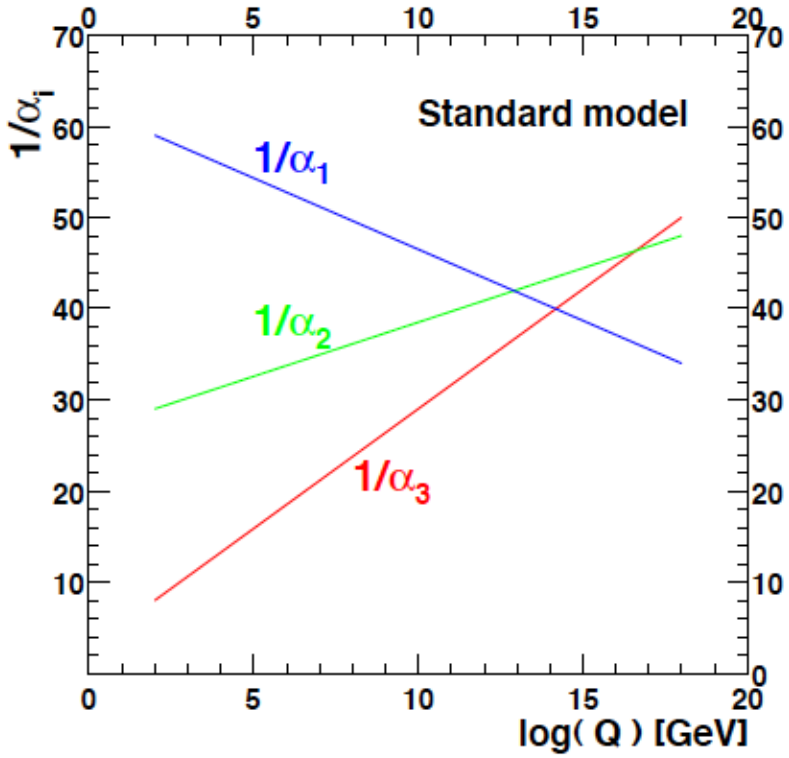

Figure 1: Unification of couplings does not take place in the SM [13]. Three lines correspond to the strong, weak, and electromagnetic forces, respectively.

It is tempting to make them meet at one point. To do so, let us review computation of running

couplings below.

First there must be a charge and then around a charge, a polarization cloud would form. The higher the momentum transfer during an interaction the deeper the cloud will be probed, resulting lessening its effect. Thus the coupling constant α_i depends on the momentum transfer Q^2.

$$\frac{1}{\alpha_i(Q^2)} = \frac{1}{\alpha_i(Q_0^2)} + \frac{b_i}{2\pi} log \frac{Q^2}{Q_0^2} \tag{35}$$

The parameter b_i is determined by the processes generating the polarization here for the SM.

$$b_1 = 0 - \frac{4}{3}N_F - \frac{1}{10}N_H \tag{36}$$

$$b_2 = \frac{22}{3} - \frac{4}{3}N_F - \frac{1}{6}N_H \tag{37}$$

$$b_3 = 11 - \frac{4}{3}N_F + 0 \tag{38}$$

with the number of families and the number of Higgs multiplets in the SM. Therefore the grand unification may be realized if additional interacting particles with right attributes are added, so that running the couplings get additional contributions at the energy scale defined by the mass of new particles.

2.2.3 Hierarchy Problem

In theory, the mass of a Higgs could be unstable if it is not fine tuned. The Higgs mass m_H has two contributions: the fundamental bare mass parameter m_0 and radiative boson corrections, in this example the W boson (the largest fermionic correction is from top loops).

$$m_H^2 = m_0^2 + \delta m_W^2 \tag{39}$$

The bare mass is not that which is measured in experiment. The corrections depend on the cutoff scale Λ and the boson mass.

$$\delta m_W^2 \sim -g_W^2 \int_{\Lambda_0}^{\Lambda} \frac{d^4k}{k^2} \sim -g_W^2(\Lambda^2 + m_W^2). \tag{40}$$

Using the Planck scale, $\Lambda \sim M_{Pl}$, one gets a correction of order of 10^{36}GeV^2. Thus the mass parameter must be of the same order of magnitude to cancel this effect. To get a Higgs mass of the order of 100 GeV this cancellation must be accurate for 32 orders of magnitude. One may consider such fine tuning unnatural, although nature does not forbid it.

Consider the calculation of the electron mass as an example [14]. Let us assume there is no positron, and still we may perform the computation. The number turns out to be about 10 GeV, which is much larger than the mass of electron. This is, strictly speaking, not necessarily considered wrong, because the bare mass of electron is unknown any way, and instead the bare mass has to be fine tuned. However, one may introduce an antiparticle of electron and then the tuning becomes unnecessary, because electron and positron contributions are roughly canceled out due to the underlying chiral symmetry.

If there were fermions with roughly the same characteristics of the bosons, additional fermionic loops would be added.

$$m_H^2 = m_0^2 + \delta m_W^2 + \delta m_{\widetilde{W}}^2. \tag{41}$$

These loops stabilize the value of m_H as they introduce an opposite sign (bosonic loops do not bring a minus sign but fermionic ones do).

$$\delta m_{\widetilde{W}^2} \sim +g_{\widetilde{W}}^2 \int_{\Lambda_0}^{\Lambda} \frac{d^4k}{k^2} \sim +g_{\widetilde{W}}^2(\Lambda^2 + m_{\widetilde{W}}^2). \tag{42}$$

This works only if $g_W^2 = g_{\widetilde{W}}$ and $m_W^2 = m_{\widetilde{W}}^2$. Otherwise fine tuning is still needed although it becomes less severe if $g_W^2 \sim g_{\widetilde{W}}$ and $m_W^2 \sim m_{\widetilde{W}}^2$, and it is called little hierarchy problem. To understand this, we can again check the masses of electron and positron, which are identical.

2.3 Supersymmetry

In the last chapter, motivations to introduce non-SM particles are reviewed. Suppose we want to go along this direction, with what guideline shall we proceed? As repeatedly discussed in the SM section, our main guideline is a symmetry. Most fundamental symmetries are already used in the SM. However, there is one symmetry missing in the SM, which is a symmetry between

fermions and bosons. In the SM, the role assignment for fermions and bosons is fixed: bosons are force carriers, and fermions are matter content. If the symmetry between fermions and bosons is introduced, hierarchy problem goes away as explained in the previous section.

By assuming such a symmetry exists at TeV scale, this is good news for experimentalists as it doubles the number of particles in the SM. Strictly speaking, the doubling is not exact, although sometimes it is said a 'mirror' copy of the SM is created once SUperSYmmetry (SUSY) is introduced. One of complexities comes from electroweak symmetry breaking, which mixes B and W fields so that the weak bosons and photon can be realized as they are measured in experiments. There is, in general, no need to form a supersymmetric copy of photon for example. Instead, Bino and Winos are introduced before electroweak symmetry breaking. Another complexity comes from the structure of Higgs doublet, which will be described in the next section.

With these exceptions in mind, for each SM particle, one new particle with exactly the same attributes is introduced by changing its spin by a half unit. Mathematically, there is an operator Q which transforms fermions to bosons and vice versa. Such operations must be anticommuting spinors carrying spin half, and thus supersymmetry is a space-time symmetry. For a realistic theory involving chiral fermions, the Haag-Lopuszanski-Sohnius extension of the Coleman-Mandula theorem requires the following relations on the operator Q [15] and [16].

$$\left\{Q, Q^\dagger\right\} = P^\mu \tag{43}$$

$$\{Q, Q\} = \left\{Q^\dagger, Q^\dagger\right\} = 0 \tag{44}$$

$$[P^\mu, Q] = \left[P^\mu, Q^\dagger\right] = 0, \tag{45}$$

where P^μ is the generator of space-time translation.

One aspect of this algebra is that supermultiplets in which the particle states are grouped. As Q and $Q^\dagger$ commute with most symmetry transformations all states in one supermultiplet possess equal masses and quantum numbers with the exception of spin. The common mass within each supermultiplet is realized when the symmetry is intact. Once the symmetry is broken, there is

no longer the common mass ($e.g.$, electron mass is different from the supersymmetric partner of electron). Each of these supermultiplets contains equal numbers of bosonic and fermionic degrees of freedom, as a natural result of the symmetry between fermion and boson as desired.

2.3.1 Supermultiplets

Let us construct simple supermultiplets starting with spin-0. The simplest one contains one spin-1/2 fermion and two scalars (spin-1/2 fermion has up and down states). The next simplest one contains one spin-1 boson, which ought to be massless to be renormalizable (3-1 = 2 states), and a massless spin-1/2 fermion. Finally there is a particle for each the SM particle, effectively doubling the number of particles. The last one contains a spin-2 graviton (5-1 = 4 states) and one spin-3/2 fermion (4 states).

The Higgs sector needs special care. If one assumes only one Higgs, gauge anomalies appear in the electroweak gauge sector, spoiling the renormalizability of the theory. Additionally the supersymmetric Higgs mechanism gives mass only to fermions in one spin state. To solve these problems two doublets are needed, resulting in eight degrees of freedom as opposed to four in the SM. Only three out of eight are consumed by vector bosons upon SUSY breaking, leaving five Higgs bosons left. Each fermion in the SM is accompanied by a supersymmetric partner. The gauge boson counterparts are gauginos. As mentioned earlier, gauginos usually do not directly correspond to gauge bosons in the SM, rather these supersymmetric particles mix together with four higgsinos to form neutralinos and charginos. The eight gluons have eight gluinos.

2.3.2 SUSY Breaking

By recalling the fact a supermultiplet has one common mass, unbroken SUSY theories do not fit reality. No sparticle has been observed yet. For example, a boson with the mass of the electron would be easily observed.

Therefore the symmetry must be broken, meaning sparticle masses are not equal to the masses

of their corresponding particles ($e.g.$, selectron mass must be much higher than electron mass). The breaking is usually introduced by additional terms in Lagrangian, which parametrize the effects of SUSY breaking without actually explaining why it is broken. If this breaking is hard, all couplings and masses are to be freely chosen, and the hierarchy problem would most likely reappear. Consequently, the breaking must be soft so that couplings in broken and unbroken SUSY must be approximately equal.

Then the SUSY Lagrangian can be separated in two pieces: one contains the gauge and Yukawa interactions that preserve SUSY invariance, and another one contains the breaking terms.

$$L = L_{SUSY} + L_{Soft} \tag{46}$$

These breaking terms may spoil the solution for the hierarchy problem, if the sparticle masses are too high. To avoid the fine tuning, sparticle masses are kept to O(TeV).

In unbroken SUSY all attributes are determined, thus there are no new free parameters besides the 19 of the SM. Breaking leads to more free parameters: in the MSSM there are 105 new parameters, eight in the gaugino-higgsino sector, 21 masses, 36 mixing angles and 40 CP violating phases in the squark-slepton sector. Some of these parameters are constrained by experiments. However, most of them remain as free parameters, which of course makes SUSY theories comparisons to experimental results difficult.

2.3.3 SUSY Answers to the Problems in the SM

For all the above mentioned problems SUSY provides solutions. One may assign a new multiplicative quantum number, R-parity to each particle: +1 for the SM particle, and -1 for sparticle. If R-parity is conserved, sparticles can only be produced or annihilated in pairs. Thus the Lightest SUSY Particle (LSP) is stable and may be identified as Cold Dark Matter if it is electrically neutral, weakly interacting, and massive.

The coefficients of running the couplings, with new particles, become

$$b_1 = 0 - 2N_F - \frac{3}{10}N_H \quad (47)$$

$$b_2 = 6 - 2N_F - \frac{1}{2}N_H \quad (48)$$

$$b_3 = 9 - 2N_F - 0 \quad (49)$$

with two SUSY Higgs doublets. Thus the evolution of the couplings will change leading to one common point at high energy. Above this energy the coupling stays the same. The unification of the couplings do not take place for arbitrary number of new particles. SUSY does provide the right number of new particles so that the unification occurs at higher energy scale. The unification is shown in Fig. 2.

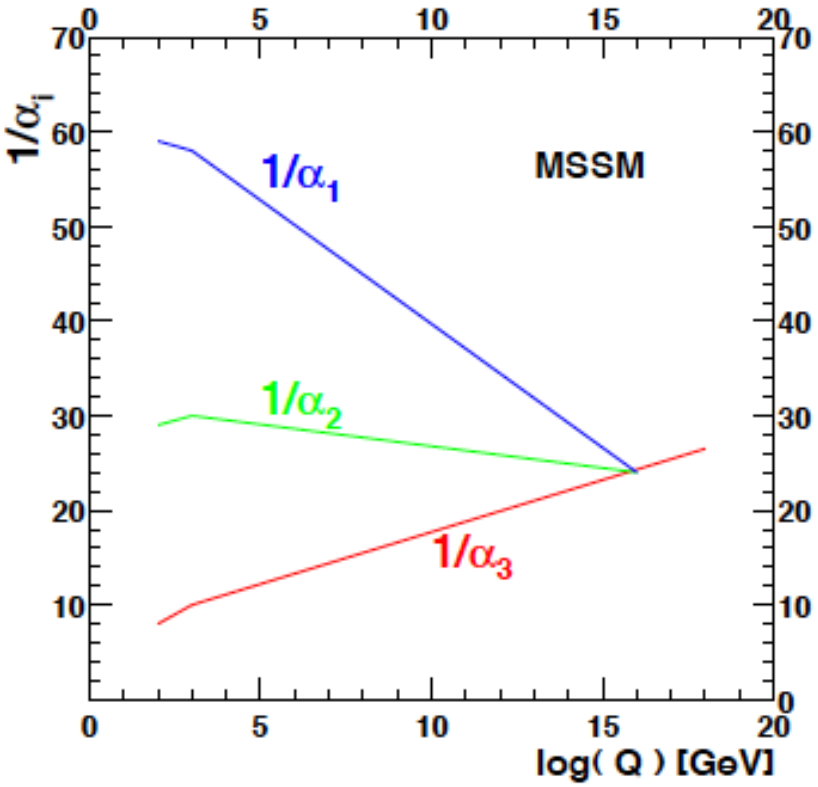

Figure 2: Unification of couplings does take place in the MSSM [13]. Three lines correspond to the strong, weak, and electromagnetic forces, respectively. The line stays the same after the unification.

Finally, bosonic and fermionic SUSY particles now appear in the higgs mass calculation, resulting a cancellation of the divergence so that Higgs mass becomes finite and its mass scale stabilizes. Few Feynman diagrams are shown in Fig. 3 for top, stop, W boson, and supersym-

metric W loops.

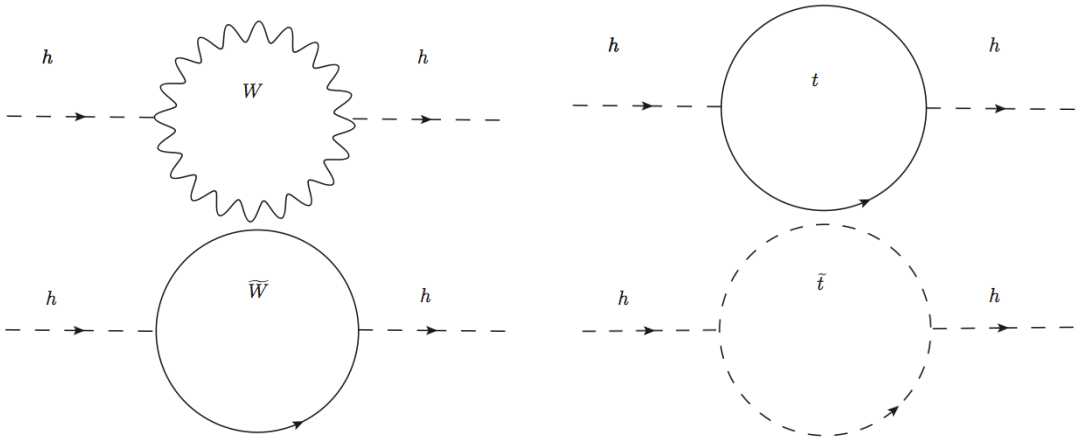

(a) W and $\widetilde{W}$ loop (b) Top quark and stop loop

Figure 3: Few example Feynman diagrams of top, stop, W, and $\widetilde{W}$ loops. These diagrams are not exhaustive a list of radiative contributions to Higgs mass ($e.g.$, tadpole and seagull ones are not shown). The key feature here is the relative minus sign between fermion and boson loops. As long as there are such pairs, the divergence does cancel as a sum [17].

2.3.4 minimal Supergravity

Let us recall the procedure for local gauge theories. Starting from a free Dirac equation, pick a symmetry to be imposed. Transform the Lagrangian under the symmetry, and finally restore the symmetry by introducing additional fields. The same has been done for SUSY by assuming super gravity fields breaks SUSY. In this context, the newly introduced fields are the spin-3/2 gravitino, and spin-2 graviton.

As mentioned in the previous section, SUSY must be softly broken. Now one may recall how the electroweak symmetry was broken. Essentially the same mechanism can be used here as well. In a locally broken SUSY, the gravitino absorbs the goldstino (which is a supersymmetry version of Numbu-Goldstone boson) and thus acquires its mass: much like the Higgs-mechanism in the SM. Although the theory now includes gravity, it is still not a full quantum theory of gravity, as it is still not renormalizable.

To avoid gauge anomalies the breaking must take place in a hidden sector. Its effect must then be transmitted to the visible sector. This can either be done by gauge forces or by gravity,

Gauge Mediated SUSY Breaking (GMSB), and SUperGRAvity (SUGRA), respectively. While MSSM is a low energy effective theory, including gravity allows to consider energy close to the Planck scale. This minimal SUGRA (mSUGRA) reduces drastically the number of free parameters by assuming various unification at high energy scale (from 105 to 5). These are:

- m_0, common scalar mass at the grand unification scale
- $m_{1/2}$, common gaugino mass at the grand unification scale
- A_0, common trilinear coupling
- $tan\beta$, ratio of Higgs field vacuum expectation values
- $sign(\mu)$, sign of the common higgs mass parameter

The mSUGRA model is reviewed in detail in following sections while GMSB is reviewed toward to the end of the theory section.

2.3.5 mSUGRA Mass Spectrum

It is often assumed that superpotential and SUSY breaking parameters are less than few TeV, SUSY CP violating terms are almost zero, and only third generation Yukawa couplings are significant (motivated by heavy the third generation fermions). Even in this simplified model, nice properties of the spontaneous symmetry breaking are preserved. One of phenomenologically interesting parts of the MSSM is its mass spectrum. The mass spectrum splits between chiral partners. Inspired by the unification of gauge couplings in the MSSM, it is common to assume the universality amongst parameters in the MSSM at the Grand Unification Theory scale $\sim$ O(10^{16} GeV).

In the mSUGRA, only five parameters need to be set. However, setting parameters at the Planck scale itself does not help us much since it is impossible to probe such a scale at existing colliders, even the LHC. Useful information is the mass spectrum of sparticles at TeV scale. This could be obtained with Renormalization Group Equations. Assuming SUSY charge conservation, the Lightest SUSY Particle (LSP) is stable and yet heavy enough to be a dark matter

candidate. In the mSUGRA the gravitino is usually too heavy and a sneutrino as the LSP is inconsistent with LEP result. There is one possibility left which is the lightest neutralino. The mass spectrum depends on the parameters, but usually the following observations apply. The mass relation of gauginos roughly equals to 1:2:7 [2]. This is originated from the couplings at the electroweak scale through Renormalization Group Equations. The gluino is almost always heaver than other sparticles. And the LSP gives a rise of $E_{\mathrm{T}}^{\mathrm{miss}}$ of O(m_{LSP}).

2.3.6 Sparticle Production in Proton-Proton Collision

Production of sparticles depends on mass of sparticles and of course the type of beams. The LHC is a pp collider and thus the strong production is expected as a dominant mode. Production modes can be grouped by the forces involved.

- Strong force for squarks and gluino production
- electroweak force for slepton, neutralino, and chargino production

Squarks/gluino and Chargino/neutralino productions occur in leading order as illustrated in the following Feynman diagrams, Fig. 4 and Fig. 5.

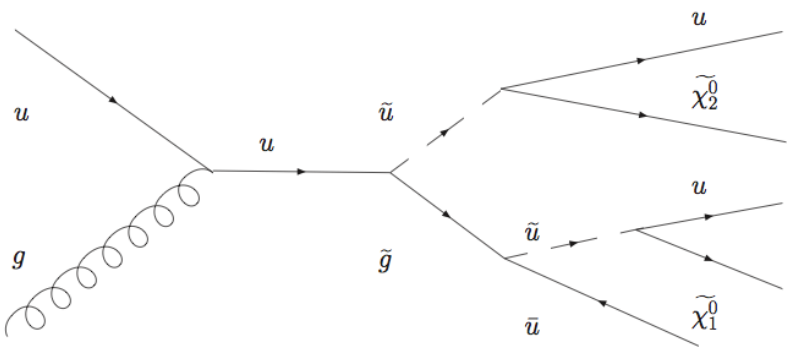

Figure 4: Feynman diagram of gluino-squark production and possible decay chain, which leads to jets and $\widetilde{\chi}$s. If a gluino and squark are heavy, high E_{T} jets are expected in a final state.

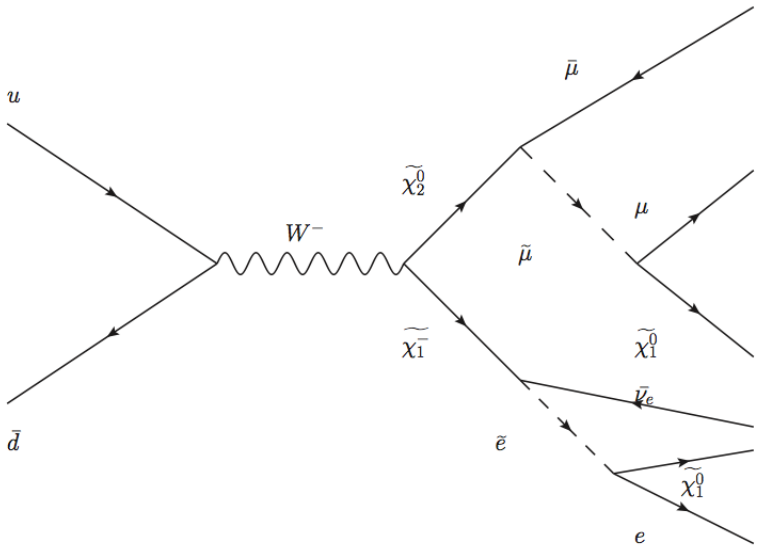

Figure 5: Feynman diagram of chargino-neutralino production and possible decay chain, which leads to three leptons (two μs and one e), one neutrino, and one LSP. It can be thought as a SUSY version of WZ production, where the trilepton charge is ± 1, and one neutrino is expected. A higher $E_{\mathrm{T}}^{\mathrm{miss}}$ is expected as well as there is one LSP contributing to $E_{\mathrm{T}}^{\mathrm{miss}}$.

2.3.7 mSUGRA Decay

The decay modes available for each sparticle again depend on the mass spectrum and thus only dominant ones are described below.

- Gluinos decay as $\widetilde{g} \to q\widetilde{q}$, and $\widetilde{g} \to q\widetilde{q}* \to qq\widetilde{\chi}$ for $m_{\widetilde{g}} < m_{\widetilde{q}}$.
- Squark decay as $\widetilde{q} \to q\widetilde{g}$, or $\widetilde{q} \to q\widetilde{\chi}$ for $m_{\widetilde{q}} > m_{\widetilde{\chi}}$.
- Chargino/Neutralinos decay as $\widetilde{\chi} \to \widetilde{l}l$, or $\widetilde{\chi_n} \to \widetilde{\chi_m} + Z^0/W^{\pm}$ for $m_{\widetilde{\chi_n}} > m_{\widetilde{\chi_m}}$.
- Sleptons decay as $\widetilde{l} \to l + \widetilde{\chi}$ for $m_{\widetilde{l}} > m_{\widetilde{\chi}}$.

2.3.8 mSUGRA Benchmark Points

There are two types of analyses: model dependent and independent search. Most of analyses are model dependent as well as this analysis. Model dependent analysis has some advantages: discover something exotic or set limits on the parameters in the model. On contrary, model

independent studies can be used to measure how much the SM prediction deviates from the data, but the reason why the data deviates is unclear.

However, a difficulty may arise when the model has many degrees of freedom, like the MSSM. In principle we can scan through 124-parameter space and set limits there, although interpretation of the result is not straightforward. In practice, it is not needed because not all of parameters are crucial in the analysis. There is a subset of parameters which are important because they have much larger impact of the final number of events passing certain selection.

There will be many studies will be presented by different groups on SUSY but with different signatures or even at different detectors. Then the question is how to compare those different analyses in a coherent way. The best way to compare different studies is that to have the common set of signal points. If the same signal and selection is used, then the results should be identical whoever does the analysis. The benchmark points are selected by the CMS community, and all collaborators are supposed to use those points. The chosen mass points are divided into two categories based on mass scale, Low Mass (LM) and High Mass (HM) points. As the cross section decreases for increasing sparticle masses, it is unlikely to detect the high mass points within early data. Therefore in this analysis only some of the LM points are compared to the data. Table 4 summaries the parameters of the LM points.

With the exception of LM9 and 10 all these points have a mass hierarchy of $m_{\widetilde{\chi}} \leq m_{\widetilde{l}} \leq m_{\widetilde{g}}$ and thus the typical SUSY events are characterized by the cascade decay of $\widetilde{g} \rightarrow q\widetilde{q} \rightarrow qqq+X$. The use of high E_{T} jets is motivated here, and it depends on analysis strategy if one would like to require a lepton and $E_{\mathrm{T}}^{\mathrm{miss}}$. The advantage of requiring at least one lepton is signified by the fact that a non-prompt lepton can be highly suppressed by requiring a considerable tight lepton IDentification (ID) and isolation. At pp collider, QCD background is in general humongous, and thus a certain handle to suppress it is needed. Otherwise most of the observable events are QCD events. In this analysis, at least two leptons are required to have a good suppression of QCD events. Requiring a lepton from SUSY production implying to have a decay of $\widetilde{\chi_n} \rightarrow \widetilde{ll} \rightarrow \widetilde{\chi_1^0}$ where $n > 1$, which gives rise of large $E_{\mathrm{T}}^{\mathrm{miss}}$. A typical SUSY analysis, where at least one lepton expected, would be summarized as event selection requiring at least one lepton plus

	$m_{1/2}$[GeV/c^2]	m_0[GeV/c^2]	tanβ	A_0
LM0	160	200	10	-400
LM1	250	60	10	0
LM2	350	175	35	0
LM3	240	330	20	0
LM4	285	210	10	0
LM5	360	230	10	0
LM6	400	85	10	0
LM7	230	3000	10	0
LM8	300	500	10	-300
LM9	175	1450	50	0
LM10	500	3000	10	0
LM11	325	250	35	0
LM12	247	2545	48	-866
LM13	218	270	40	- 553

Table 4: Low Mass SUSY benchmark points. m_0 is the common scalar mass. $m_{1/2}$ is the common gaugino mass. $sign(\mu)$, the sign of the common higgs mass parameter, is omitted because all of points listed have positive μ. tanβ is the ratio of Higgs vacuum expectation values. A_0 is the common trilinear coupling. mSUGRA assumes universality among parameters at GUT scale.

large $E_{\mathrm{T}}^{\mathrm{miss}}$ plus large hadronic activity.

The LM10 parameter set leads to heavy squarks and sleptons of about 3 TeV thus a direct production of charginos and/or neutralinos is expected. This results in some leptons but only very few jets from gluinos decaying via virtual squarks. LM1, 2, and 6 are compatible with WMAP cold dark matter limits and LM1 is just beyond the Tevatron Higgs reach. LM0 is almost identical to LM2, but its cross section is the highest of the LM points. The others can be made compatible by giving up some Higgs unification assumptions. During the definition of these points a top mass of 175 GeV/c^2 has been used. Later on, with a measured top mass of 172.5 GeV/c^2 [18], it showed that there is no electroweak symmetry breaking for LM7 and 9 using a spectrum calculator SOFTSUSY [19]. These points are not used in this analysis.

Full the mass spectrum is listed in Table 5 for LM1 as an example.

2.3.9 Gauge Mediated Supersymmetry Breaking

As mentioned in Sec. 2.3.2, breaking of the supersymmetry must be soft. However this does not mean it must be broken by the gravitino field. A different way to break the symmetry softly

particle type	mass GeV$/c^2$
$\widetilde{\chi}_1^0$	97
$\widetilde{\chi}_2^0$	178
$\widetilde{g}$	607
$\widetilde{\chi}_1^{\pm}$	178
$\widetilde{l}_L$	187
$\widetilde{l}_R$	118
$\widetilde{u}_L$	559
$\widetilde{u}_R$	542
$\widetilde{d}_L$	565
$\widetilde{d}_R$	542
$\widetilde{t}_1$	405
$\widetilde{t}_2$	581
$\widetilde{\tau}_2$	190
$\widetilde{\tau}_1$	111
h	110

Table 5: Mass Spectrum in LM1 SUSY Point. A tilde denotes supersymmetric particles. Left (L) and Right (R) denotes the chiral representation to which a particle belongs. The full description can be found in [20].

is via gauge interactions of the messenger particles which make the hidden sector communicate with the observable sector: Gauge Mediated Supersymmetry Breaking (GMSB). The soft supersymmetry breaking masses of SUSY partners of SM particles are thus proportional to the strength of their gauge interactions while the gaugino masses satisfy the grand unification mass relations.

The full mass spectrum and couplings are determined by six parameters within the simplest model of this type. The parameters are

- Λ, the scale of sparticles
- M, the messenger scale
- n_5, the number of complete vector representation of SU(5)
- $tan\beta$, ratio of the Higgs field vacuum expectation values
- $sign(\mu)$, sign of the common higgs mass parameter
- C_{grav}, the partial width constant for sparticle decaying to gravitino

The most important parameter of the six is Λ which sets the scale of sparticles. The experimental signature of the model depends on the mass of the NLSP by assuming the LSP escapes from the detector without any footprint. This statement applies to any variant of the MSSM, for example, the mSUGRA as well.

One important difference from the mSUGRA is that the gravitino can be identified as the LSP. In such a case, the decay mode $\widetilde{l_1} \rightarrow l\widetilde{G}$ can be dominant. This mode is indeed dominant if $m_{\tilde{l_1}}$ - $m_{\tilde{\tau_1}} \leq m_\tau$ and produces electrons and muons copiously as staus are suppressed. Given that high reconstruction efficiencies and low fake rates of electrons and muons with respect to taus, this particular scenario is attractive. In this dissertation, a further simplification is done: the gluino mass fixed and the bino mass varied to scan the parameter space. The strong SUSY breaking scale is set separately from that of weak scale: squarks and gluinos can be much lighter than those sparticles in the mSUGRA. Lighter strongly interacting particles result higher production cross section. The slepton masses are taken to be degenerate within few GeV. In this particular scenario, we have many leptons in a final state. This model is referred as Multi-Lepton co-NLSP (ML) or the Gauge Mediated Split Messenger (GMSM) model in the result table and exclusion limit plot. The details of the model can be found for instance in references [21, 22].

To end this theoretical foundation chapter, the motivation for SUSY can be summarized as following. The Ω^- was introduced into the baryon decuplet based on the SU(3) color symmetry. This last baryon was subsequently discovered in experiment in 1964 [23]. In a similar way, superpartners of SM particles are introduced into the theory based on the new symmetry [2]. It remains to be seen if SUSY is a true symmetry of nature.

3 Experimental Setup

The Large Hadron Collider (LHC) is the highest energy collider to date, and it collides protons head on. The Compact Muon Solenoid (CMS) is one of the two general purpose detectors at LHC. In this chapter, collider physics is reviewed, and then the LHC and CMS are reviewed in detail. The former part is based on references [24, 25], and the latter part is based on references [26, 27], respectively.

3.1 Collider Physics

The basic idea of high energy physics is to make highly accelerated particles collide head-on, and then the particles are converted to a form of energy, so that yet undetected particles with high mass can be created, and finally its existence is captured with the detector. The importance of the maximum center-of-mass energy can be understood by the fact yet undetected particles remain so due to its higher mass than previous available energy, such as at Fermilab Tevatron.

There are two different designs: fixed target and colliding beam experiments. Fixed target experiments have advantages in term of simple experimental setup and operation: only one beam, and detectors can be placed in forward regions to collect almost all decay products. On the contrary, colliding beam experiments need two beams (and beam focussing to collide), and nearly 4π solid angle coverage to collect decay products. Despite of their relative complexity, colliding experiments are preferred because of their higher center-of-mass energy.

Through the course of high energy physics (from Lawrence Lab to the LHC), various experiments have been built over the last decades reaching higher and higher center-of-mass energy and therefore opening new windows to explore properties of the underlying physics. As a matter of fact, some of them did not find anything new, which was a consequence of the center-of-mass energy ($\sqrt{s}$) lower than required for some discovery. Thus it is natural to hope to achieve $\sqrt{s}$ as high as possible to discover new exotic particles.

The maximum energy may depend on technologies available, and then it is not necessarily

easy to assert which design is the best. Nevertheless, $\sqrt{s}$ can be calculated easily with special relativity for a fixed beam energy. For a fixed target experiment, the relation between beam energy and $\sqrt{s}$ is given by the formula

$$\sqrt{s} = \sqrt{2} \cdot \sqrt{E_{beam} \cdot m_{target}} \tag{50}$$

whereas the relation for two colliding beams is given by the formula

$$\sqrt{s} = 2E_{beam}. \tag{51}$$

Therefore colliding design is preferable over fixed target type, to gain higher $\sqrt{s}$. When $E_{beam} > m_{target}$, the advantage is significant.

Any new theory which provides solutions to the SM problems, involving new heavy particles, the higher $\sqrt{s}$, the higher production cross section. Even if $\sqrt{s}$ is not high enough to have mass-shell states, new particles could be inferred by indirect measurements which, in usually, require much more complicated analysis. The indirect effect becomes larger as $\sqrt{s}$ gets closer to the energy scale of the new physics.

The discovery of W and Z at UA1/2 ($\sqrt{s}$ = 450 GeV), and top quark at Tevatron Run I ($\sqrt{s}$ = 1.8 TeV) was a natural consequence of the evolution of $\sqrt{s}$. And the LHC (design $\sqrt{s}$ = 14 TeV) is the next step has been taken by human beings to explore the TeV scale. The beam particles commonly used at colliders are electrons and protons.

The experimental environment is clean and well defined at electron colliders since the electron is a point-like particle, without underlying substructure. This implies that the initial state is known and can be used as experimental constraint which is not possible at a hadron collider where the colliding partons p_1 and p_2 carry momentum fractions x_1 and x_2, and thus the effective center-of-mass energy is

$$\sqrt{s_{eff}} = \sqrt{s x_1 x_2}. \tag{52}$$

This is a serious disadvantage in terms of accuracy of measurements because $\sqrt{s}$ varies collision to collision. However there is a huge gain in the magnitude of $\sqrt{s}$. The common strategy in high energy physics is to explore a higher energy scale at pp colliders first, and if new particles are discovered, then conduct precise measurements at ee colliders. The rationale is simple, there is no need to conduct precise measurements on new particles which cannot be created.

As the proton momentum transverse to the beam axis is very small, the transverse energy balance can be measured. Invisible particles like the LSP can be detected indirectly, as they escape undetected and spoil the energy balance in transverse plane. On the other hand, spectator partons usually fly quasi-parallel to the beam direction after the collision and escape detection, making it impossible to reconstruct the center-of-mass frame of the collision. A fraction of the remnants can as well fly through the detector components making it difficult to tell particles originated from hard scattering or soft interactions.

A linear collider would have to be several tens of km long to reach an unexplored energy scale, and that is difficult in practice. In a ring collider synchrotron radiation limits the maximum reachable energy, since the energy loss via synchrotron radiation per revolution of a given particle with mass m and energy E in an accelerator with radius R is proportional to $E^4/(m^4R)$. The mass appearing in the denominator has very important meaning here. The mass of the proton ($\sim$1 GeV) is much heavier that of the electron ($\sim$0.5 MeV), $i.e.$, much less energy loss. A proposal for a muon collider has even been made given that the mass of muon is much larger that of the electron. However, muons are unstable, and thus dedicated technologies needed to build such a collider. The protons, however, are easy to produce in vast quantities: just by ionizing hydrogen and they are heavy enough to reduce the synchrotron radiation energy loss, allowing higher energy. However, they have a drawback of not being an point-like particle as mentioned earlier.

Increasing $\sqrt{s}$ is the most important aspect of the collider, and the next important aspect of the collider is the rate, and therefore the total number of collisions. For instance, typical neutrino experiments expect a handful of neutrino interactions per year given that neutrinos are weakly interacting. Even if $\sqrt{s}$ is high, the production of new particles may never take place actually

at the collider if the production cross section of the signal process is considerably small at the design $\sqrt{s}$ with low collision rate.

And there is another motivation to have as many collisions as possible per beam fill, because preparation of beams take time O(1 hour) and beam intensities decrease as the time goes by. It is best to maximize the number of collisions per beam fill to take data efficiently. The protons circulating in the LHC are bundled into bunches. The more protons per bunch and the more bunches are filled in the LHC, the more collisions take place. Thus the rate for a given process is higher as well.

The expected event rate depends on the cross section and the luminosity delivered by the accelerator

$$\frac{N_{event}}{t} = L \cdot \sigma, \tag{53}$$

where L is the luminosity expressed in units of inverse barn, and σ is the cross section expressed in units of barn. The number and types of possible interactions for a given combination of two partons i and j determine the partonic cross section $\widehat{\sigma_{ij}}$. The sum of these partonic cross sections, weighted by the probability to find each combination, is the total cross section. This probability can be described by Parton Density Functions (PDFs) $f_i(x_i, Q^2)$, which are equal to the probability to find a given parton i with momentum fraction x_i at an energy scale Q.

$$\sigma_{total} = \sum_{i,j} \int dx_i \int dx_j f_i(x_i, Q^2) f_j(x_j, Q^2) \widehat{\sigma}_{i,j}. \tag{54}$$

This leads to a non-trivial energy dependence. While the total cross section will be fairly similar for the LHC and Tevatron, the cross section of processes involving heavy particles will be much higher at the LHC because of higher $\sqrt{s}$.

As the cross section of such interesting processes is usually rather small compared to the total pp cross section, a high luminosity has to be reached in order to gain a sufficient event rate. Assuming a Gaussian proton density distribution of the beam, with width σ_x and σ_y along the

x and y-axes, the luminosity can be approximated by

$$L = \frac{n_b N_B^2 f \gamma}{4\pi \epsilon_n \beta *} F, \tag{55}$$

where n_b the number of bunches per beam, N_B the number protons per bunch and f the revolution frequency, γ relativistic gamma factor, ϵ_n the normalized transverse beam emittance, and β* the beta function at the Interaction Point (IP) and F the geometric luminosity reduction factor due to the crossing angle at the IP. The frequency f is fixed by the speed of light and the accelerator dimensions. Increasing the luminosity will yield a higher probability to get an interesting process per bunch crossing but will also increase the number of background interactions.

3.2 The Large Hadron Collider

The Large Hadron Collider (LHC) is located at the French-Swiss border west of Lac Leman and in the former the LEP tunnel. The tunnel has a circumstance of $27km$ and lies between 45 and $170m$ below the surface. The energetic beams circulate in vacuum pipes there and are kept on track by a magnetic field provided by dipole magnets. Superconducting Radio Frequency (RF, usually referred as resonator) cavities are used to accelerate beams to the desired energy. The LHC is capable of operating with either proton or heavy ion beams. At design conditions, it runs at a luminosity of $10^{34} cm^{-2} s^{-1}$ for pp beams at $\sqrt{s}$ = 14 TeV, supplying the high luminosity experiments CMS and ATLAS with collisions every $25ns$ corresponding to the nominal bunch spacing. Low luminosity runs at $L = 10^{29} cm^{-2} s^{-1}$, and $10^{32} cm^{-2} s^{-1}$ provide data for the elastic scattering experiment TOTEM and b-physics experiment LHCb respectively.

In 2010, the center-of-mass energy was set to 7 TeV and the highest instantaneous luminosity achieved was about $2 \cdot 10^{32} cm^{-2} s^{-1}$.

In order to reach the design luminosity 2808 proton bunches are filled in the LHC, separated by roughly $8m$, or $25ns$. These luminosities are high enough to provide a sufficient rate of hard interactions in which the physics processes interesting for most of experiments take place. At

the same time the probability for soft interactions is orders of magnitude higher than for hard interactions, thus around 20 significant soft interactions are expected per bunch crossing. As these soft interactions are considered unwanted background by the experiments, the detectors must be able to separate these pile-up events from hard interactions. The number of protons per bunch is limited by the non-linear beam-beam interactions that each proton experiences each bunch crossing. In combination with the constraints from the mechanical aperture the nominal peak beam size is $1.2mm$ the maximum bunch intensity is thus $N_B = 1.15 \times 10^{11}$.

At a pp collider both beams need different magnetic field polarities in the dipoles. Thus the beams run in separated vacuum pipes with separated dipole fields. 1232 dipoles are used to hold beams on track. Only in the $\sim$130m long sections at the interaction regions do both beams share one beam pipe. Sustained fields of this strength can only be generated by superconducting magnets, and thus all dipoles are cooled down to $1.9K$ using superfluid helium. Using well established technologies, the superconducting cables are made of $NbTi$ as previously utilized at the Tevatron, DESY, and RHIC, and were chosen for cost reduction and reliability. Using these state-of-the-art technologies a maximum magnetic field strength of $8.4Tesla$ is obtained, providing the possibility of operating with 7 TeV beams. For the dipoles, the twin core design was chosen: two beam pipes with own coils share a common cold mass and cryostat with the magnetic flux circulating in the opposite sense through the two channels.

A collider designed to guide and accelerate beams of a certain energy is usually not suitable for much lower energies. Consequently the LHC main ring must be supplied with pre-accelerated protons. The injector chain consisting of Linac2, Proton Synchrotron Booster (PSB), Proton Synchrotron (PS), Super Proton Synchrotron (SPS) is depicted in Fig. 6.

The protons are produced by ionizing hydrogen in a plasmatron and then accelerating them in the Linac2 proton linear accelerator to 50 MeV. Each of the four rings of the Proton Synchrotron Booster (PSB) is then filled with one 30μs bunch delivered by Linac2. After accelerating the protons to 1.4 GeV, the bunches are compressed to the size of $190ns$. Six of these bunches grouped into two batches are then sent to the Proton Synchrotron (PS). Still at 1.4 GeV the bunches are split in three, then accelerated to 25 GeV and again split in two, resulting in batches

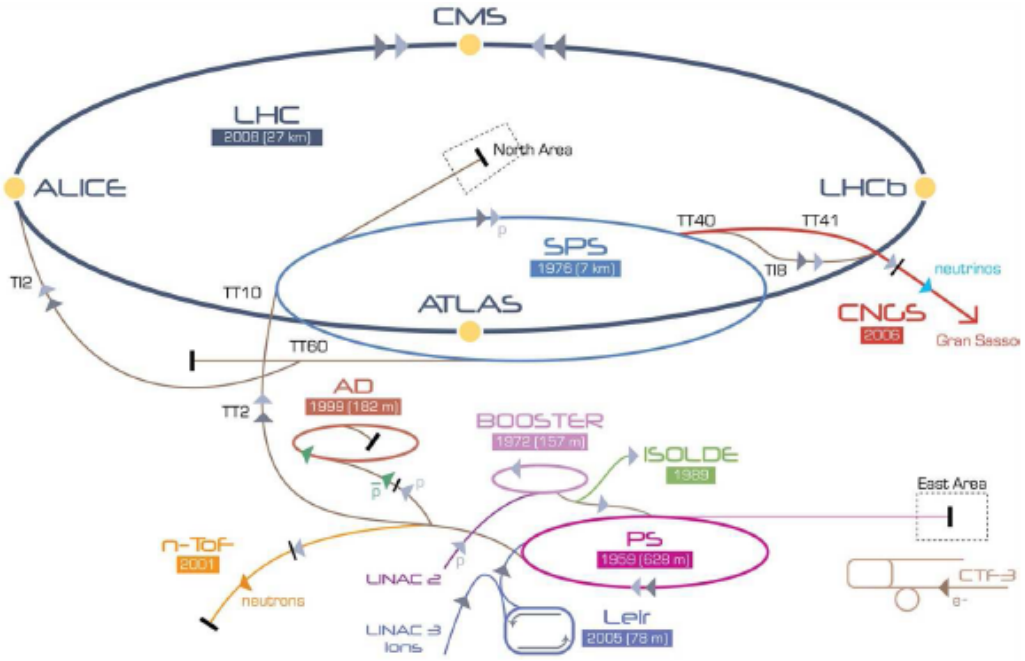

Figure 6: The LHC. The injector chain and the CMS experiment are shown [28] with other experiments.

of 72 bunches. These bunches are now spaced by $25ns$ as desired.

After compression and rotation, the bunches are $4ns$ long and are then fed into the Super Proton Synchrotron (SPS). Four PS cycles are necessary to fill the SPS for one supercycle, then the protons are accelerated to 450 GeV. It takes about 9 minutes to execute 24 SPS supercycles to fill both LHC rings with 2808 bunches in total, plus some additional overhead in form of pilot bunches and setup: about 15 minutes per fill is expected. Rumping up energy takes about 20 minutes, and routine testing between two runs may take 30 minutes. In total, the LHC turnaround is expected to be about an hour. Residual gas scattering and mainly the interactions themselves will reduce luminosity over time with an expected lifetime of 15 hours, resulting in 6 to 12 hours of data taking. Assuming 200 days of data taking per year and above estimate for run length and turnaround time, about $100\,\mathrm{fb}^{-1}$ of data can be collected per year with design conditions.

3.2.1 Startup Conditions

The startup conditions of the LHC in terms of beam energy, number of bunches, and protons per bunch, are well below the design conditions and can be changed in short a period of time.

An incident on September 19, 2008, due to a faulty electrical connection between two of accelerator dipole magnets led to a helium leak and extensive damage in sector 3-4. After the incident every connection was checked and some had to be replaced, which required a partial warmup of the LHC. It was subsequently decided that the LHC would run in 2010 at 3.5 TeV per beam with the energy rising later in the run.

3.3 The Compact Muon Solenoid

In this section, the general features of the Compact Muon Solenoid (CMS) detector are reviewed. The details of the subdetectors is described in the following subsections, in inside-out order.

The CMS detector is a multi-purpose apparatus designed to measure precisely the products from pp collisions produced at the LHC. The detector lies approximately $100m$ underground nearby the French village, Cessy. Its shape is cylindrical and closed with two endcaps. The cylindrical shape allows addition of a solenoidal magnet to measure curvature of charged particles from the interaction point. The coordinate system used in the CMS has its origin at the nominal interaction point. The x-axis points to the LHC's midpoint. The y-axis vertically points upward and hence the z-axis is parallel to the beam direction in the right-handed coordinate system. Transverse energy is derived using x and y components. The cylindrical coordinates have two degrees of freedom: ϕ defined as the azimuthal angle measured in the x-y plane, and the θ polar angle measured from the z-axis. The ϕ angle is a natural choice from the assumed azimuthal symmetry of scattering processes. However θ is not since it is not Lorentz variant. Employed instead is the pseudorapidity defined as η = -$\ln tan(\theta/2)$, which is Lorentz invariant. This is important because a boost along a beam axis due to a different Bjorken x values of the colliding partons cancels out and the difference in η is the same as in the center-of-mass frame.

As described in the last section, the LHC will ultimately operate at design conditions of 7 TeV beam energy and $10^{34}cm^{-2}s^{-1}$ peak luminosity requiring a bunch spacing of $25ns$. Every bunch crossing results in more than 20 pp interactions leading to more than 1000 charged par-

ticles traversing the detector, interacting with subdetector components. This high particle flux of 10^9 particles per second, makes high demands on detector techniques. It must be radiation resistant to ensure long endurance, precise, and reliable.

Different particles may decay differently and/or interact with subdetector components differently. This necessitates different types of subdetectors. The subdetectors record either of the hits made by a charged particles or the number of scintillations. The former quantity relies on the fact that an electrically charged particles ionize gases, or induces charges. The latter relies on the cascade of shower development by an electromagnetic and/or strongly interacting particles.

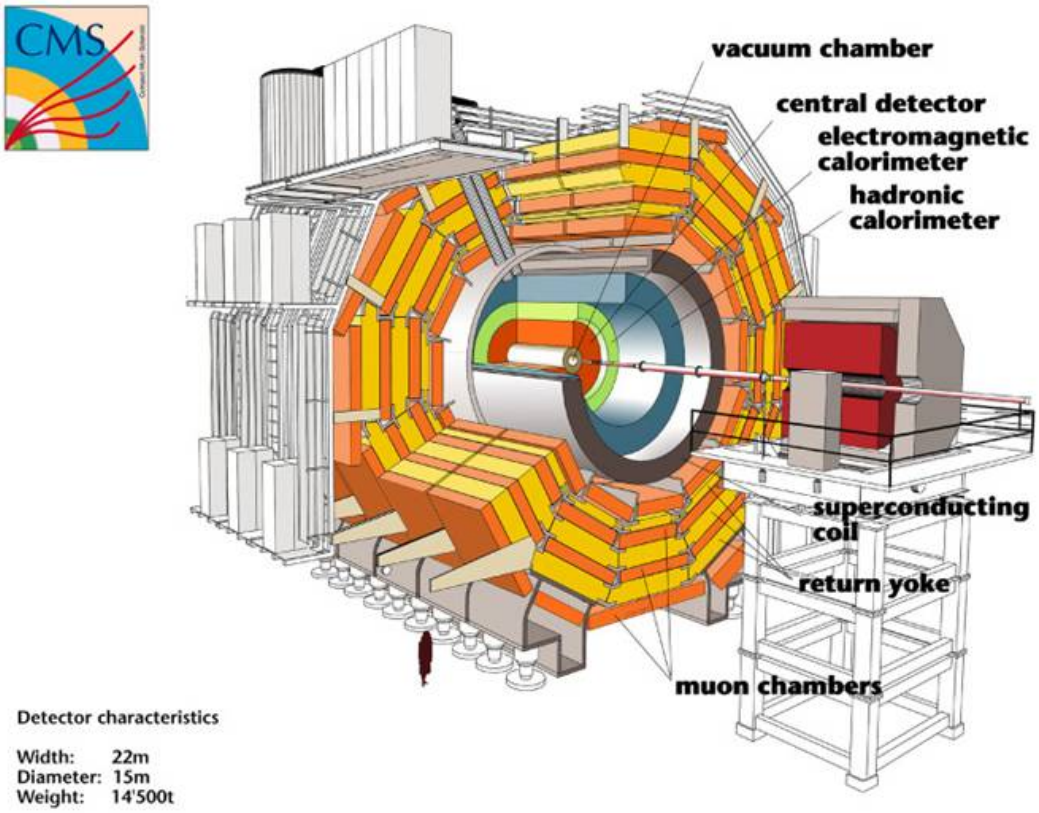

Figure 7: The CMS detector sliced [26]. A typical height of human being gives a rough idea of the size of the detector.

As shown in Fig. 7, the CMS basically consists four elements, listed from inside out:

- The silicon tracker with pixel and strip detectors
- The Electromagnetic CALorimeter (ECAL) made of lead tungstate ($PbWO_4$) crystals
- The Hadronic CALorimeter (HCAL) a brass/scintillator sampling calorimeter

- The $3.8T$ superconducting solenoid providing large bending power in order to measure momentum transverse to the beam
- The Muon System (MS) that uses three different techniques of gas detectors:
  - Cathode Strip Chambers (CSCs)
  - Drift Tubes (DTs)
  - Resistive Plate Chambers (RPCs)

The layout of subdetectors was well thought out to keep dead region and dead materials as small as possible. In total, the CMS detector weights $14500tons$, and has a diameter of $15m$, and is $22m$ long. To ease installation and maintenance the detector is sliced into five wheels and three endcap disks on each end. The central wheel supports the magnets and most components mounted inside the magnet. Two wheels on each side can be moved on air-pads to allow access to the central structures. The detector is closed on each sides by three disks, the innermost supporting the endcaps of the calorimeter. The direction and track curvature of charged particles inside the magnet is measured by the silicon strip tracker and the silicon pixel vertex detector which also provides precise measurements of the interaction vertex. The calorimeter measures the energy and the flight direction of all electromagnetically or strongly interacting particles. The magnet is placed outside of the calorimeter to avoid a degradation of energy measurements in the calorimeter. It allows the measurements of particle momentum transverse to the beam axis via the track curvature and protects the calorimeter against the vast amount of low momentum particles.

The magnet is a distinguishing factor of the CMS and its geometry found its way into the name itself. In contrast to the ATLAS where a toroidal field geometry is used in the muon system and a solenoid one in the tracker, the CMS makes use of a global solenoidal magnet. Being $12.8m$ long and with a diameter of $5.9m$ the four layers of superconducting $NbTi$ coils provide a homogeneous $3.8T$ strong magnetic field inside of the coils, making precise measurements of charged particle's trajectory possible. The world's largest superconducting solenoid stores $2.6GJ$ in the field during operation. The superconductors is cooled down to $4.5K$ in order to

provide fields of such strength. The z-position of a vertex is not affected as the field is parallel to the beam axis providing the possibility of a vertex fit. On the other hand, the coils set a spatial limitation on detector components located within.

The remaining fraction of energy carried by charged particles that are not stopped in the calorimeter is unknown. That is mostly a problem at small η, where material budget is the smallest, and moreover a strong magnetic field is needed outside the coils to provide sufficient bending of muon trajectory. Therefore the yoke is put in place with the interleaved muon stations. Three return yokes are in the barrel region and three in each endcap guide the flux on the outside of the coils with the muon system interleaved within yokes. 10000 out of the CMS total $14500 tons$ are due to these yokes. A drawback of solenoidal design is the inhomogeneous magnetic field in the endcaps which could lead to a possible deterioration of measurements in the muon endcaps. This is one of reasons to choose CSCs for the endcaps.

All detectable particles passing beyond the calorimeters and magnet which should be mostly muons, because photons, electrons, and pions deposit most of their energy in the detector before reaching the muon system. The muon system again works as a tracker measuring direction and curvature of the tracks using the field in the iron return yokes interleaved with the muon chambers as mentioned here.

The vast amount of data produced by the frequent reactions cannot and does not have to be saved completely. Only interesting events will be stored persistently. This is achieved with multiple trigger levels that reduce the event rate from $40 MHz$ to $100 Hz$. The trigger system is reviewed after all subdetectors are reviewed in the following subsections.

3.3.1 Silicon Tracker

Closets to the beampipe, the silicon tracker is mounted to measure the trajectories of charged particles as precisely and as efficiently as possible. This system has a length of $5.8 m$ and a diameter of $2.5 m$ and consists of two different subdetectors: the silicon pixel and subsequently silicon strip detectors.

At design luminosity 20 overlapping inelastic interactions will produce $\sim$ 1000 particles every $25ns$, making the need of a radiation hard technology inevitable. The innermost tracking detector needs a high spatial resolution and fast response to identify vertex positions. Precise measurement of the vertex position is important for two reasons: first to reject most of particles coming from additional interactions, and to identify secondary vertex if there is any. The b, c quarks and τ leptons may travel some mm before decaying, and thus separated from the primary vertex. To detect these secondary vertexes a detector close to the interaction point with excellent spatial resolution is necessary, and this is achieved with the silicon detector.

For good momentum resolution by measuring the track curvature in the magnetic field both good spatial resolution and a long lever arm is necessary. By making use of layers of pixels and strips, both high precision and affordable cost are achieved. The doped silicon semiconductor technique works as following. A charged particle traversing a sensor produces electron-hole pairs that is pulled to the upper/lower electrodes with moderate bias voltage. The analog pulse height is read out and combined with those from adjacent pixels/strips since charge-sharing among them improves spatial resolution.

With the B-field parallel to the z-axis inside the tracker the transverse momenta of charged particles can be determined by measuring their bending in the r-ϕ plane. A compromise had to be found between the high power density of on-detector electronics making high precision measurements possible, but in turn requiring cooling and a minimum of material budget in order to limit multiple scattering, bremsstrahlung photon conversion, and nuclear interactions.

The tracker layout is shown in Fig. 8.

3.3.2 Silicon Pixel Detector

The silicon pixel detector in the CMS which offers excellent spatial resolution is used for vertex detection. At the heart of the tracker a three layered cylindrical silicon pixel detector lies with the layers located at 4.4, 7.3, and $10.2cm$ distance from the IP. It is enclosed by two endcap disks at $z \pm$ 34.5 and $46.5cm$. It consists of 1440 modules and their arrangement is shown in Fig. 9.

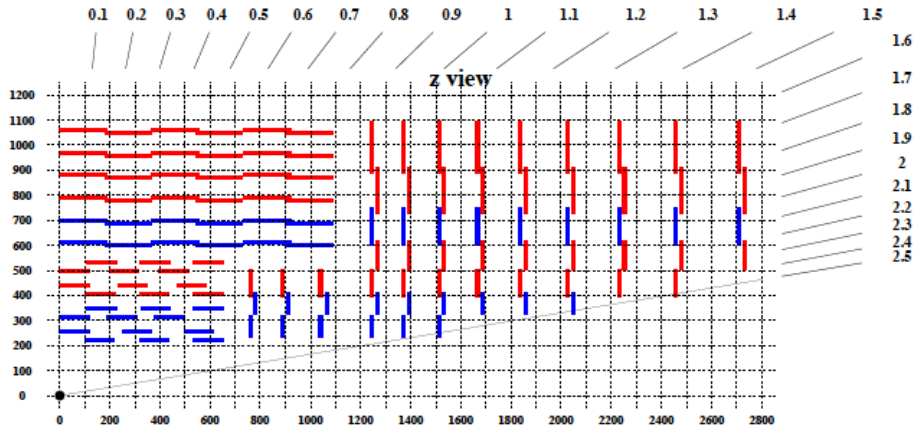

Figure 8: The tracker layout in r-z plane [29]. The layout shows how to avoid dead regions.

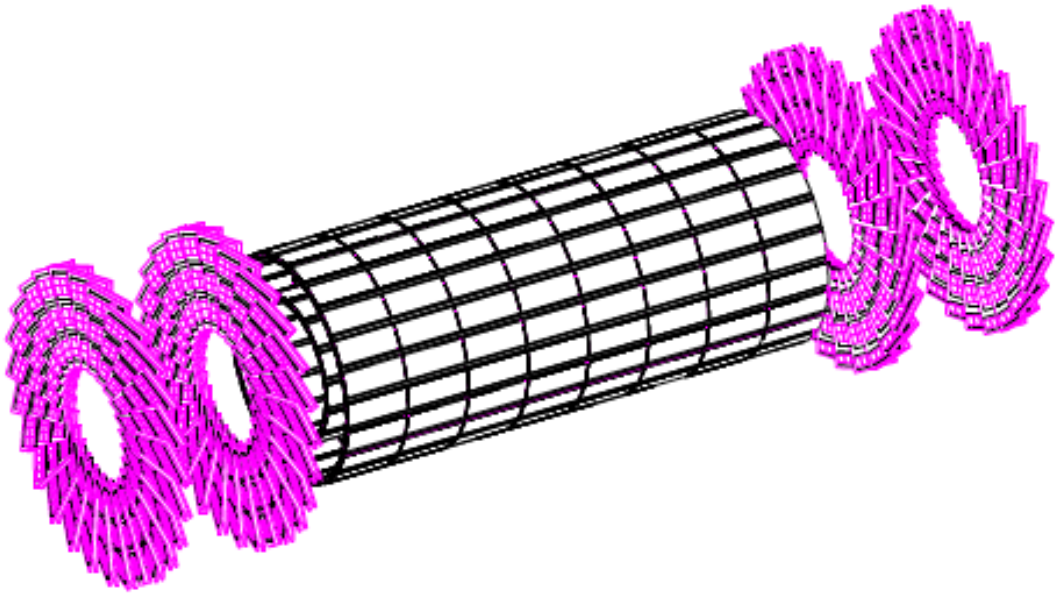

Figure 9: The pixel detector [30]. Each endcap pixel blade (pink) is placed, overlapping with other blades.

The pixel detector provides the seeds for the track finding algorithms. Using pixels of 100×150 μm^2 a resolution of $10\mu m$ in ϕ direction and $17\mu m$ along the beam can be achieved. The charges generated by a passing particle in one pixel will also drift into neighboring pixels because of the high magnetic field. This allows interpolation of the hit position by weighting the pixel signals. Thus a resolution better than the pixel size itself is possible.

The barrel layers cover an acceptance range up to pseudorapidity $|\eta|$ $\sim$1.5. The forward pixel detector provides at least two hits per track up to $|\eta|$ = 2.5. To minimize the amount of material in the particle path, to keep radiation-sensitive electronics away from the interaction point and to maintain the pulse height information, the analogue signal is transmitted by lasers through

optical fibers to the readout electronics. Cooling to -10 C° is needed to abate radiation damage as a lower temperature leads to less mobility of the defects in the semiconductor. This avoids the clustering of defects that would worsen the performance.

3.3.3 Silicon Strip Detector

Ideally, more layers of pixel could be added to have enough hits in the tracker. However, adding more pixel layers costs more than affordable. As the stream of particles spread out as it moving away from the IP, particle occupancy per unit area decreases. Then it is possible to change from pixels to strips which has lower spatial resolution but also lower costs. Using common lithographic processing sensors with strips up to $12cm$ long and a strip pitch of 80 to $120\mu m$ can be made.

Between r = 20 and $116cm$ from the beam, ten such layers, four in the Tracker Inner Barrel (TIB), six in the Tracker Outer Barrel (TOB) accompanied by three disks in the Tracker Inner Disk (TID), and nine disks in the Tracker End Cap (TEC) have been prepared covering $|\eta|$ up to 2.5. Four layers contain double-sided stereo modules. Two modules back-to-back with a slight angle allows a position measurement along the strip. The strip pitch sizes are between 80 to $120\mu m$. 15158 modules with 24244 sensors cover about 9.3 million strips, an active area of $198m^2$ (roughly the size of a tennis court), that is the largest silicon detector ever built.

Charge sharing between adjacent strips allows a resolution of about $15\mu m$ from the inner modules with a strip width of $61\mu m$. Combining 66 million pixels and 9.3 million strips allows a transverse momentum resolution of

$$\frac{\delta p_T}{p_T} = 0.15 p_{\mathrm{T}}[\mathrm{TeV}] \oplus 0.005. \tag{56}$$

3.3.4 Calorimeters

The tracker inside the magnetic field measures the momentum of electrically charged particles. Neutral particles like the photon do not produce hits at all in the tracker if no interaction

occurs between those particles and the tracker. Subsequently, the calorimeter are designed to determine the energy of particles for both charged and neutral particles.

The energy is measured by collecting the light emitted during the deceleration process. As the measured amount of light does not correspond to the particle's energy in case of leakage, to guarantee good energy resolution the particle must be completely absorbed. Thus the calorimeter needs a certain thickness. Electromagnetic particles like electrons and photons can be stopped relatively easily but heavier hadrons like protons and neutrons travel much further through any material.

For Minimum Ionizing Particles (MIPs) like muons or hardly interacting particles like neutrinos this procedure is not possible at all since their interaction length is too long. Muons with p_{T} larger than about 10 GeV are not stopped in the detector at all as they interact much less on their way through the detector. For both light electromagnetic particles and hadrons, materials made of heavy elements are used as they have shorter interaction/radiation lengths. They provide a huge number of free electrons per volume to interact with electrons and photons. Hadrons are absorbed by nuclear interactions with the large nuclei. Thus the CMS calorimeter consists of two layers: a layer of active material to stop light electromagnetic particles, the Electromagnetic CALorimeter (ECAL), and a thick layer to stop hadrons, the Hadronic CALorimeter (HCAL).

Materials providing good energy resolution subdivided into small cells for a good angular resolution tend to be costly. Furthermore the nuclear interaction length for hadron is much longer than the radiation length for electrons and photons making thick layer of material necessary. A compromise between costs and granularity has to be made. A schematic longitudinal slice of calorimeters is shown in Fig. 10.

ECAL

In the CMS, the ECAL built from scintillating lead tungstate crystals ($PbWO_4$), fulfilling various competing requirements at the LHC: fast, finely grained, radiation hard, and yet providing excellent energy resolution. The crystal has two important properties: a short radiation length of $0.89cm$, making the ECAL thin with good energy resolution, a small Moliere radius of

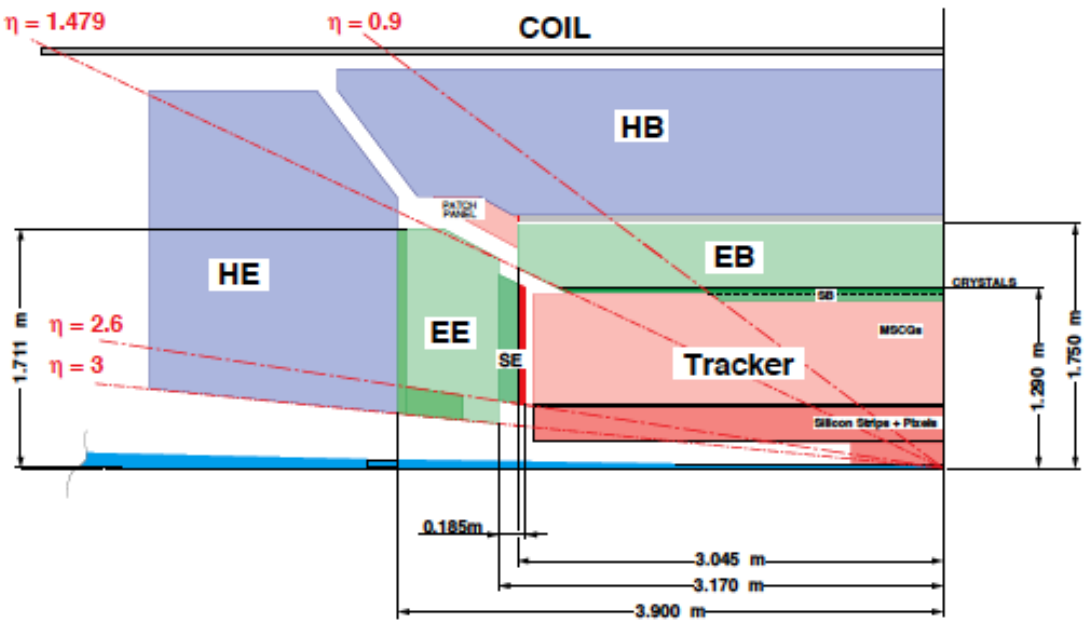

Figure 10: The calorimeter in r-z view [31]. EB and EE are ECAL Barrel and Endcap respectively. HB and HE are ECAL Barrel and Endcap respectively. The material budget is η dependent as shown here.

$2.2cm$.

The radiation length is defined as the energy of electron drops to $1/e$ on average, after traveling one radiation length. On average 95% of the absorbed energy is contained within one Moliere radius providing a good angular resolution. The scintillation time is quite comparable to the LHC bunch spacing in time, 80% of the light is emitted within $25ns$. Hence the deposited energy can be assigned to a certain bunch crossing. Approximately 4.5 photo-electrons per MeV are collected in both Avalanche Photo Diodes (APDs) and Vacuum PhotoTriode (VPTs). The crystal light yield and diode gain are strongly temperature dependent requiring a temperature constant within 0.05K. Both radiation damage and recovery increase with the temperature thus $18C^{\circ}$ is chosen for an optimal lifetime. Consequently, an effective thermal screen between the tracker and ECAL is necessary.

The ECAL is divided into a barrel and endcaps. The barrel consists of 61200 crystals read out by APDs, covering a pseudorapidity range up to $|\eta|$ ~1.5. Holding a crystal volume of $\sim 8m^3$ it weighs $67.4tons$. The crystal length of $23cm$ equals about 25 radiation lengths. APDs, in contrast to common photo multipliers are not affected by the magnetic field.

One endcap contains 7324 crystals with VPT used as photodetectors, covering pseudorapidity

range up to $|\eta|$=3. The ECAL endcaps (EE) are located $3.15m$ away from the interaction point, and each endcap contains $1.45m^3$ of active volume with a mass of $12tons$. Test beam measurements of fully equipped the ECAL modules showed an energy resolution

$$\frac{\sigma}{E} = \frac{0.028}{\sqrt{E}} \oplus \frac{0.12}{E} \oplus (0.003), \tag{57}$$

where E in GeV and the contributions are from the following sources.

- First, stochastic fluctuation of the light yield, light collected and absorption in the ECAL crystals and all material inside of the ECAL
- Second, intrinsic noise from electronics used in readout systems and pileup effects ($i.e.$, additional activity in the detector)
- Third, non-uniformity of crystals leading to non-uniformity of light collection, and calibration errors

A preshower detector at the inner surface of the ECAL endcaps improves the spatial resolution. The preshower consists of two lead radiators, about 2 and 1 radiation lengths thick respectively, each followed by a layer of silicon microstrip detectors. The two layers of detectors have their strips orthogonal to each other: the first layer has vertical strips to measure the vertical position of shower particles, and the second layer has horizontal strips to measure the horizontal position of particles.

The ECAL is arranged mechanically as can be seen from Fig. 11.

HCAL

The HCAL is designed to quantify the hadronic activity of the events and is important for jet energy and $E_{\mathrm{T}}^{\mathrm{miss}}$ measurements as it limits the resolution of these quantities. The barrel and endcaps are sampling calorimeters made from absorber-scintillator sandwiches, in contrast to the ECAL. It consists of four main parts: The Hadron Barrel (HB), Hadron Endcap (HE),

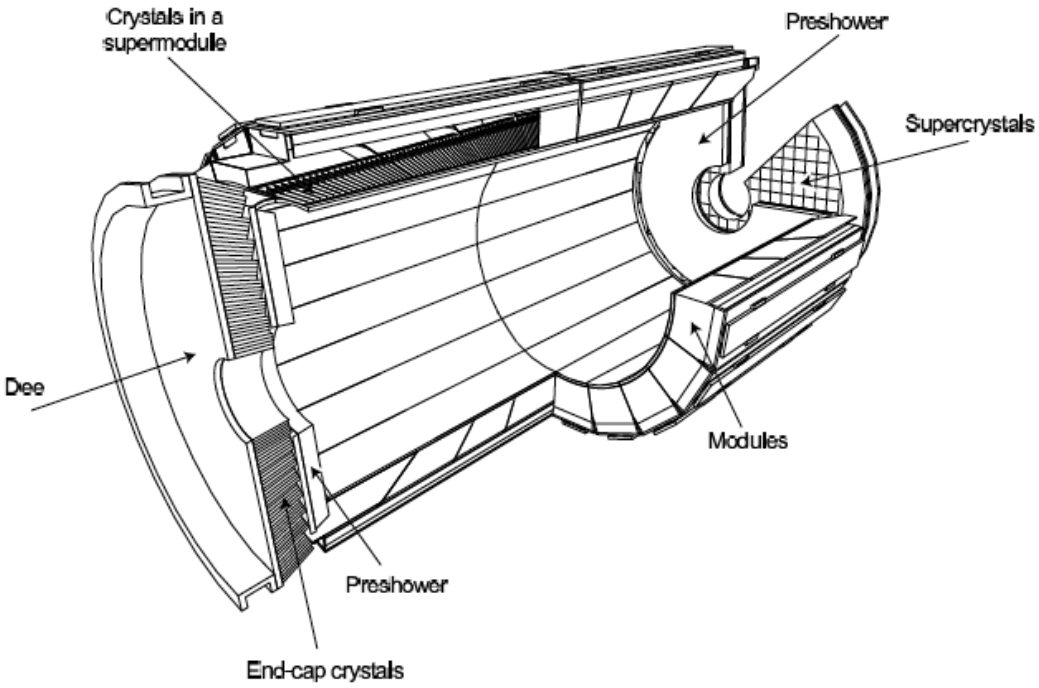

Figure 11: The ECAL layout [32]. The tracker is not shown here.

Hadron Outer (HO), and Hadron Forward (HF) calorimeter, covering a pseudorapidity range of $|\eta|$ <1.3, 1.3 < $|\eta|$ < 3.0, $|\eta|$ < 1.3, and 3.0 < $|\eta|$ < 5.2 respectively.

The long hadronic interaction length and spatial constraints due to the solenoid necessitate the usage of a sandwich design using absorber material to force showering of the hadrons and active material to detect the showers. As the HB and HE are placed inside the solenoid the absorber materials must be non-magnetic. Brass from old Russian artillery shells has been used. Being stored in underground bunkers for decades the inner radioactivity of the brass has declined. This radioactivity would otherwise increase the inner background of the calorimeter.

The barrel section contains: one steel support layer, 14 brass plates, and again a steel support layer. This adds up to five to ten nuclear interaction lengths, depending on η of hadrons. Between each two absorber layers one 3.7mm thick plastic scintillator sheet is placed, which is read out by wavelength-shifting fibers.

The multiple layers suggest a segmented read out along the longitudinal coordinate. However this has not been implemented and is a possible subject for upgrades. The last scintillator after the outermost absorber is 9mm thick to detect showers which develop late in the absorbers. The first scintillator before the innermost absorber uses the ECAL and its support structures as

an absorber. The scintillator layers are subdivided into 72 sections along the ϕ direction and 16 sectors along the η direction, providing a segmentation of 0.087 in η and ϕ. A typical jet is constructed within a cone of 0.5 on η-ϕ plane.

Each endcap contains 17 absorber-scintillator layers, each with $7.9mm$ brass and $3.7mm$ plastic scintillator. Again, a $9mm$ inner scintillator uses the ECAL as an absorber. Both the ECAL and HCAL add up to about ten nuclear interaction length. The granularity decreases from 0.087 to 0.17 in ϕ and from $1.3 < |\eta| < 3$ in η with respect to the barrel. At η = 0, only about five interaction lengths are provided by the HB. Thus the HO is placed after the solenoid and the first return yoke iron as an absorber. Its arrangement is shown in blue in Fig. 12.

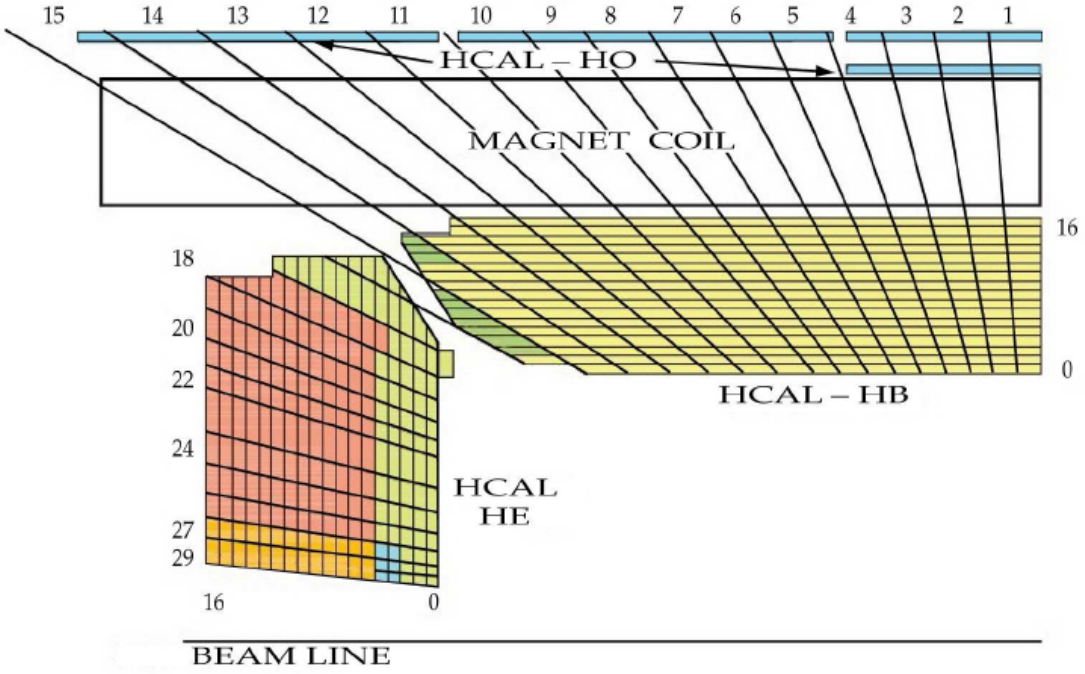

Figure 12: The HCAL in r-z view [33]. HB and HE is HCAL Barrel and Endcap respectively. HO is HCAL Outer and placed after the coils to measure E_{T} of energetic jets.

This extends the total thickness of the calorimeter to at least 11.8 nuclear interaction lengths. The HO scintillators are subdivided into tiles which roughly match the granularity of the HB. The HCAL including HO is expected to reach a resolution of

$$\frac{\Delta E}{E} = \frac{1.2}{\sqrt{E}} \oplus 0.069, \tag{58}$$

where E in GeV. The forward calorimeters, covering $3 < |\eta| < 5.2$, is exposed to large particle

fluxes. Consequently, radiation hardness was the main design goal – even more important than energy resolution. The HF consists of quartz fibers embedded in a steel absorber providing about ten nuclear interaction lengths. As the fibers measure the Cherenkov radiation of passing particles they are sensitive mostly to electromagnetic fraction of the showers.

3.3.5 Solenoid

The CMS has the world's largest superconducting solenoid. Larger magnets have advantages for three reasons.

- First, the longer the magnet, the more homogeneous field away from the edges
- Second, the larger the magnet, the larger tracker and calorimeters ca be fitted inside the detector
- Third, the stronger magnetic field with larger radius, the better momentum measurement in the inner tracker

As magnet price grows nonlinearly with size and strength, a compromise has to be made. The CMS solenoid is $12.5m$ long and has an inner diameter of $5.9m$. It generates homogeneous magnetic field of $3.8Tesla$ using four layers of superconducting coils. Total magnetic induction is shown in Fig. 13.

The field outside of the solenoid is guided by iron return yokes which allows the muon system not to identify only muons but provide a momentum measurements. The longitudinal field causes no deviation of a particle trajectory along the beam axis improving the vertex measurement along the beam axis. The drawback of a solenoid field is its strong inhomogeneity in the endcap region affecting the performance of the muon subsystem.

Assuming the full coil thickness of around $30cm$ to be solid copper a magnet of this size and strength would need about $100MW$ of energy to be delivered electrically and removed as heat. Thus superconducting materials must be chosen. The $NbTi$ coil is cooled below $9.8K$ to stay superconducting. In case of catastrophic failures the $2.6GJ$ stored energy can be dismissed

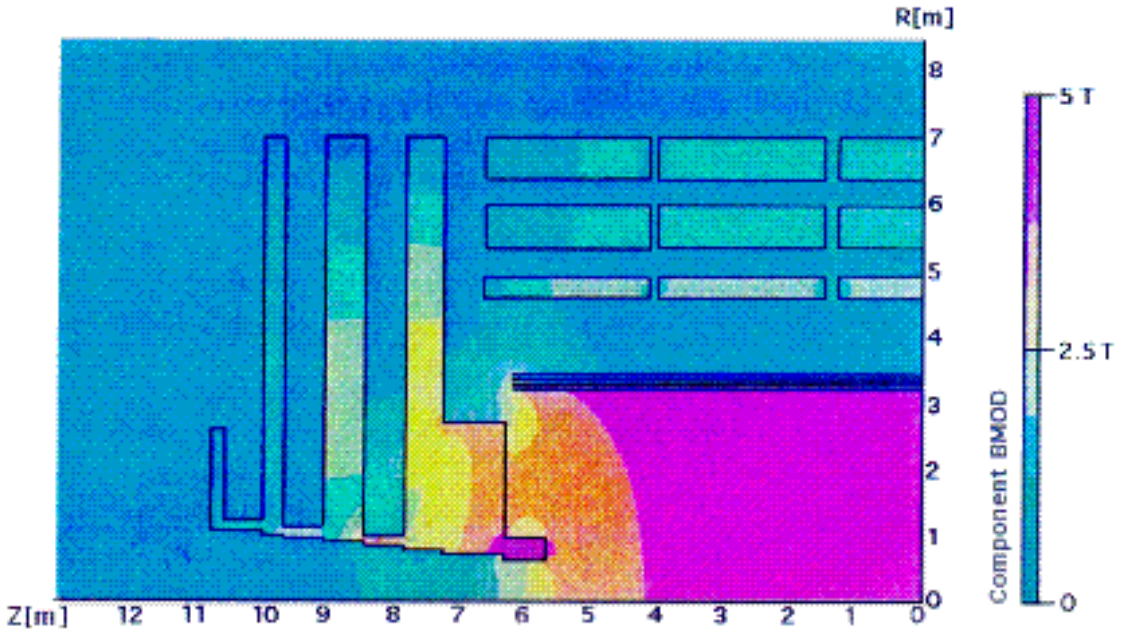

Figure 13: Total magnetic induction in and around the CMS [34]. The field is homogeneous inside the solenoid, but becomes inhomogeneous at the edge of the solenoid, which is important in the muon system.

in about $200s$ using a resistor block located outside the cavern. During normal shutdown the energy will be dissipated slowly in about few hours.

3.3.6 Muon System

The CMS name includes the words, Muon and Solenoid, and the Muon System (MS) is reviewed below. Special attention is given to detecting muons, as the muon is produced in important channels like $Z \rightarrow \mu\mu$, for various experimental checks with the data, and the muon could be a sign of yet undetected processes, like $H \rightarrow ZZ \rightarrow 4\mu$. The advantage of using muons is their cleanness compared to other detectable particles. The calorimeters are designed to contain most energy of photons, electrons, and hadrons. However, muons do not interact with the subdetectors much, and typically only ionize atoms as they traverse material. Most muons reach the MS before losing most of their energy. The MS identifies muons and also measures momenta of muons.

Located outside magnet, and interleaving the return yoke, in conjunction with the inner tracker, the MS must cover the largest area. The area to be covered is increased even more by the

CMS muon system providing not only a muon identification but several hits for momentum measurement.

As multiple scattering in the return yokes dominates the resolution in the MS for a muon p_{T} smaller than 200 GeV, the tracker information is more precise for its determination. However the readout of the tracker is too slow to be used for triggering purposes. Moreover, the particle flux close to the IP is high resulting in many hits with indistinguishable origin, which form false tracks. The MS provides accurate trigger information for true muons and makes it possible to extrapolate muon trajectories back to the tracker for better muon identification and high momentum measurements.

Following the general design of the CMS detector, the muon system consists of the cylindrical barrel sections and two endcaps. In the barrel section, the uniform field, which is mainly enclosed in the return yoke, allows the use of Drift Tube chambers (DTs). This is not the case in the endcaps, thus technology insensitive to the field must be used.

In addition to the inhomogeneous magnetic field, high particle flux is expected in this region. Cathode Strip Chambers (CSCs) are chosen because of short drift distance O(mm), and reliable operation with the high flux. In both barrel and endcaps, Resistive Plate Chambers (RPCs) complement the muon identification and momentum measurements, as they provide an excellent timing measurement albeit their lower spatial resolution. All of these chambers work in a similar way. A muon ionizes gas while traveling the MS. An avalanche of electrons induces mirror charges on the cathode, which are measured. The barrel DTs and RPCs cover the pseudorapidity range of $|\eta| \leq 1.2$. The endcap CSCs covers the pseudorapidity range of $0.9 \leq |\eta| \leq 2.4$, while RPCs stop at $|\eta| = 2.1$. Overall they provide a detection area of $25000m^2$.

Drift Tube Chambers

The layout of DTs is shown in Fig. 14.

The r-ϕ plane is divided into 12 sectors, each with four MSs interleaved by the return yoke. Thus, combining 12 stations at a given r approximates are concentric layer. Divided up to five

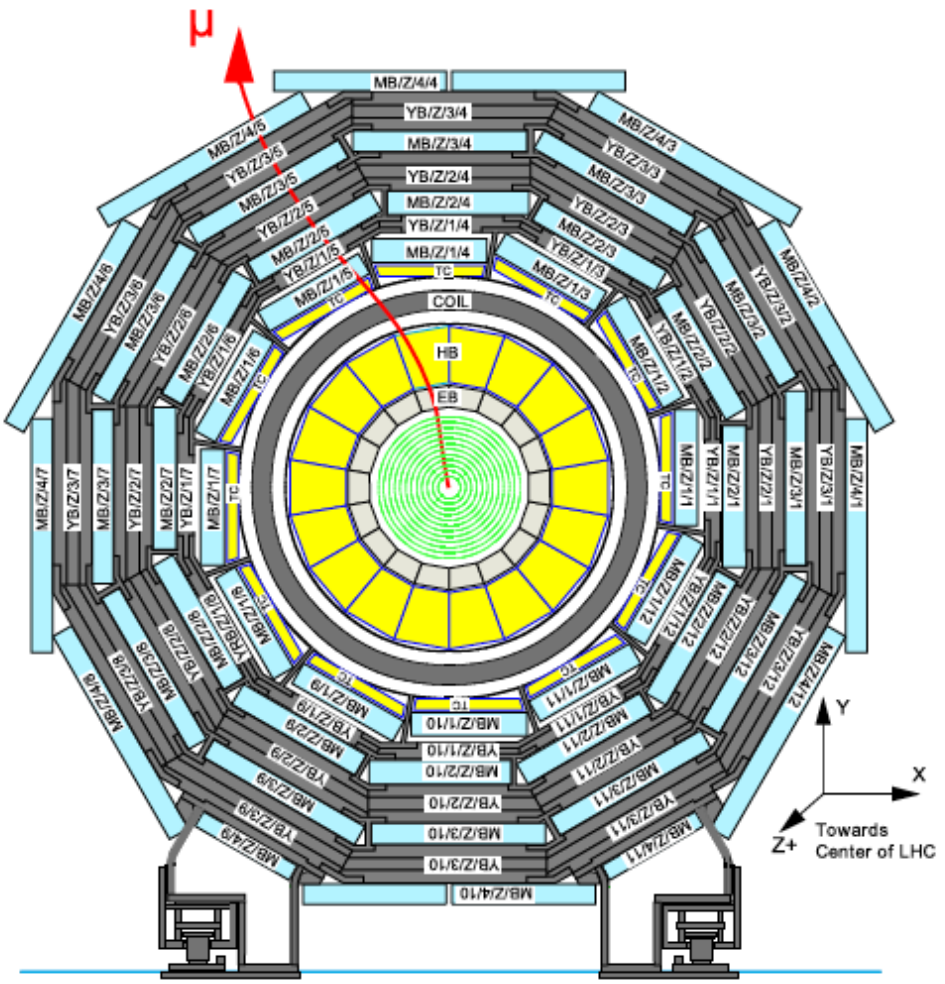

Figure 14: The DT layout in the r-ϕ view [35]. DTs are placed interleaved with return yokes (YB). As the red line (μ) shows, the magnetic field changes its direction in the return yokes.

wheels along the z-axis the barrel MS consists of 12 $\times$ 5 $\times$ 4 = 240 chambers. The inner three chambers contain three SuperLayers (SLs), of which the first and the third ones measure the ϕ coordinate and the second one the coordinate along z. The fourth MB is equipped with only two SLs, measuring only the ϕ coordinate.

All SLs are built from four layers of 11.5 $\times$ 42 mm^2 drift tube cells, which are not stacked exactly on top of each another but shifted by half a cell. This reduces ambiguities and avoids uninterrupted rays of inactive material pointing to the interaction point. The active elements of one cell consist of a central wire, two cathodes at the I-beams (supporting structure), and two field forming stripes near the anode wire on the plates. The maximum drift length is $21mm$, resulting a maximum drift time of $380ns$ for a gas mixture of 85% Ar + 15% CO_2. This time corresponds to less than 16 bunch crossings. 16 bunch crossings are too long to assign the hits

to muons if there are lots of hits present. Therefore DTs are used only in the barrel, where low particle flux is expected. The position of each hit is measured with an accuracy of $250\mu m$, and using eight hits improves the resolution to $100\mu m$ along ϕ.

Cathode Strip Chambers

As mentioned earlier, the DTs are not suitable in the endcaps because of the high particle flux and non-uniform field. Instead Cathode Strip Chambers are used arranged in four stations perpendicular to the beam axis on each end. Each station is arranged as a disk, consisting of two rings. The chambers are arranged with overlaps to avoid dead regions. The inner core is equipped with eighteen 20° chambers and the outer one with thirty-six 10° chambers giving full ϕ coverage.

A single chamber is made of seven trapezoidal panels forming six gas gaps. Within every gas gap a plane of 1000 wires with $3.2mm$ distance is arranged as illustrated in Fig. 15, forming multi-wire proportional chamber.

The wires are aligned along the ϕ direction. They provide a measurement of the radial coordinate with a precision of a few mm and precise time measurement to assign the muons to bunch crossings. All cathode panels are divided into strips aligned perpendicular to the wires hence along the radial coordinate. They are between $8.4mm$ wide near to beam and $16mm$ at the outer edge covering a constant $\Delta\phi$ width. Similar to the benefit of charge sharing, by weighting the charge distributed over several chambers a precision of about $150\mu m$ in ϕ is achieved.

Resistive Plate Chambers

The Resistive Plate Chambers (RPCs) provide precise timing information such that even under the LHC design conditions an unambiguous bunch crossing identification is possible. The system is thus crucial for triggering muons. The RPCs are complementary to the other muon detectors, adding redundancy. They provide a reasonable position measurement along the ϕ

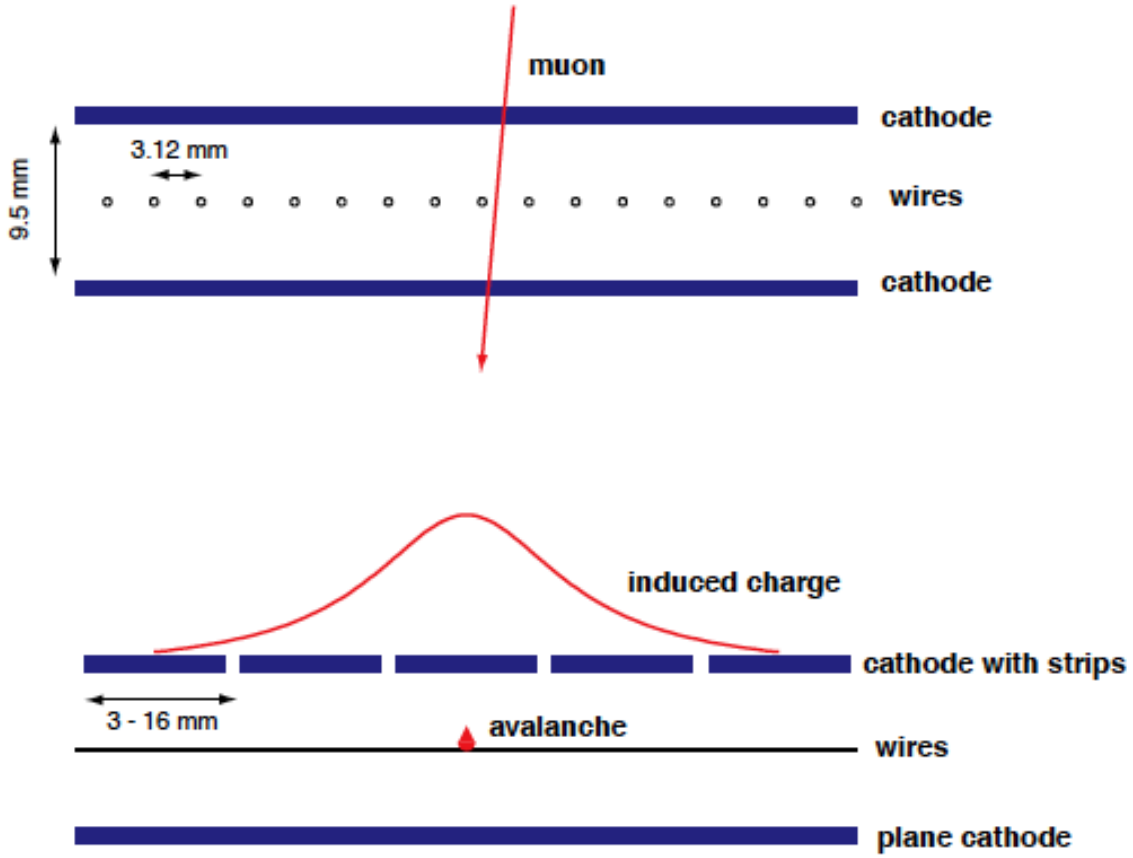

Figure 15: A slice of a CSC cell [35]. The signal produced by the crossing of a muon is illustrated.

direction as well as giving timing information. The layout of a double gap RPC used in CMS is illustrated in Fig. 16.

It is made of two pairs of bakelite plates confining two gas volumes. These gaps are filled with a mixture of 96.2% $C_2H_2F_4$, 3.5% iso-C_4H_{10} and 0.3% SF_6. The resistive plates are coated with graphite electrodes in order to apply the high voltage of approximately $10kV$. Each covers an area of about $2 \times 2m^2$. In the barrel the two innermost muon DT stations are sandwiched by two RPCs the two other stations carry only one RPC. This allows for a momentum measurement for even low energy muons absorbed in the iron return yokes before they reach the outer stations.

Each endcap muon station carries one RPC up to $|\eta| = 2.1$. They are read out by aluminum strips isolated from the graphite paint by a PET film. The RPCs are driven in the fast avalanche mode. However, they are less sensitive in this mode and provide small signals which must be

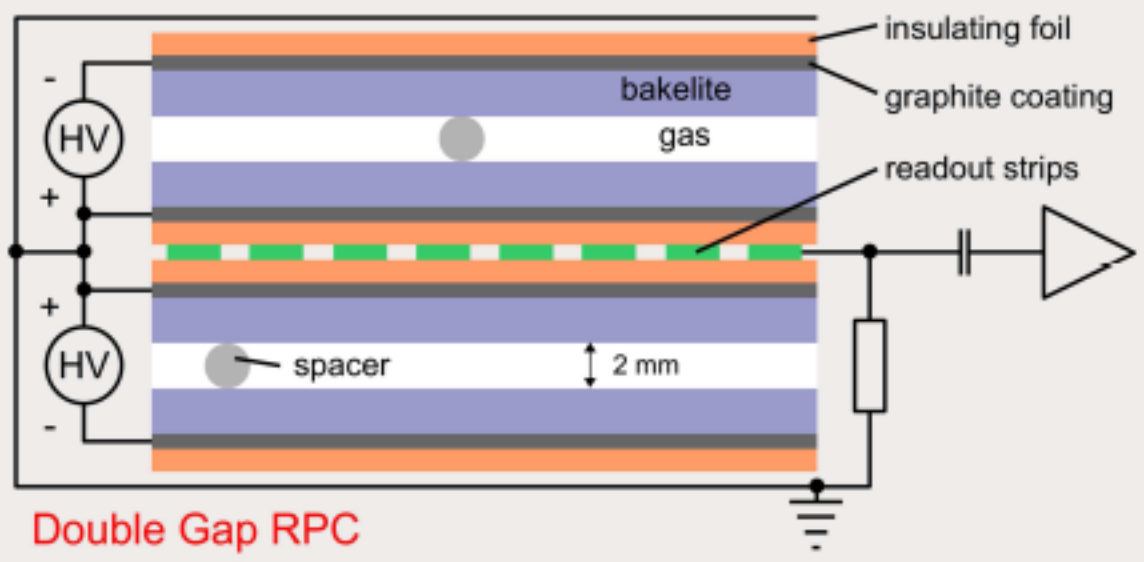

Figure 16: Schematic illustration of the double gap RPC [26]. One readout is shared with two gaps.

amplified by front end electronics. Double gap RPCs where one RPC gap is mounted on each side of the readout strips increase sensitivity and signal strength. Much like for the CSCs, the signals in adjacent chambers are weighted to gain a spatial resolution better than strip width.

3.4 Trigger System

We now discuss the trigger system in the CMS, based on reference [36]. With the CMS running under design conditions, more than 10^8 channels generate data every $25ns$. Even after zero-suppression, the order of $1MB$ per bunch crossing would have to be read out at the rate of $40MHz$, resulting in about $40TB/s$. This is far beyond computer technologies existing as of today, and, furthermore, most of them are actually contain no interesting interactions at all, and thus should be discarded.

Collision events have QCD interactions because of the high cross section. Meanwhile, rare processes beyond the SM are supposed to have much lower cross section to explain, at least partially, why such processes have remained undetected so far. Hence, a careful but very quick selection has to be made to ensure the most of interest physics events are saved on tape or disk while uninteresting ones are thrown away. Such a mission is performed by the online trigger system.

The trigger system is divided into two consecutive steps: Level 1 (L1) and High Level Trigger (HLT). The L1 is a different system from the HLT one, and the HLT has internal steps corresponding to the reconstruction levels. In this section, the HLT is referred as one entity and no detail is mentioned at each level ($e.g.$, L2, L2.5, and L3).

3.4.1 Level 1 Trigger

The L1 trigger (L1) is based on custom hardware pipeline processors (microprocessors with buffer memories), providing a decision every $25ns$ without dead time (no recording of data): the maximal rate of which L1 can handle is $100kHz$, and thus the total accept rate must be maintained below this number. Whenever the electronics sending out above the capability, the back pressure occurs, resulting a dead time. To find problems so that they can be fixed as soon as possible to avoid any dead time, online Data AcQuisition System (DAQ) and trigger shifters working at P5 keep their eyes monitoring for abnormal behaviors.

The L1 trigger searches for localized energy clusters in calorimeters and for tracks made from grouped hits in the MS. The trigger system is depicted in Fig. 17.

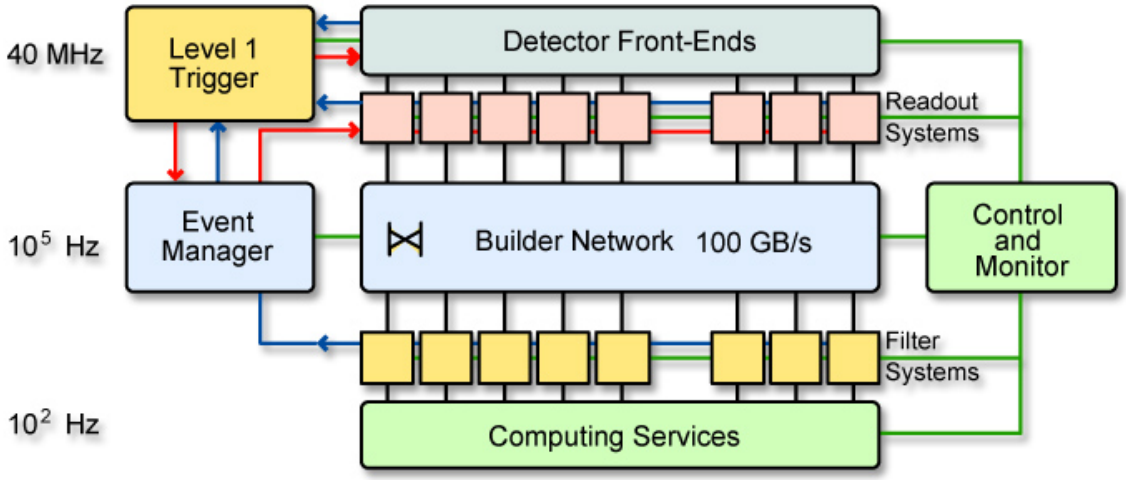

Figure 17: Two level trigger system used in the CMS [26]. Trigger primitives are sent to L1 and decision is made with buffer memories. Finally, the events are passed to HLT computing farm to achieve $100Hz$.

These are regional triggers that combine their information in a limited spatial region in order to form electron, muon, and jet candidates and rank them as a function of energy or momentum and quality. The four regional objects with the highest rank are all passed to the global muon

trigger and global calorimeter trigger which further selects the four highest rank objects from the entire detector and pass them to the global trigger which finally makes the decision at L1.

Events are passed to the next level only when energy and momentum of trigger objects exceeds predefined threshold values. The list of trigger thresholds, referred as a trigger menu, is subject to frequent changes with corresponding increase of the instantaneous luminosity and/or the beam energy. One thing worth keeping in mind is that the trigger capability is fixed and thus, as necessary, the trigger thresholds must be increased and/or prescaled. The prescaling means taking one in N events before the trigger decision, where N is the prescale number, resulting lower trigger efficiency for the trigger path. A common application of such scaling is for triggers for background and control samples. In general, all analyses prefer to have unprescaled triggers for signal. Otherwise, the signal events would be reduced by the factor of the prescale value at least.

The L1 tau trigger is documented in App. D, and the Web Based Monitoring (WBM) tools provide online check of the trigger rates based on the previous good runs as shown in Fig. 18.

This particular application is described in detail in App. E.

3.4.2 High Level Trigger

The High level trigger (HLT) is based on about 1000 Personal Computers (PCs) and reduces the event rate to about $100Hz$, which allows use of a tape archive system that can record data at the rate of $100MB/s$. The HLT makes use of the high resolution data that are read out from pipelined memory. Utilizing such information the HLT PC farm runs algorithms to determine the type and multiplicity of particles in the events passed from L1. This collection then runs through the possible trigger paths and a trigger fires when the requirements are met. The event thus passed at least one trigger path is written to tape.

The HLT algorithms are like the ones used in the offline reconstruction, which collect information from the whole detector to determine the number and types of particles found in the events. There are different paths with all kind of different collection of requirements including: iso-

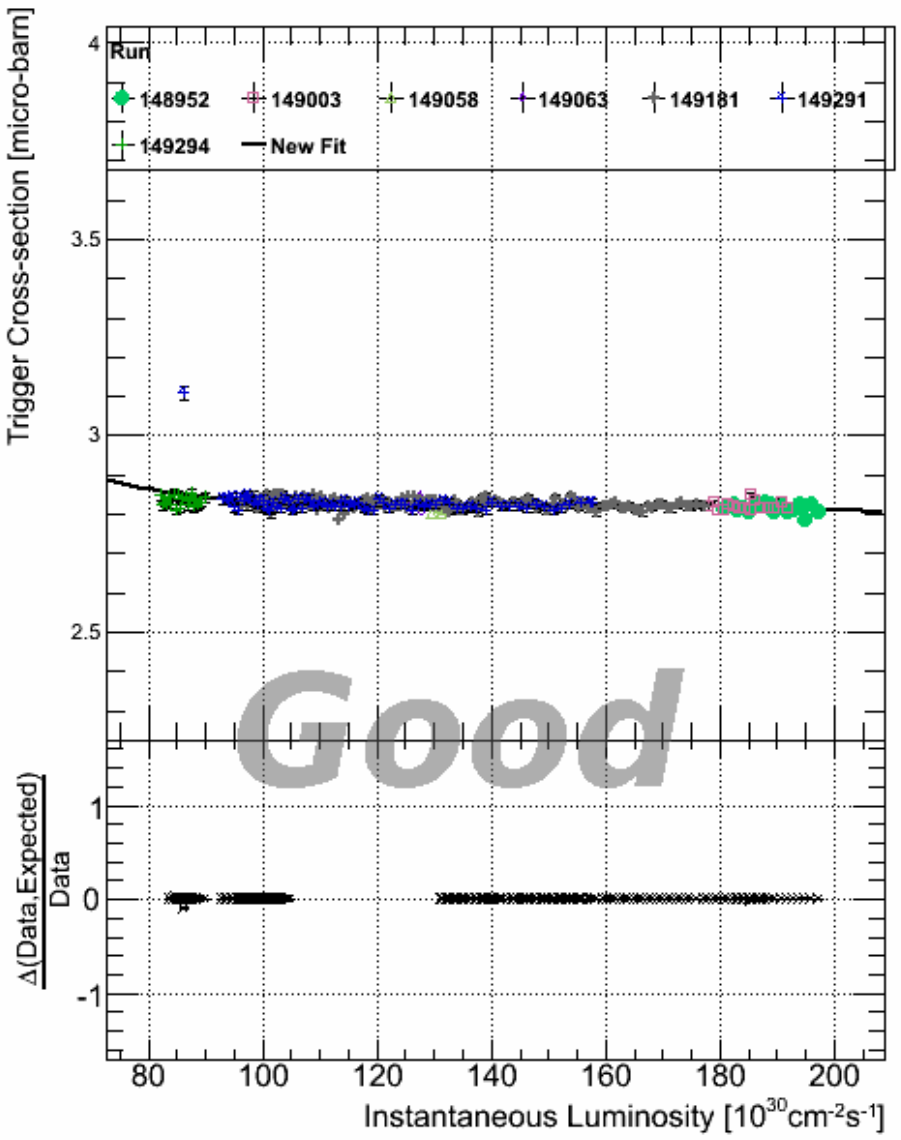

Figure 18: Single jet with uncorrected energy of 60 GeV trigger cross section provided by WBM team [37]. Trigger cross section, trigger rate divided by the instantaneous luminosity, is fitted across multiple runs. The difference between expected value from previous good runs is shown in the lower half. The fit result is used for online monitoring via one of the WBM applications, 'TriggerRates.'

lated and non-isolated electrons, muons, taus, jets, $E_{\mathrm{T}}^{\mathrm{miss}}$, and the sum of jet E_{T} s with certain threshold values. A muon is considered isolated if the energy in cone of $\Delta R < 0.24$ is below a certain threshold: the transverse energy must be less than 2 to 4 GeV in the calorimeter and transverse momentum must be less than 0.8 to 1.2 GeV in the tracker.

It is possible to form a trigger as any combination of particles and available quantities ($e.g.$, one electron and $E_{\mathrm{T}}^{\mathrm{miss}}$). This results, in general, shorter trigger decision times with the same decision although it becomes slightly complicated. When interpreting HLT path with similar

ones, a special attention is needed since the similar trigger may have different L1 seed(s) and/or the intermediate HLT requirements ($e.g.$, HLT_Mu5 and HLT_Mu15 may have different L1 seeds).

For every event, a list of the trigger decisions is stored, so that analysts can access this information and use it to select events for their interest. In this analysis, all combination of active triggers are used in electron and muon data streams. The justification of this treatment is given later in the trigger section. The rationale is, roughly speaking, always at least two electrons/muons are required to be reconstructed offline, meaning the inefficiency of single lepton triggers must be squared at least, as long as the reconstructed leptons have moderate p_{T} spectra. Assuming about 90% of single trigger efficiencies, the inefficiency is of the order of O(1%), which is small enough to be neglected with respect to other uncertainties like the luminosity measurement. For 3 and 4-lepton signals, optimization of offline cuts on data is less difficult because of low SM backgrounds. The details are provided in Sec. 5.

The prescales can be applied at the HLT as well with one more complication: dynamic prescales. The prescale value is usually set at the beginning of a run, and kept the same through the run. Technically, however, it can be changed during a run for HLT. This will be deployed in the runs expected in 2011, but so far no dynamic prescales have been applied for physics runs.

3.5 Luminosity

The collected luminosity has to be certified for good data quality and which is done centrally through the Run Registry (RR). The certified luminosity is the integrated luminosity, which determines total number of events, with cross sections of various processes and trigger efficiencies.

There are two methods to measure the luminosity. First by determining the beam parameters and calculating the luminosity with equation 3.1.

As it is rather difficult to measure the beam parameters at the IP, an uncertainty of $\sim$ 10% is expected. Another way to determine the luminosity is adopted in the TOTEM experiment [38] .

It is designed to determine the total cross section of the LHC and the rate of inelastic and elastic processes. These quantities can in turn be used to fix the integrated luminosity. The luminosity can be calculated using

$$N_{incl} + N_{el} = \sigma \int L dt. \tag{59}$$

The optical theorem relates the total cross section σ_{tot} to the imaginary part of the forward scattering amplitude. The latter is related to the differential elastic event rate per momentum transfer t,

$$\sigma_{tot} = \left(\frac{dN_{el}}{dt}\right)_{t=0} \frac{16\pi}{N_{el} + N_{inel}} \frac{1}{1+\rho^2} \tag{60}$$

with the ratio ρ between the real and imaginary part of the forward scattering amplitude. TOTEM measures $\frac{dN_{el}}{dt}$ and N_{el} with its roman pots and N_{inel} using its forward inelastic detector and the CMS forward HCAL.

The offline luminosity measurements are done making use of standard candles. Drell-Yan production of $Z \rightarrow ll$ and $W \rightarrow l\nu$ provide this possibility as these production rates can be measured precisely and its cross section is high enough to have reasonable statistics in a short time. In this analysis, the official number announced by the luminosity group for the uncertainty, 11%, is used.

3.6 Computing with Clusters of PCs

The computing capability of PCs exponentially has grown over the last few decades as predicted by Moore's law. However, there are limitations foreseen from physics. The speed of light cannot propagate faster/slower than its fixed value in a certain medium. This fact roughly sets the maximum CPU clock cycles as $f = c/L \sim$O(GHz) typically with available technologies as of today, where L is the total length of wiring in the CPU. To gain higher the clock cycle, L must be shortened as short as possible. However, the quantum effect eventually comes in when adjacent wires with sufficiently high electric voltage. This causes degradation in the power efficiency of the CPUs.

Instead, one may take another path to effectively increase computation power. If a certain

process is independent from the rest of data, such a process can be detached from the rest of the data. The data can be divided into the minimum unit (say, an event), and the units (events) may be processed at the same time in parallel. Then the effective computing power increases linearly in ideal a case at the cost of buying multiple CPUs. In other words, the process is scalable. In modern computing, usually a user sends a set of jobs to the cluster of PCs.

The CMS experiment would collect Peta Bytes of data, and several thousand physicists all over the world start analyzing it once the access granted. Additionally large amount of processing power is needed for Monte Carlo (MC) simulation. It is simply unrealistic to have only one site stores everything and provides computing power to everyone. Hence it has been agreed to distribute the computing system geographically. Along with the necessary high speed connections between all sites, this is then called the LHC Computing Grid (LCG) [39].

The LCG consists of several hierarchical tiers. Raw data delivered by the detector is first stored on tape at the T0 (CERN). Fast reconstruction for calibration and monitoring purposes is performed also at the T0. After dividing the data into streams depending on the HLT decision, the streams are sent to six T1 centers located around the world. After full reconstruction, the T1s distribute the data to a high number of T2s which are usually located at a single institution.

At T2s, a user may run his/her analysis jobs. The T2s are also used for MC event generation and detector simulation. The particular datasets a user wants to access are not necessarily located at his/her home institution. Thus, the CMS has created a set of software tools used for this purpose with the user interface, CMS Remote Analysis Builder (CRAB). Its basic task is to take the user's programs, pack them up, and send this to a computer on the grid with direct access to the desired dataset. After successfully running the program, the output is then collected and sent back to the user.

4 Reconstruction

The raw data from the detector contains all the information relevant to analyzing interesting physics. However, the raw data are quite different from the 4-vectors of produced particles. Once data is written to tape the offline reconstruction follows. As it is not crucial to do the offline reconstruction within a short time scale, unlike for the trigger system, all detector information is used and all possibilities of particle trajectories are checked and compared to each another. The physics objects that are used in this analysis are muons, electrons, jets and $E_{\mathrm{T}}^{\mathrm{miss}}$, taus and the reconstruction methods follow.

4.1 Muons

Muons are the only particles that travel through the whole detector without losing most of their energy, and leave hits in the muon system. Muons with a p_{T} above ~ 3 GeV/c are not stopped in the detector and their energy is not known, but their tracks are used to determine the transverse momenta making use of the curvature of trajectories

$$p_{\mathrm{T}}[\mathrm{GeV}] = \frac{B[T]\rho[m]}{3.3}. \tag{61}$$

The transverse momentum is linearly magnetic field dependent. The alignment of the muon system of the tracker and the alignment with respect to each other is important as well to get the bending right.

A muon passing through the tracker and muon system deposits energy by ionization. Muons with $p_{\mathrm{T}} < 100$ GeV/c do not radiate significant energy. This deposit would be recoded as a hit. A series of hits are converted into a single track which corresponds to a muon trajectory in the magnetic field. In this analysis, a muon is required to be global, meaning a track must exist in the inner tracker and MS and these two tracks have to be matched together.

Muon reconstruction starts with DT, CSC, and RPCs. Hit positions in the MS define where a muon passed through. First, the innermost and outermost hits detected in the CSCs or DTs are

combined to make track segment candidates, and for each combination the number of hits fitted to this particular candidate is counted. If a sufficient number of hits is assigned to the candidate, it becomes a track segment. This segment is then extrapolated to other MS subdetectors, using a Kalman Filter technique which accounts for multiple scattering and other material effects. If suitable hits are found there, the hits are combined with the track segment to form a new one and a new fit is repeated until all layers up to the outermost are included. Then a backward Kalman filter technique is used to work its way back to the innermost layer. The track parameters are defined performing a fit with all associated hits. Finally the track is extrapolated back to the IP and a vertex constrained fit is applied updating the track parameters. Such a track is defined to be a standalone muon. Extrapolating back the standalone muon to the inner tracker and taking into account material effects defines a region of interest in the tracker where the muon should have come from. Pairs of hits in the region are combined to form a seed for the muon trajectory candidate where the two hits forming a seed must come from different layers. These layers must be pixel or stereo strip layers. Then again Kalman filter technique is used to reconstruct tracks with the information of all layers. As the last step the tracker track segments are combined with standalone track segments to form global tracks and a final fit is performed. Such a track is defined to be a global muon.

The muon track quality is characterized by following parameters:

- χ^2/n.d.f.: The χ^2 of the fitted track divided by the number of degrees of freedom. A usual value for a good muon is < 10.
- Number of valid hits: The number of valid hits that are assigned to a muon track. An good muon has few tens of hits.
- d_0: the muon impact parameter in the x-y plane with respect to the primary vertex normally $< 0.2\ cm$

The global muon efficiency is shown in Fig. 19.

After the reconstruction further quantities defining the muon quality are calculated with a template likelihood method in the calorimeters and MS. The muon calorimeter compatibility is

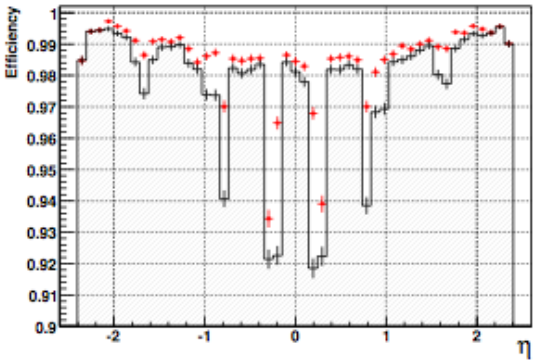

(a) Efficiency as a function of pseudorapidity.

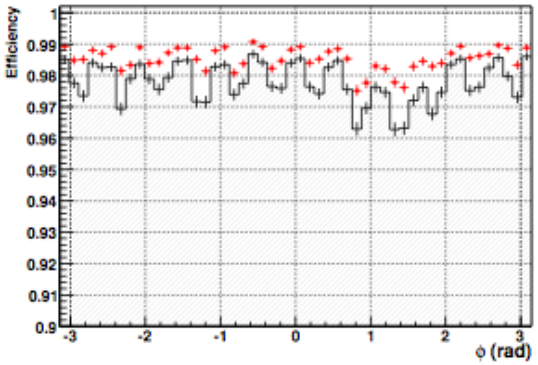

(b) Efficiency as a function of ϕ.

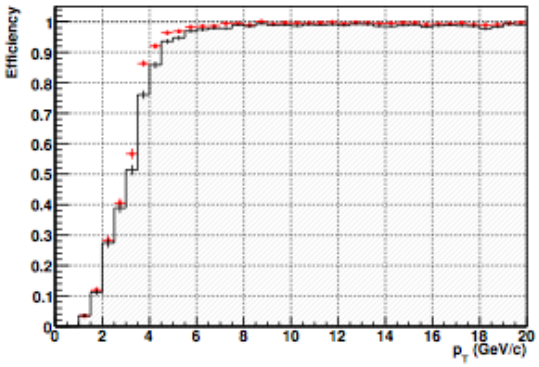

(c) Efficiency as a function of p_{T}.

Figure 19: Efficiency of the reconstruction in the muon spectrometer as a function of η, ϕ and p_{T}, with (red cross) and without (dashed area) RPC in the track reconstruction [40].

a number that quantifies how MIP-like the muon is in the calorimeters. The muon segment compatibility is a number that quantifies how prompt muon like the muon is in the MS.

The muon isolation is useful to distinguish between prompt muons coming from heavy particles like Z boson decay, and non-prompt muons produced in b-jets. In a cone of $\Delta R = \sqrt{\Delta\phi^2 + \Delta\eta^2} < 0.3$ around the muon's trajectory the p_{T} of other tracks is summed up in the tracker and calorimeters to determine the tracker and calorimeter isolation. An inner cone of $R < 0.01$ is removed in order not to count p_{T} leaking from the muon itself. In this analysis, only global muons are used with additional check as a MIP by requiring a muon satisfying both the global and tracker muon selections. Standalone and calo muons are not used at all.

Muons with p_{T} <200 GeV, the transverse momentum resolution of the MS is deteriorated by multiple scattering in the material before the first muon station, as mentioned earlier. The

momentum resolution in this region is therefore dominated by the inner tracker which provides a resolution of order of 1 %. For muons with higher momentum, the combined reconstruction in both the inner tracker and muon system provides a resolution of the order of 10% up to p_{T} = 1 TeV. In the endcaps the resolution is slightly lower but still in the same order of magnitude. The reconstruction efficiency of global muons is between 95 and 99%, with drops at transition regions in the barrel, and the barrel to endcaps [40].

4.2 Electrons

An electron, as a light electromagnetic particle, interacts with the magnetic field leaving a curved trail in the tracker, and deposits most of its energy in the ECAL. The reconstruction of electron naturally relies on the pixel detector, silicon strip tracker, and the ECAL. This section follows reference [41].

As for muons, the emphasis here is on the reconstruction of prompt electrons. There is a considerable amount of real electrons originating from heavy quark decays, typically non-isolated electron within jet products. Such a non-prompt electrons are not of primary interests in this physics analysis. Another important source of contamination is the conversion of photons in the inner tracker. However, most conversions can be removed by checking all combinations of reconstructed tracks and cutting on angular distribution and distance between tracks. Prompt electrons are considered hereafter.

The reconstruction is not simple even for prompt electrons. Electrons traversing the inner tracker radiate bremsstrahlung photons and the energy reaches the ECAL with a significant spread in ϕ direction. The ECAL clustering is designed to take into the ϕ spread and collect the bremsstrahlung energy. Supercluster-driven pixel seed finding is then used to initiate the building of trajectories in the inner tracker. The electron track reconstruction relies on a dedicated Gaussian Sum Filter (GSF) using a specific energy loss modeling.

The estimate of electron energy combines tracking and ECAL measurement. Track-based information dominates in lower p_{T} region and ECAL information dominates in higher p_{T} region.

The electron direction is obtained from the track associated to it.

The supercluster and track reconstruction algorithms are reviewed in the following subsections.

4.2.1 Supercluster

Most energy of an electromagnetic shower initiated by electrons is contained in several crystals of the ECAL. With the test electron beam, for energy of 120 GeV, in the barrel, electrons deposited about 97% of their incident energy in 5×5 crystal window. The array design has an advantage in energy measurement because local containment corrections can be applied to account for the variation of the measured energy as a function of the shower position with respect to the cluster boundary.

The bremsstrahlung complicates the situation. Integrating radiated energies along the electron trajectory, the effect can be large. About 35 % of the electrons radiate more than 70% of their initial energy before reaching the ECAL. In about 10% of the cases, more than 95% of the initial energy is radiated. The superclustering algorithms are designed to collect the energies. Within the energy range considered in this analysis, the basic hybrid and island clustering algorithms are used for electrons in the ECAL barrel and endcaps respectively.

The hybrid algorithm attempts to profit from the simple geometry of the ECAL barrel and exploit the properties of the lateral shower shape in the transverse direction while dynamically searching for separated energy in ϕ. In the language of hybrid superclustering, a seed cluster is a collection over ϕ of contiguous dominoes made of 3 to 5 crystals in η and separated by other such collections by a valley where less than 100 MeV is observed in a domino.

The island algorithm used in the endcap region builds clusters by connecting row of crystals containing energies decreasing monotonically when moving away from a seed crystal. Then superclusters are built by collecting other island clusters in a ϕ road in both directions around each island clusters starting from a list of clusters ordered in E_{T}.

4.2.2 Tracking

The track reconstruction can be summarized as following:

- First, seeds are sought in the inner tracker.
- Second, all possible trajectories are constructed outward for a given seed.
- Third, ambiguities among the possible trajectories are solved with trajectory cleaner and a maximum number of track candidates is kept.
- Fourth, the final fit of the track is performed with trajectory smoother which uses all the collected hits to estimate the track parameters at each layer through backward fit.

A seed is created from two hits in the inner-most detector, the pixel detector. To reconstruct electrons, it is not necessary to try all possible trajectories. Instead, only relevant hits may be used. The relevant ones are determined from the supercluster position. The supercluster-pixel matching takes advantage of the fact that the energy-weighted average impact point of the electron and associated external bremsstrahlung photons, as calculated using information from the supercluster in the ECAL, coincides with the impact point that would have been measured for a non-radiating electron of the same initial momentum.

The hit positions in the pixel layers are predicted by propagation of the energy weighted mean position of the supercluster backward through the magnetic field under both charge hypotheses toward the pixel detector. A first compatible hit is then sought for in the innermost pixel layer within a loose $\Delta\phi$ window and Δz interval. In cases where no hit is found in the innermost layer, the first hit is looked in the next layer. When a first compatible hit is found, a new estimated z_0 for the z coordinate of the primary track vertex is calculated combing the pixel hit found and calorimetry information in the r-z plane. A new trajectory is then propagated to find a second pixel hit in the next pixel layer. Once pixel layers are investigated, the hit search process moves to the next silicon layers. Then an extrapolation is performed using the Bethe-Heitler modeling of the electron energy losses and a GSF in the forward fit. This procedure is iterated until either the last tracker layer is reached, or no hit is found in two subsequent layers.

The trajectory state at each layer is computed as the weighted mean of the predicted state and of the measured hits.

The track quality is determined in terms of a χ^2. If many hits are found on a compatible layer, many candidate trajectories are grown in parallel. In order not to lose efficiency at this stage, no specific χ^2 cut is applied in the building steps of the GSF tracks, but only the best two candidates are kept. A minimum of five hits is required to create a track. The efficiency of track reconstruction is shown in Fig. 20, and the resolution of electron p_{T} is shown in Fig. 21.

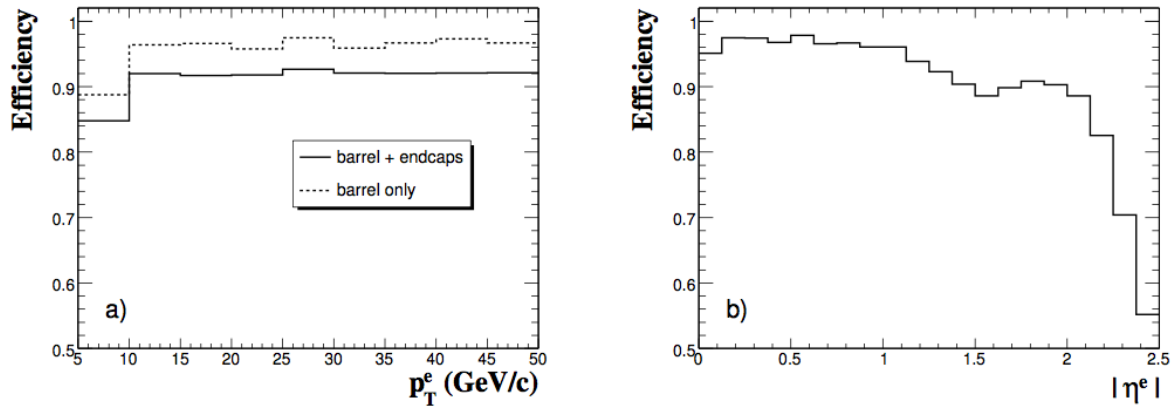

Figure 20: Electron track reconstruction efficiency (a) as a function of p_{T} and (b) as a function of $|\eta|$, for electrons uniformly distributed in between 5 and 50 GeV. In (a), the efficiency is shown averaged over the full ECAL barrel and endcaps η range (full line) and for the barrel only (dotted line) [41].

The selection of electron used in this analysis is η dependent and it is summarized in Table 6.

variable type	barrel	endcaps
$\sigma_{i\eta i\eta}$	0.01	0.03
Δ_ϕ	0.8	0.7
Δ_η	0.07	0.009
E_{HCAL}/E_{ECAL}	0.12	0.05

Table 6: Electron cuts in the barrel and endcaps. $\sigma_{i\eta i\eta}$ is the weighted cluster RMS along η inside 5×5 region of supercluster. $\Delta\phi$ is the difference of ϕs between supercluster and position of inner track extrapolated from the interaction vertex. $\Delta\eta$ is the difference of ηs between supercluster and position of inner track extrapolated from the interaction vertex. E_{HCAL}/E_{ECAL} is the ratio of HACL and ECAL energies associated with the electron.

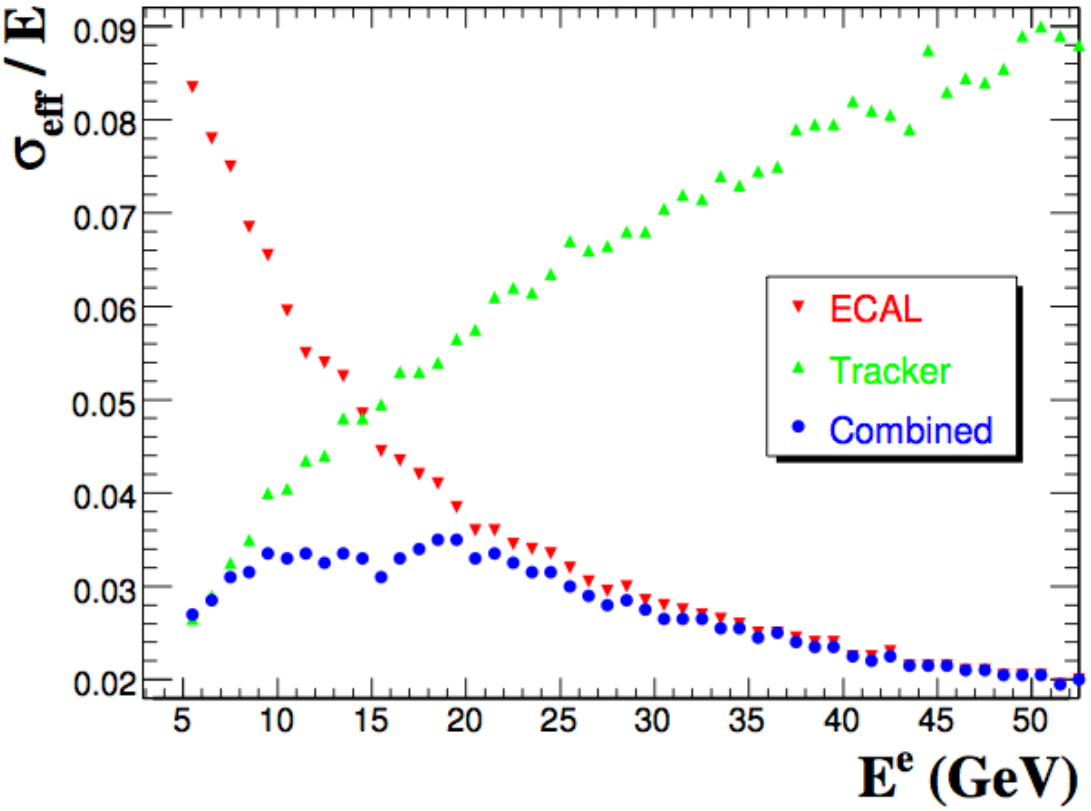

Figure 21: The resolutions as measured by the relative effective RMS of the corrected supercluster energy (downward triangles), the reconstructed track momentum at origin (upward triangles), and the combined electron momentum estimate (circles) as a function of the electron incident energy for electrons in the ECAL barrel [41].

4.3 Jets and Missing Transverse Energy

A jet is an object that contains mostly pions, kaons, and other hadrons. π^0 mesons can decay electromagnetically such that a jet has in general electromagnetic and hadronic contributions. The hadronization of a single quark or gluon to numerous hadrons happens due to the confinement in the QCD. Gluons or quarks, that are radiated from a hard scattering initial parton, produce an accumulation of aligned hadrons.While traveling through the detector they deposit most of their energy in the calorimeters, except neutral hadrons with long life times.

It is better if the type of quark or gluon can be identified in the experiment. However, only c and b-jets have a promising probability of being identified (top quarks are different in a sense W decay is involved).

The objects, a jet and $E_{\mathrm{T}}^{\mathrm{miss}}$, are both built from the same source: the signals in calorimeter

towers (calotowers) with some corrections applied. Approximately nine ECAL crystals cover one HCAL cell. A calotower represents the jet energy in a certain direction on the $\eta - \phi$ plane. A jet uses a combination of the calorimeter activity in clustered cells. The second object built from calotowers is the total transverse energy balance of all calorimetric depositions.

4.3.1 Jets

A jet is a high p_{T} hadronizing particle which leads to a bunch of particles, all going into roughly in the same direction. If they enter the calorimeters they cause a broad area of calorimeter cells to light up. In any physics analysis, not calorimeter hits, but the 4-vector of the original hadronizing particle is of primary interest. To reconstruct as much information about the hadronizing particle as possible, the hits must be regrouped. In this analysis only Anti-k_T (AK) jet clustering algorithm is used, and the detail follows reference [42].

The Anti-k_T Algorithm

The AK algorithm has properties of infrared and collinear safe (to compare with theoretical predictions) like some other jet clustering algorithms. The infrared safe jet algorithms are less affected by the addition of soft particles, and the collinear safe jet algorithms do not split collinear particles. The important features of the AK jets can be summarized in two points: being resilient to irregularities provoked by soft radiation, and less susceptible to back-reaction (which will be discussed later in this subsection).

The AK algorithm is a combination of k_T and Cambridge/Aachen algorithms. Two distances are defined as

- d_{ij} = distance between two entities
- d_{iB} = distance between a jet and the beam

Two entities are combined based on the smallest d_{ij} and if d_{iB} is less than a certain threshold value, the entities assigned to i-th jets are removed from a list of entities, and now the i-th jet

is saved. The process is repeated until no possible combination left. The AK algorithm defines the distances as

$$d_{ij} = min(k_{ti}^{2p}, k_J^{2p}) \cdot \frac{\Delta_{ij}^2}{R^2} \quad (62)$$

$$d_{iB} = k_{ti}^{2p}, \quad (63)$$

where $\Delta_{ij}^2 = (y_i - y_j)^2 + (\phi_i - \phi_j)^2$ and k_{ti}, y, ϕ are the transverse momentum rapidity, and azimuthal angle of particle, respectively. In addition to the usual jet cone radius parameter R, a parameter p is added to govern the relative power of the energy versus geometrical Δij scales. The AK is the one with p = -1.

General behavior of the AK algorithm is apparent in a few hard particles and many soft particle case. The d_{1i} = min$\left(\frac{1}{k_{t1}}, \frac{1}{k_{ti}}\right) \cdot \frac{\Delta_{1i}^2}{R^2}$ between a hard particle and a soft particle i is exclusively determined by the transverse momentum of the hard particle and the Δ_{1i} separation. The d_{ij} between similarly separated soft particles is much larger because of its p_{T}. Therefore soft particles tend to cluster with hard ones long before they cluster among themselves. If a hard particle has no hard neighbors within a distance $2R$ then it will simply accumulate all the soft particles within a circle of radius R resulting in a perfectly conical jet. If another hard particle 2 is present such that $R < \Delta_{12} < 2R$ then there will be two hard jets.

For a general situation, $k_{t1} \sim k_{t2}$, both cones are clipped with the boundary b between them defined by $\frac{\Delta_{2b}}{k_{t2}}$. The key feature is that the soft particles do not modify the shape of the jet while hard particles do ($i.e.$, only hard jets defines jet boundaries). The jet area of the AK algorithm can be computed order by order given that it is infrared safe.

In most of analyses, only high p_{T} jets are of primary interest. However, the measurement can be affected by the soft jets from pile up and/or underlying events as well. Soft energy will have been added to each jet, and additionally the particle assignment to each jet may be changed, called a back reaction. If the soft particles that are added have a density ρ of transverse momentum per unit area then for usual sequential recombination algorithms, the probability, $\frac{dP}{d\ln \Delta p_{\mathrm{T}}^B}$, of having a back reaction of Δp_{T}^B is O$\left(\frac{\alpha_s \rho}{\Delta_{p_{\mathrm{T}}^B}}\right)$ for $\Delta p_{\mathrm{T}}^B \leq \rho^4$. For the AK, the probability of back-reaction is suppressed not by the amount of back reaction itself but by

the jet transverse momentum. Therefore the AK is chosen.

Jet Energy Scale

The HCAL is a sampling calorimeter. Thus not the total jet energy is measured as the jet deposits energy in the absorber material as well, and long lived neutral hadrons can escape from the detector without depositing much energy. Both the detector as well as the clustering algorithms tend to lose a certain fraction of a jet energy. On the other hand, the pileup events (additional particles with a high collision rate) usually add energy to each jet. To make things worse both effects are η dependent. Hence the jet energy must be corrected to really represent the underlying physics. The energy response is shown in Fig. 22.

The correction, which is to gain a flat jet response in η, called L2 correction. To accomplish this correction factors for various η and jet p_{T} regions are determined by comparing calorimeter jets to associated generator level jets. Finally these factors are derived from jet balance in dijet events. After leveling out the response in η, the correction, which aims at adjusting the absolute jet energy in a control region, $|\eta| \leq 1.3$, is called L3 correction. Hence a p_{T} dependent correction function is determined by again comparing the calorimeter jets to matched generator level jets.

By balancing γ/Z+jets events, the function parameters can be obtained. The corrections determined for the jets are then used to correct the $E_{\mathrm{T}}^{\mathrm{miss}}$ too. The $E_{\mathrm{T}}^{\mathrm{miss}}$ is divided into clustered and unclustered energy. The former is the energy in calotowers assigned to a jet, and the latter is everything left. The clustered energy is then corrected using the above jet correction. The uncertainty is ~ 5 % after the correction [43].

4.3.2 Missing Transverse Energy

The CMS detector covers almost the full 4π solid angle. However, complete hermeticity cannot be achieved since at least two openings for the beam pipes are necessary. Hence high energy low p_{T} particles escape from detection and therefore missing total energy is unknown. However

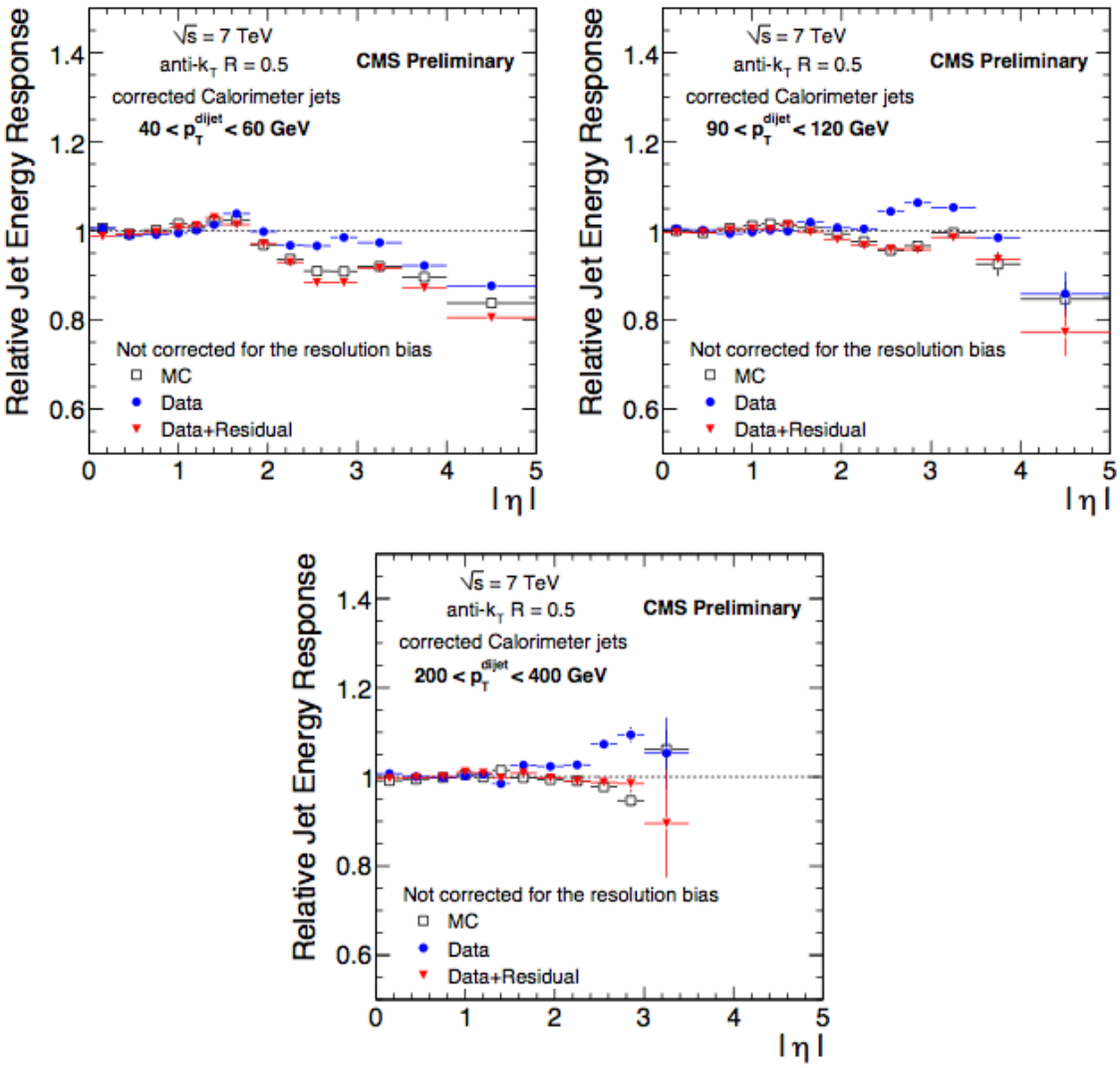

Figure 22: Relative response for CALO jets in various p_T^{dijet} bins. Open squares: simulation, T solid circles: data, solid triangles: data corrected with the residual calibration [43].

these undetected particles carry low transverse momentum and calculating the imbalance of transverse energy in the calorimeter is still useful.

To reconstruct the missing transverse energy, the transverse energy of all calorimeter towers are added up as a vector sum. The calotowers are defined in a two dimensional space in $\eta - \phi$ [44]. In transverse plane,

$$\overrightarrow{E_{\mathrm{T}}^{\mathrm{miss}}} = -\sum_{1}^{n} E_n \cdot (sin\theta_n \cdot cos\phi_n,\ sin\theta_n \cdot sin\phi_n), \tag{64}$$

where n is the number of active calotowers. Its magnitude is referred as $E_{\mathrm{T}}^{\mathrm{miss}}$.

$\overrightarrow{E_{\mathrm{T}}^{\mathrm{miss}}}$ is corrected for various effects. As just described, jets undergo jet energy scale correc-

tions which of course have an impact on $\overrightarrow{E_{\mathrm{T}}^{\mathrm{miss}}}$. These are called Type I corrections and can algebraically be written as

$$\overrightarrow{E_{\mathrm{T}}^{\mathrm{miss}}}_{typeI} = \overrightarrow{E_{\mathrm{T}}^{\mathrm{miss}}} - \sum [\overrightarrow{p_{\mathrm{T}}}^{cor}_{T_i} - \overrightarrow{p_{\mathrm{T}}}^{raw}_{T_i}]. \tag{65}$$

The next step accounts for unclustered energy response and out of cone energy are done on top of Type I correction according to the formula

$$\overrightarrow{E_{\mathrm{T}}^{\mathrm{miss}}}_{typeII} = \overrightarrow{E_{\mathrm{T}}^{\mathrm{miss}}}_{TypeI} + c \times \sum [\overrightarrow{p_{\mathrm{T}}}^{cone7}_{T_i} - \overrightarrow{p_{\mathrm{T}}}^{cone5}_{T_i}], \tag{66}$$

where cone5 and 7 refer to the size of jet in R. The comparison of raw and corrected $E_{\mathrm{T}}^{\mathrm{miss}}$ is shown in Fig. 23.

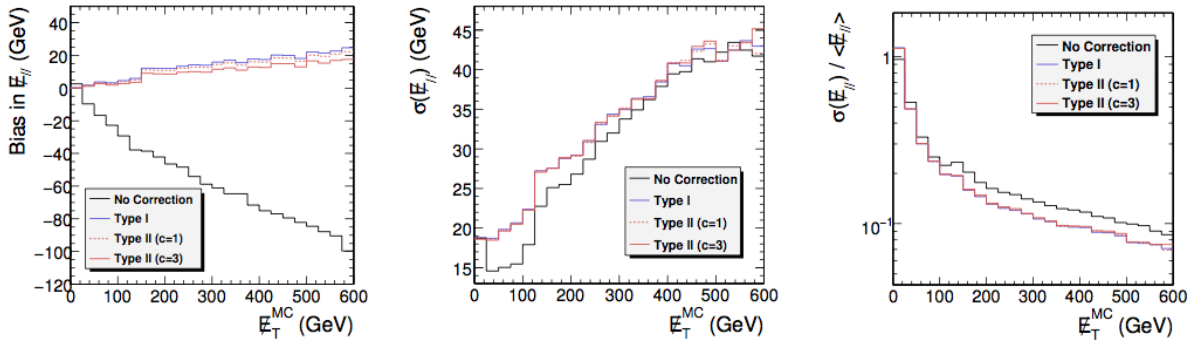

(a) Bias in $\not\!\!E_{\parallel}$. (b) Absolute resolution of $\not\!\!E_{\parallel}$. (c) Relative resolution of $\not\!\!E_{\parallel}$.

Figure 23: Comparison for raw $E_{\mathrm{T}}^{\mathrm{miss}}$ and type I and II corrections in the $W \rightarrow e\nu$+ jets samples [44].

A further applied correction accounts for muons. $\overrightarrow{E_{\mathrm{T}}^{\mathrm{miss}}}$ needs to be corrected with muons p_{T} and its energy deposits in calorimeters as they are MIP-like and their p_{T}s are reconstructed using hits from the tracker and muon system. After identifying those entries in the calorimeters left from muons, $\overrightarrow{E_{\mathrm{T}}^{\mathrm{miss}}}$ is re-calculated as

$$\overrightarrow{E_{\mathrm{T}}^{\mathrm{miss}\prime}} = \overrightarrow{E_{\mathrm{T}}^{\mathrm{miss}}} + \sum \overrightarrow{E_{\mathrm{T}\mu}} - \sum \overrightarrow{p_{\mathrm{T}\mu}}. \tag{67}$$

The resolution of the $E_{\mathrm{T}}^{\mathrm{miss}}$ is in general sensitive to all kinds of detector effects, as it is a global observable and thus determining the various effects on its performance is challenging. The

resolution is parametrized as

$$\sigma(E_{\mathrm{T}}^{\mathrm{miss}}) = C \cdot \sqrt{\sum_{1}^{n} E_{\mathrm{T}}}, \tag{68}$$

where the C is a jet resolution of calorimeter jets, and $\sum_1^n E_{\mathrm{T}}$ is a scalar sum of all calorimeter hits. Given the good p_{T} resolution of the MS, the dominant source of the uncertainty is expected to come from jets. The important feature of the resolution is the square-root dependence on the scalar E_{T}. This behavior can be understood as a random walk problem in statistics. If the underlying events deposit same energy in random direction, then the vector sum of the energy just cancel out among themselves. In practice, however, underlying events do not deposit the same energy everywhere, and still the increase, on average, grows non-linearly.

Muons and neutrinos give rise to large $\overrightarrow{E_{\mathrm{T}}^{\mathrm{miss}}}$. However, the muon p_{T} is reconstructed as described earlier, and $\overrightarrow{E_{\mathrm{T}}^{\mathrm{miss}}}$ must be corrected for muon p_{T}s and its energy deposits. Therefore only neutrinos are the SM particles contribute to $\overrightarrow{E_{\mathrm{T}}^{\mathrm{miss}}}$. Beyond the SM, many theories predict weakly interacting particles that would add to $E_{\mathrm{T}}^{\mathrm{miss}}$ distribution. It is important to understand detector effects that would add to $E_{\mathrm{T}}^{\mathrm{miss}}$ like dead cells, dead material, and wrongly calibrated cells in order not to misidentify these effects as a new physics signature.

4.4 Taus

The tau, as the heaviest lepton, can decay into lighter leptons as well as hadrons. The reconstruction of taus therefore is far more complicated than electron and muon reconstruction. And achieving a high purity (real taus divided by all reconstructed taus) is rather difficult in contrast to lighter leptons. Due to this complexity, it is sometime ignored completely in a clean leptonic analysis, or restricted to only the single charged pion mode.

In the SM, heavy particles exhibit lepton universality in the BR ($i.e.$, BRs are the same for all lepton families). If the physics beyond the SM also has such a universality, then the muon channel is the golden mode of discovery in terms of its high purity and precise p_{T} measurements. Interestingly, in the MSSM, the heaviest slepton (squarks) have heavier masses among sleptons (squark) in higher tanβ parameter space, resulting higher BRs for those heavier particles. Sup-

pose the muon channels are checked first and no excess found beyond the SM. Yet, the physics beyond the SM is lurking in the tau channels if tau BR is significantly enhanced. Therefore, it is worth analyzing taus even given its challenging nature.

About two thirds of tau decays are hadronic, and the other one third is leptonic. As long as the decay is leptonic, it can be reconstructed as lighter leptons. The challenging decays are the hadronic ones. Henceforth, taus refer to hadronic decaying taus. The cross section of the QCD processes are the largest at pp colliders. In the calorimeters, there are not much difference between QCD jets and hadronic tau decays. This poses the first and the biggest challenge to hadronic tau reconstruction.

This section follows reference [45]. The first half of this section is devoted to the reduction of QCD backgrounds, and the latter half describes electron and muon rejection. The algorithm used in this analysis is a cut-based shrinking cone, and assumes taus originating from a heavy particle, like Z, W, and $Higgs$. In other words, a narrow signal cone contains all tau decay products (due to Lorentz boost).

4.4.1 Particle-Flow

The reconstruction uses Particle-Flow (PF) techniques, which has been validated with the early data in 2010. Comparison of data and PFJets are shown in Fig. 24.

The particle-flow algorithm aims at providing a global event description at the level of individually reconstructed particles with a combination of information coming from all the CMS detector components. The reconstructed and identified individual particles are muons, electrons, photons, charged hadrons, and neutral hadrons. The complete list of particles may then be used to derive composite physics objects such as clustering into jets with standard jet algorithms. The algorithms discussed in this analysis use this list of particles both for reconstruction and identification of taus. Specifically, all reconstructed particles in the event including charged pions and photons from any possible hadronic tau decay products are clustered into jets with the AK algorithm.

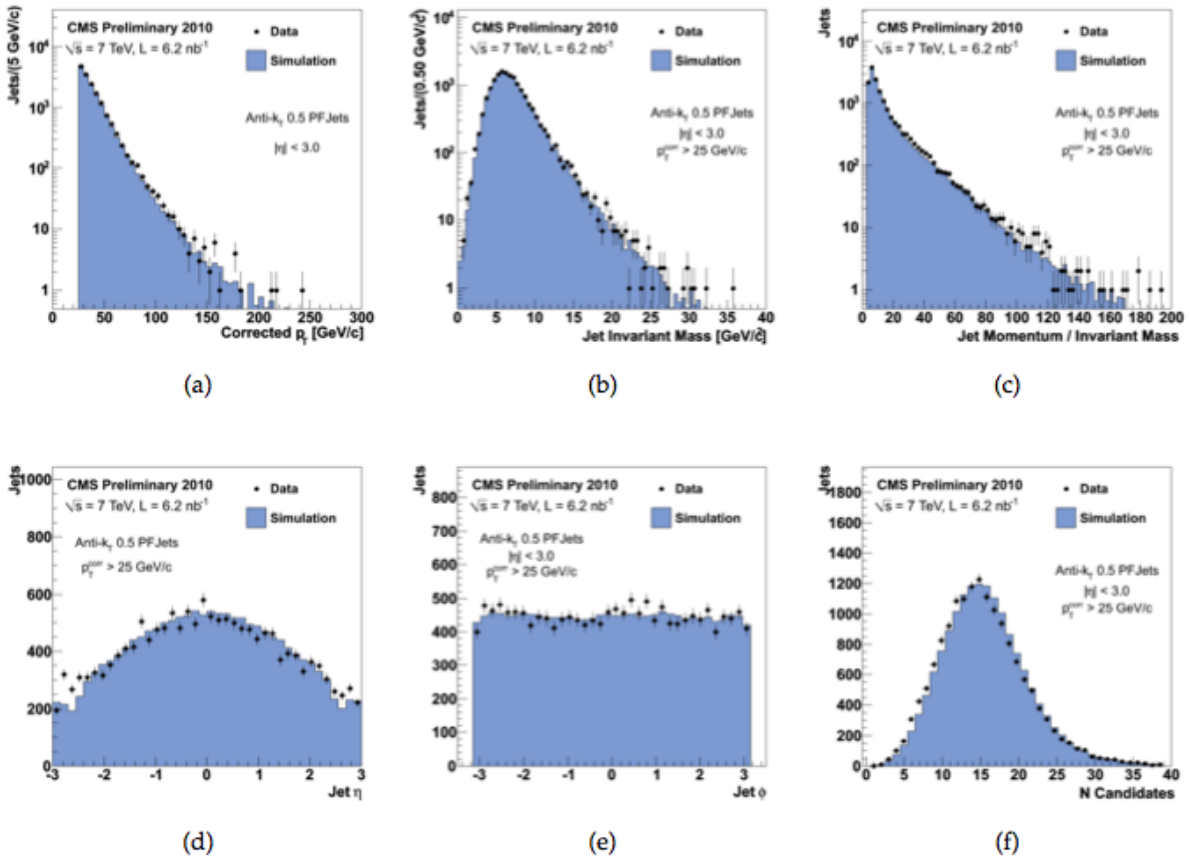

Figure 24: Basic jet properties in dijet events: Distributions of (a) jet transverse momentum; (b) jet invariant mass; (c) the ratio of jet momentum to jet invariant mass; (d) jet pseudorapidity; (e) jet azimuth; and (f) number of particle constituents in a jet [46].

The tau algorithm benefits from both the improved energy and angular resolution available describing each individual particles in the jet. The benefits of using it can be summarized in three points:

- First, better energy and momentum resolution from the inner tracker and ECAL for charged hadrons and neutral pions
- Second, no azimuthal angle bias for charged hadrons because the momenta are determined at the primary vertex where the axial magnetic field has no effect
- Third, not affected by the JES correction tuned for QCD jets

4.4.2 Base Reconstruction

The base tau selection works as following:

- A minimum transverse momentum is required to each jet and only those satisfying it are further considered as a possible tau candidate.
- At least one charged hadron with $p_{\mathrm{T}} > 5$ GeV/c is required to be found within a distance from the jet axis < 0.1 in R.
- A narrow signal cone is defined around the direction of the leading object, and an isolation annulus expected to contain little activity is defined as a cone larger than but excluding the signal cone, as illustrated in Fig. 25.

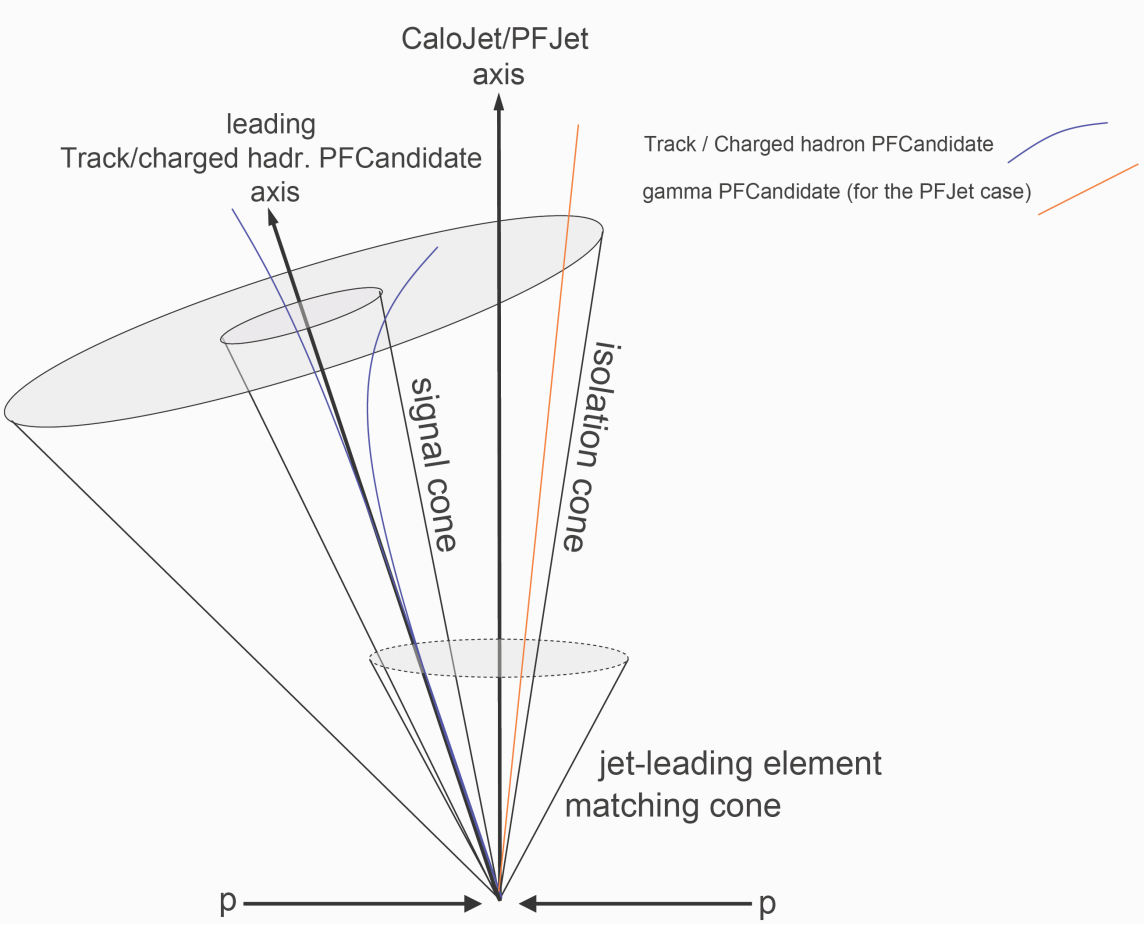

Figure 25: The signal and isolation cones defined by the leading track inside the jet for PFTau reconstruction [45].

Default isolation requires no reconstructed charged hadron with p_{T} above 1 GeV/c and no photon with E_{T} above 1.5 GeV inside the isolation annulus. In this analysis, a shrinking cone algorithm, which defines its signal cone size as $5.0[\mathrm{GeV}]/p_{\mathrm{T}}$, is used.

4.4.3 High Level Reconstruction

The base reconstruction successfully rejects most QCD jets retaining (O(few %)) while keeping about half of the $Z \rightarrow \tau\tau$ signal as an important benchmark. However, it does not reject most electrons and muons, which are the perfect tau candidates as it provides a good track and energy deposits in the calorimeters.

The electron pre-identification algorithm uses a multivariate analysis of the tracker and calorimeter information which provides efficient seeds for full electron reconstruction. The electron pre-identification achieves 90-95% efficiency across the entire tracker acceptance, with about 5% pion efficiency. In order to optimize the electron rejection efficiency beyond 95%, two additional variables are formed.

The first variable E/P is defined as the summed energy of all ECAL clusters in a narrow strip $|\Delta\eta| < 0.04$ with respect to the extrapolated impact point of the leading track on the ECAL surface divided by the momentum of leading track inside the jet. This variable is expected to cluster around unity for electrons and to be scattered around smaller values for charged pions from tau decays.

The second variable, $H_{3\times3}/P$ is defined as the summed energy of all the HCAL clusters within $\Delta R < 0.184$ around the extrapolated impact point of the leading track on the HCAL surface divided by the momentum of the leading track inside the jet. This variable is expected to cluster around zero for electrons and to be somewhat randomly distributed for charged pions from tau decays.

The high efficiency of the standard muon reconstruction and identification in the CMS provides optimal rejection of muons in the reconstruction if the muon information is used. Tau candidates are rejected if their leading track matches to a global muon, or the matched muon has at least one muon chamber segment, as real pions usually are not reconstructed as global muons.

5 Analysis

The aim of this analysis is to search for SUSY in 3 and 4-lepton final states. The multilepton final state is interesting since leptonic signatures are clean at the LHC where most backgrounds are jets, and the chargino and second-lightest neutralino have sizable branching ratios to leptons. The branching ratio of chargino to $\widetilde{l}\bar{\nu}_l$ pair is flavor dependent in high tanβ SUSY parameter space, because one of $\widetilde{\tau}$ gets lighter than the other $\widetilde{\tau}$. For instance LM1 SUSY point, the $\widetilde{\tau}_1\bar{\nu}_\tau$ branching ratio is three times larger than the other $\widetilde{l}\bar{\nu}_l$ ones in $\widetilde{\chi_1}^{\pm}$ decays. Some decay channels are listed in Table 7 for this point.

decay mode	branching ratio
$\widetilde{\chi_1}^{\pm} \rightarrow \widetilde{e}^{\pm}\bar{\nu}_L$	16%
$\widetilde{\chi_1}^{\pm} \rightarrow \widetilde{\tau}_1^{\pm}\bar{\nu}_\tau$	44%
$\widetilde{\chi_2}^{0} \rightarrow \widetilde{e}_R e$	5.6 %
$\widetilde{\chi_2}^{0} \rightarrow \widetilde{\tau}_1 \tau$	49%

Table 7: Branching Ratios for the LM1 SUSY Point. Branching ratios are computed by ISASUSY [47]. The cross section of this particular point is 6.55 pb at NLO for $\sqrt{s} = 7$ TeV with k-factor correction computed by PROSPINO [48].

To bolster the discovery potential for SUSY, it is natural to include the tau channels. The analysis is done by cuts on the kinematic quantities that are reconstructed from the signals recorded by the different detector components. The heart of the analysis is to find an excess of events over that expected from the SM, because such an excess is considered as evidence for physics beyond the SM. The excess can be interpreted differently with various theories. In this analysis, only SUSY models are considered. The p_{T} distribution is shown in Fig. 26 for LM0 signal sample.

With the $35\,\mathrm{pb}^{-1}$ of integrated luminosity of 2010 data taking, no signal is found and thus exclusion limits are set.

The signal cross section must be tiny compared to the total cross section of all SM processes. Otherwise, such new physics would have been discovered already. Finding evidence of new physics is thus a needle in a haystack problem. If the new physics somehow mimics the signatures of major SM background processes, the discovery is impossible from event topology

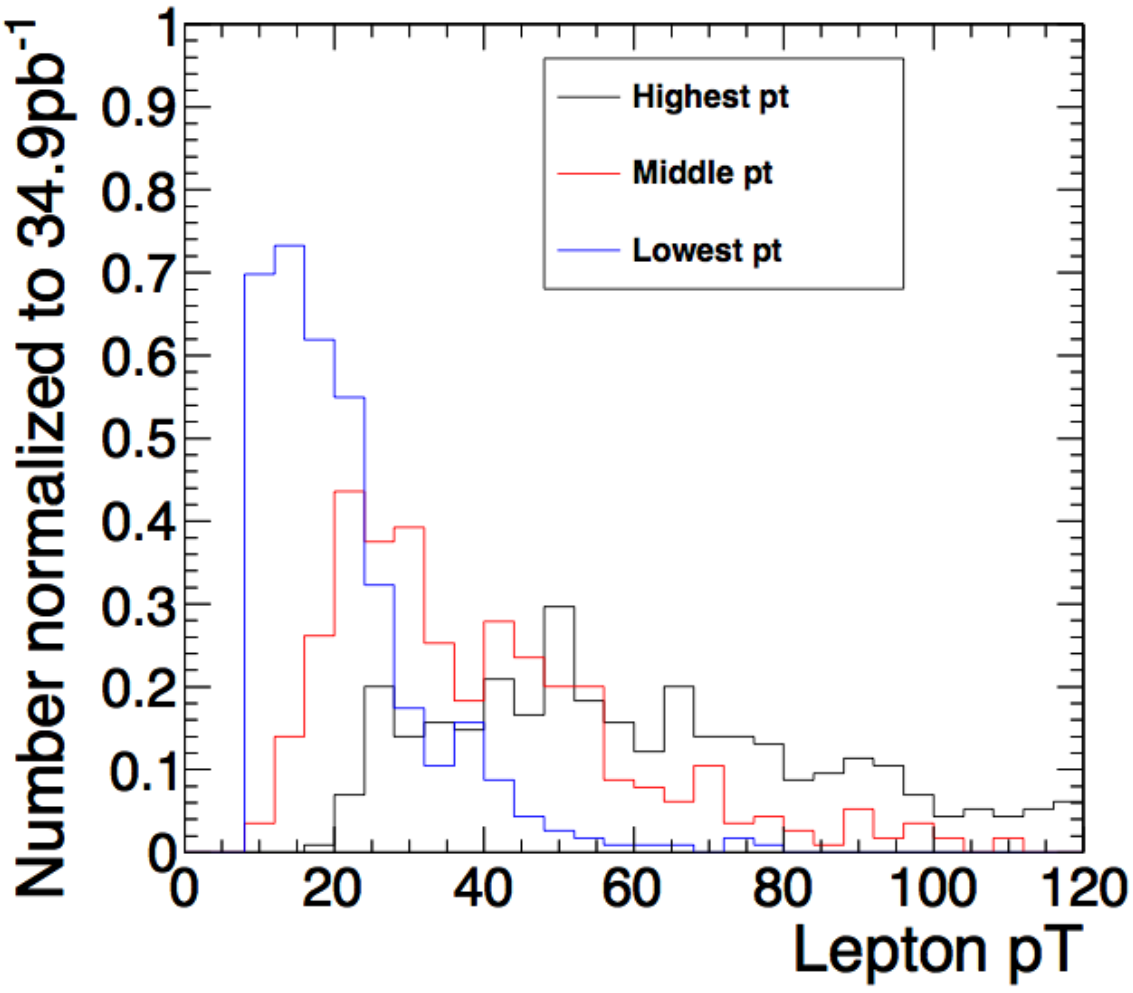

Figure 26: p_{T} spectra for three p_{T}-ordered leptons for LM0 3μ events [49]. The third lepton peaks at 15 GeV.

since those major BGs are discarded. Fortunately, the new processes can generate events with different signatures from those of the SM. By carefully choosing requirements to be fulfilled by events, it is possible to choose a signature which prefers the new physics events. Then one may count the events passing all the cuts, and compare the measured number of events with the number of events expected from the SM which may be taken from MC samples or data driven methods. In this analysis, a conventional cut-based selection is presented.

This analysis requires detailed knowledge of the new physics, the SM, and detector performance. To gain this information, MC simulation of the SM processes and of the detector are carried out. Details about the analysis are discussed in the following section, including MC samples, preselection cuts, statistical methods, and systematics uncertainties. Finally the result is presented at the end of this chapter.

5.1 Event Generation

Detailed Monte Carlo (MC) simulation is needed before the actual data are examined. Both the SUSY signal and SM backgrounds are generated with Pythia [20], which is a popular MC generator that generates particle interactions at tree level and is capable of simulating parton showers. Various parameters can be varied and tuned to match certain conditions: $\sqrt{s}$ can be set to the desired value and a special parametrization of the parton density functions can be selected from various possibilities. For this analysis CTEQ6M [50] is used. Pythia provides the generation of a large variety of processes and more importantly for this analysis offers the implementation of new processes.

Pythia supports the MSSM and provides an interface to other, next-to-leading order software by taking external files in a format, SLHE, which contains the mass spectrum of SUSY particles. SLHE files are produced with SOFTSUSY and SUSY-HIT [51]. Then, the detector simulation software using Geant4 [52] processes the MC samples so that the outputs are similar to actual data. The entire MC event simulation can be done in the CMS integrated SoftWare frameWork (CMSSW).

The SM background samples are centrally produced and distributed. The CMS Data Bookkeeping System (DBS) is a bookkeeping tool offering an easy way to locate available copies of samples from all over the world (mainly at T2 sites). Signal samples are, however, only produced centrally for a few signals. In the case where one searches a new exotic signal, the samples must be generated by users or a working group. For the nominal signal samples used in this analysis all are generated centrally. While our SUSY parameter space scan, the SUSY working group generated the files.

5.1.1 The CMS Software

The event generation itself is done by Pythia alone or a combination of Pythia and supported external event generators. This is done in the CMS SoftWare (CMSSW). To make use of the CMSSW, the format has to be adapted to its specifications. IOMC provides such an interface.

Consequently, the output file is converted to a ROOT [53] file ready to be passed through all the steps of the CMSSM.

First the cmsdriver tool, which automatically generates configuration file from the database, produces a collection of all specified generation steps which are GEN, SIM, and RECO.

The GEN step puts all generated particles into the $GenParticle$ collection and subsequently the detector simulation is performed. This simulates the detector responses for all particle trajectories –just the way a real collision would produce particles traversing through the detectors– resulting in hits and energy deposits. The breakdown of this step is: DIGI, L1, DIGI2RAW, and HLT, where DIGI digitizes simulated hits, L1/HLT performs the L1/HL trigger decision, DIGI2RAW coverts the digitized hits to the RAW format.

The RAW format is equivalent to the data coming from the CMS detector with real collisions. The data format is called SIM and contains all hits and energy deposits. There is a faster version of SIM, Fast Sim, which is faster than Full Sim by a factor of 10, however it is less precise in terms of detector response. In this analysis, Full Sim is used for background and benchmark signal points while Fast Sim is used for SUSY parameter space scan. Finally the reconstruction is performed. This and subsequent steps are identical for simulated and real data.

The methods of reconstruction for the most of interesting particles are described in the reconstruction section. The data format after this step is called RECO and contains high level physics objects ($i.e.$, particle types and 4-vectors). If desired, the process of chain ends here. The users are encouraged to reduce further the amount of data size by converting RECO to Analysis Object Data (AOD) format, which is a CMSSW Data Format designed to be sufficient for a large set of CMS analyses. It is a proper subset of the RECO Data Formats. Or the users may even apply basic cuts on particle properties using the Physics analysis Tool Kit (PAT) to create smaller ntuple files.

5.2 Monte Carlo Samples

The Monte Carlo (MC) samples used for this analysis is from Fall 2010 7 TeV production, re-reconstructed in CMSSW release 38X. For all signal and background processes, the NLO cross sections are used. The k-factors for signal samples are computed with PROSPINO [48]. The GMSM points ML01 and 02 produced by the SUSY group are used as well. FastSim SUSY parameter space scan samples are produced with CMSSW38X series as well.

MC samples are split into signal and SM BGs in separate tables below.

Process	DBS Name	# Events
Benchmark Point		
LM0	/LM0_SUSY_sftsht_7TeV-pythia6/Fall10-START38_V12	219595
LM1	/LM1_SUSY_sftsht_7TeV-pythia6/Fall10-START38_V12	219190
LM2	/LM2_SUSY_sftsht_7TeV-pythia6/Fall10-START38_V12	220000
LM3	/LM3_SUSY_sftsht_7TeV-pythia6/Fall10-START38_V12	220000
LM4	/LM4_SUSY_sftsht_7TeV-pythia6/Fall10-START38_V12	220000
LM5	/LM5_SUSY_sftsht_7TeV-pythia6/Fall10-START38_V12	220000
LM6	/LM6_SUSY_sftsht_7TeV-pythia6/Fall10-START38_V12	220000
LM7	/LM7_SUSY_sftsht_7TeV-pythia6/Fall10-START38_V12	220000
LM8	/LM8_SUSY_sftsht_7TeV-pythia6/Fall10-START38_V12	220000
LM9	/LM9_SUSY_sftsht_7TeV-pythia6/Fall10-START38_V12	220000
LM10	/LM10/Spring10-START3X_V26_S09	203818
LM11	/LM11_SUSY_sftsht_7TeV-pythia6/Fall10-START38_V12	219190
LM12	/LM12_SUSY_sftsht_7TeV-pythia6/Fall10-START38_V12	219595
LM13	/LM13_SUSY_sftsht_7TeV-pythia6/Fall10-START38_V12	219915
ML01	/PhysicsProcess_PYTHIA6_SUSY_GMSM_SC_ML01	200000
ML02	/PhysicsProcess_PYTHIA6_SUSY_GMSM_SC_ML02	200000
SUSY Scan		
tanβ3	/PhysicsProcesses_mSUGRA_tanbeta3Fall10v1/spadhi-PhysicsProcesses_mSUGRA_tanbeta3Fall10-.../USER	13000000
GMSM	/PhysicsProcesses_GGM_SCMSleptonicNLSP/spadhi-PhysicsProcesses_GGM_SCMSleptonicNLSP-.../USER	31350000

Table 8: Datasets used for SUSY signal Monte Carlo studies. Most of SUSY signals are CMSSW38X samples. The only exception is LM10, which is a CMSSW31X sample. The scan samples are made with FastSim.

SM BG Process	DBS Name	# Events
VV+jets	/VVJetsTo4L_TuneD6T_7TeV-madgraph-tauola/Fall10-START38_V12-v1	962976
γV+jets	/PhotonVJets-madgraph/Spring10-START3X_V26_S09-v1	1086319
W+jets	/WJets-madgraph/Spring10-START3X_V26_S09-v1	10068895
$t\bar{t}$ +jets	/TTJets_TuneD6T_7TeV-madgraph-tauola/Fall10-START38_V12-v2	1394548
QCD	/InclusiveMu15/Spring10-START3X_V26_S09-v1	6228142
QCD Pythia8	/QCD_Pt-15_7TeV-pythia8/Spring10-START3X_V26B-v2	5234800
$Z \to \bar{\tau}\tau$	/Ztautau/Spring10-START3X_V26_S09-v1	2195255
$RelVal\, Z \to \bar{\mu}\mu$	/RelValZMM/CMSSW_3_9_2-START39_V3-v1	9696
$RelVal\, Z \to \bar{e}e$	/RelValZEE/CMSSW_3_9_2-START39_V3-v1	9000
DY(low)+jets	/DYJetsToLL_TuneZ2_M-50_7TeV-madgraph-tauola/Fall10-START38_V12-v3	2661949
Z+jets	/DYJetsToLL_TuneD6T_M-10To50_7TeV-madgraph-tauola/Fall10-START38_V12-v2	188145

Table 9: Datasets used for SM BG Monte Carlo studies. Important SM BGs are CMSSW38X, and other ones are CMSSW31X samples. DY(low)+jets and Z+jets sample do not overlap because of the invariant mass cut on SFOS leptons at $M(ll) = 50\text{GeV}/c^2$. DY(low) sample also has a mass cut at $M(ll) = 10\text{GeV}/c^2$ which may be too tight when compared to data because lepton p_{T} cut is 8 GeV/c each and the isolation cone is 0.3 in R. The lowest possible mass in data is about 3 GeV/c^2.

5.3 Data

The results in this analysis are based on the 2010 data taking, which corresponds to 34.9 pb^{-1} collected with the CMS detector. 2010 RunA data is re-reconstructed ones, and 2010 RunB data is promptly reconstructed one. The re-reconstructed one used the updated calibration for the subdetectors at the time of re-reconstruction, and the promptly reconstructed one used the best calibration when the data was taken. For analyses with at least one muon, the datasets used are

- /Mu/Run2010A-Sep17ReReco_v2
- /Mu/Run2010B-PromptReco-v2

For the $3e$ and $ee\tau$ channels, the datasets used are

- /EG/Run2010A-Sep17ReReco_v2
- /Electron/Run2010B-PromptReco-v2

5.4 Preselection

The aim of the preselection is to reduce most of the SM background contributions to the level of the SUSY signal events. In muon channels, this selection reduces background to negligible level compared to LM0 signal for example. Even tau channels have background relevant to LM0 signal after the selection. The quantities which have been cut on are explained in reconstruction sections.

5.4.1 Muons

Muons are selected with a simple set of criteria:

- GlobalMuonPromptTight AND Tracker Muon [54]

- $p_{\mathrm{T}} \geq 8$ GeV/c
- $|\eta| \leq 2.1$
- #Tracker hits ≥ 11
- Global χ^2/d.o.f. < 10.0
- $|d_0| < 0.02cm$
- $(TrackerIso + ECALIso + HCALIso)/p_{\mathrm{T}} < 0.15$

Muons sometimes have a leakage of the own track, as a single track may be reconstructed multiple times. This is the reason of setting the inner cone when muon isolation is computed. Duplicated muons are removed with $|\Delta R| < 0.01$ where ΔR is the quadrature sum of the difference between the η and ϕ of the two muons.

5.4.2 Electrons

The electron selection is similar to the muon selection:

- VBTF90 electron ID cuts ($\sigma_{i\eta i\eta}$, $\delta\phi$, $\delta\eta$, HoE, conversion rejection) [55].
- $p_{\mathrm{T}} \geq 8$ GeV/c
- $|\eta| \leq 2.1$
- $|d_0| < 0.02cm$
- $\Delta R > 0.1$ to nearest μ
- $(TrackerIso + max(0, ECALIso - 1.0\mathrm{GeV}) + HCALIso)/p_{\mathrm{T}} < 0.15$

The conversion rejection code uses #expected hits. The distribution is shown in Fig. 27 for the LM0 signal and γ+V+jets background samples.

The pedestal subtraction of 1.0 GeV is needed only in the barrel region to account for accumulated noise [55].

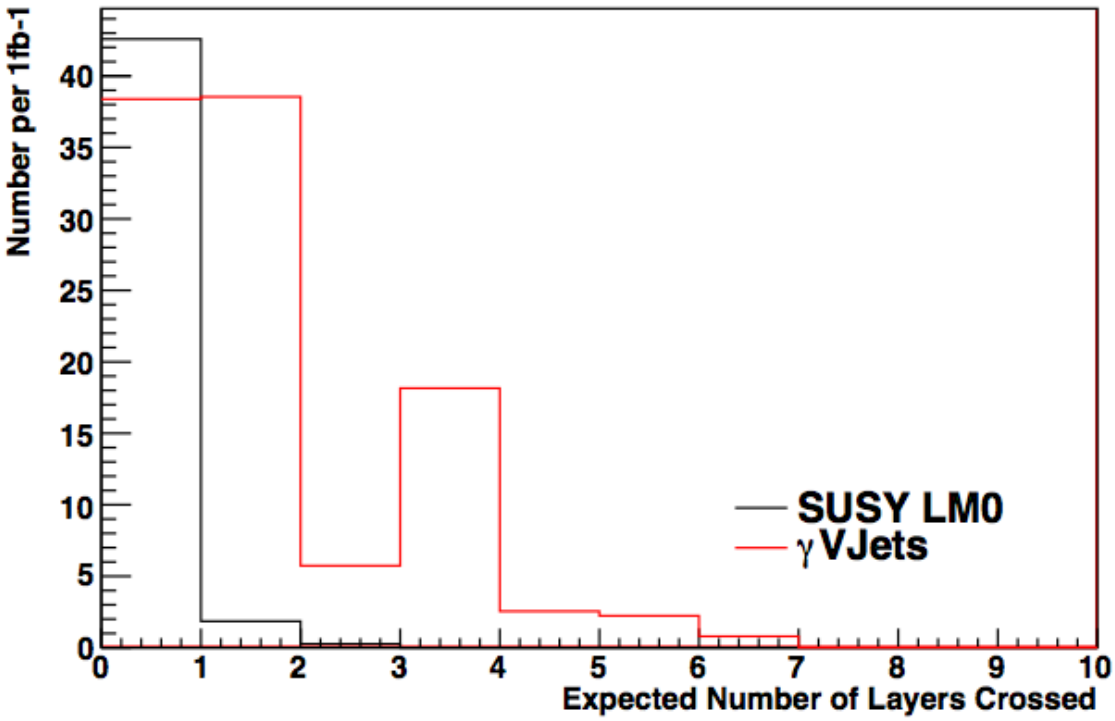

Figure 27: The difference between the first layer crossed by a candidate track and the expected innermost hit for the track for LM0 signal (black) and the γ+V+jets sample (red) which is dominated by photon conversions. All events above the first two bins are removed [49].

Muons with p_{T} less than 100 GeV/c do not radiate much, but energetic ones do. Then, a muon may be reconstructed as both a muon and electron by satisfying both requirements described above. In such cases, the priority is given to the muon over electron in this analysis.

5.4.3 Taus

When 'taus' are discussed, it means taus decaying hadronically. For example, $\tau \rightarrow \nu_{\tau}\bar{\nu}_{\mu}\mu$ is an isolated good muon as long as a tau comes from heavy particle (like Z boson) decay as far as muon identification is concerned. Although electrons and muons from taus must be softer in p_{T} and larger Impact Parameter (IP) on average, given the high reconstruction efficiencies of electrons and muons compared to that of taus, the electrons and muons shall be reconstructed as they are, and those particles should be a part of the signal acceptance.

Tau selection, for hadronic tau decays, is summarized here. Reconstruction of particle-flow taus starts with a PF jet using the calorimeter and tracker information [45] as already reviewed in the reconstruction section. To reduce fakes from QCD jets, three cuts are applied.

- First, a leading charged hadron with $p_T > 5$ GeV$/c$ in a ΔR cone of 0.1 from the direction of the jet is required.
- Once the leading hadron is found, a 'shrinking' signal cone with $\Delta R = 5$ GeV$/E_T^{jet}$ and an isolation cone with $\Delta R = 0.5$ are defined.
- In the annular region between these cones, electromagnetic and tracker isolation requirements are applied.
  - No track with $p_{\mathrm{T}} > 1$ GeV/c
  - No γ with $E_{\mathrm{T}} > 1.5$ GeV

Other requirements are:

- $p_{\mathrm{T}} \geq 8$ GeV/c
- $|\eta| \leq 2.1$
- Leading track $p_{\mathrm{T}} \geq 5$ GeV/c
- Require tau to have 1 or 3 charged tracks inside its signal cone
- $\delta R > 0.15$ to nearest e or μ
- ECAL $E/P_{track}^{lead} \leq 0.8$ OR HCAL $E/P_{track}^{lead} \geq 0.15$
- Discriminator against e, μ

5.4.4 Jets

As emphasized in the theory section, SUSY signal usually originated from heavy gluino and/or squarks, resulting high hadronic activities in the events. Some SM processes, like vector diboson productions, have well isolated multiple leptons but less hadronic activities. Such events could then be the main background to the analysis because it is irreducible as far as isolated

leptons are concerned. To remove most of those events, the scalar sum of energy of jets, H_T, is used. Jets used for H_T calculation is the AK5 jets with Pure09 loose cuts [56] satisfying these conditions:

- $p_{\mathrm{T}} \geq 30$ GeV/c
- $|\eta| \leq 2.5$
- Neutral hadron energy fraction < 0.99
- Neutral EM energy fraction < 0.99
- Charged EM energy fraction < 0.99
- Charged hadron energy fraction > 0
- At least one charged hadron
- At least two jet constituents
- $\delta R > 0.3$ to nearest e, μ, τ

The #jets distribution is shown in Fig. 28.

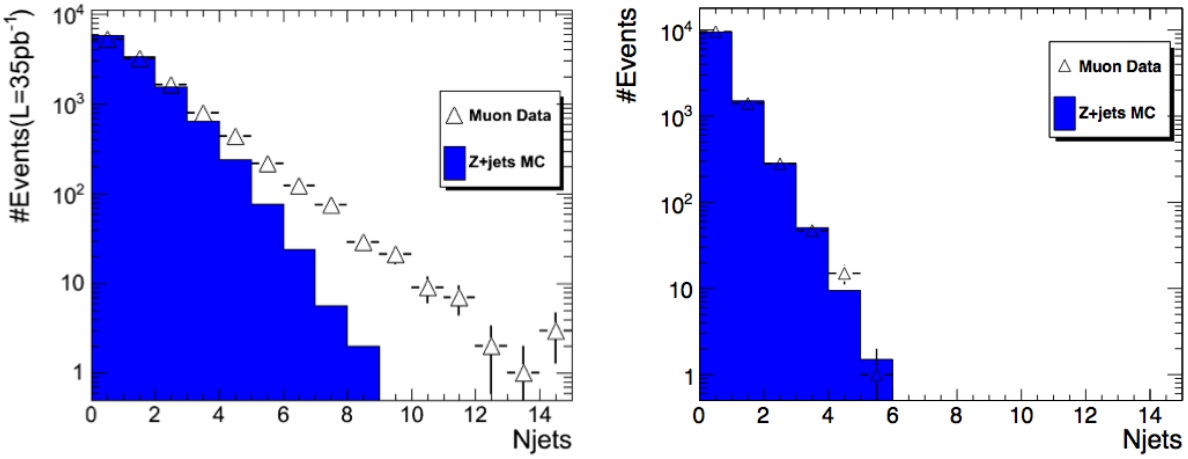

Figure 28: Distribution of the number of PF jets with $E_{\mathrm{T}} > 8$ (left) and $E_{\mathrm{T}} > 30$ GeV (right). The former is relevant for the tau selection and the latter for the H_{T} calculation. H_{T} is less sensitive to the pileup events. However, the taus are sensitive to the number of pileup events. We scale up DY MC expectations based on the number of events in the control region in data.

The selection is motivated by signal event signatures. The signal leptons (electrons and muons) are prompt and well isolated. A minimum transverse momentum requirement reduces the contribution from soft particles, which are mostly from non-prompt particle decays. An isolation requirement insures that the leptons are not from leptonic decays of heavy quarks, where the leptons are surrounded by other hadrons or decay products of hadrons. The "total relative isolation" is defined as the energy of all forms deposited within a cone in (η, ϕ) about the lepton candidate, relative to the momentum of the candidate particle. For muons and electrons the "isolation cone" is defined by $\Delta R \equiv \sqrt{\left(\Delta\eta^2 + \Delta\phi^2\right)} = 0.3$ and for for taus the definition is given in the preselection section. It is worth noting that the tau isolation is not relative but absolute isolation with different isolation regions compared to those of electron and muon.

A cut of $|\eta| < 2.1$ for the leptons is chosen to insure that the isolation cone falls within the good acceptance, $|\eta| < 2.5$, of the inner tracker.

5.5 Event Selection

The event selection that is applied to the data in advance is the L1 and HL trigger selection. Unlike offline cuts, there is no option at users' disposal. The trigger p_{T} and E_{T} measurements are less precise compared to offline ones, hence a trigger cut should be rather loose in order to collect all possibly interesting events so that harder cuts can be imposed after offline reconstruction on more precise quantities. However this is ideal a case. As the instantaneous luminosity increases, the tighter cuts online are inevitable, and then sizable fraction of signal events may fail at trigger level. In any case, the trigger efficiency must be accounted before comparing the data to MC samples.

The goal of the event selection is to achieve an almost background-free environment when combined with the preselection cuts. For all events, electrons and muons must fall within $1cm$ along the beam axis of a primary vertex with $n_{d.o.f.} > 4$, $|z| < 24cm$, and $\rho = \sqrt{x^2 + y^2} < 2cm$, where (x, y, z) is the position of the primary vertex, as all leptons are expected to come from the primary vertex.

The channels are divided based on lepton flavors first ($e.g.$, two muons plus one electron and so forth). Further divisions are made based on the electric charge of the electron and/or muon. If two muons have the same charge, $e.g.$, ++ or $--$, the channel is labeled as Same Sign (SS) mode. Similarly, Opposite Sign (OS) channels are defined.

The trilepton channels have strictly three leptons including a tau. For 4-lepton events, four or more leptons are required in an event. Multilepton channels are constructed from the isolated leptons with no more than two hadronically decaying taus. The motivation of this limit on the number of taus is that its higher fake rate (reconstructed jets as taus divided by all jets) and difficulty of its trigger at low p_{T} region. Whenever there is more than one way to place an event into different channels, the number of muons acts as a selector to ensure no overlap remains among different channels.

The $Z + X$ events can be removed by applying Z mass window cut. However, the dilepton edge can be within the window, depending on how nature chooses SUSY parameters. Instead of applying the cut, high hadronic activity, $H_T > 200$ GeV, is required to reduce QCD and EW backgrounds (H_T may be called J_T in some of references). The H_T distribution is shown in Fig. 29.

The edge of $\widetilde{\chi_2^0}$ three body virtual decay is given by the formula

$$M_{ll'}^{max} = m_{\widetilde{\chi_2^0}} - m_{\widetilde{\chi_1^0}}. \tag{69}$$

The edge of $\widetilde{\chi_2^0}$ two body decay is given by the formula

$$M_{ll'}^{max} = \sqrt{4 \cdot E_l \cdot E_{l'}} = \sqrt{\frac{(m_{\widetilde{l}}^2 - m_{\widetilde{\chi_1^0}}^2) \cdot (m_{\widetilde{\chi_2^0}}^2 - m_{\widetilde{l}}^2)}{m_{\widetilde{l}}^2}}. \tag{70}$$

The H_T cut rejects the events from direct chargino/neutralino productions. However, for early data searches, reasonable sensitivity is limited to the higher cross section squark/gluino processes which typically have high p_{T} multiple jets. The direct production is cleaner and thus it could have higher sensitivity as long as enough data collected. The similar argument can

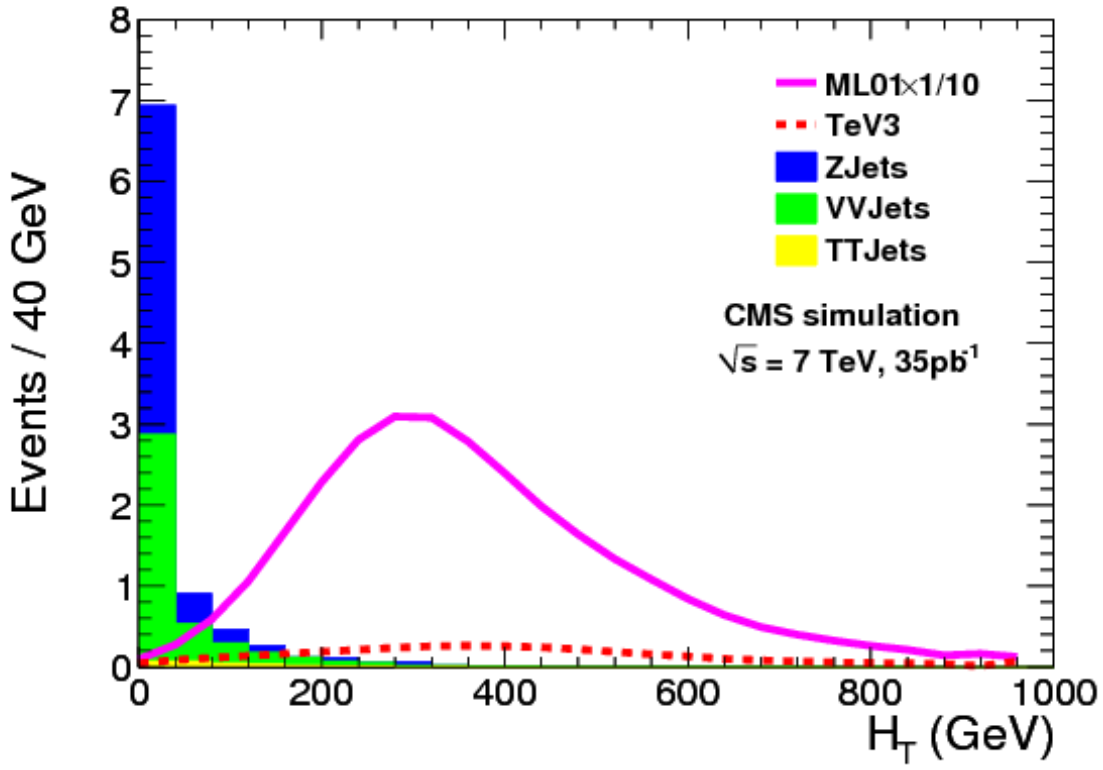

Figure 29: H_T distribution for 3 lepton events passing selection before H_T cut applied [57]. The motivation of H_{T} cut at 200 GeV is clear here to achieve almost BG-free environment.

go to the SS channels, where total background is expected to be smaller than the OS channels but the number of events are smaller there. Since the background for the OS tau channels is larger than other electron and/or muon ones, $E_{\mathrm{T}}^{\mathrm{miss}}$ is required to be at least 50 GeV using the particle-flow(pf) $E_{\mathrm{T}}^{\mathrm{miss}}$. The $E_{\mathrm{T}}^{\mathrm{miss}}$ distribution is shown in Fig. 30.

For all channels, at least one electron or muon with p_{T} greater than 20 GeV/c is required to ensure good trigger acceptance in arbitrary SUSY parameter space, especially for the SUSY scan. The detail of main triggers are described in the trigger section.

5.6 Systematic Uncertainties

Any measurement has an uncertainty associated with it. Quantifying uncertainty is crucial when one interprets the measurement. It could be considered more important than the measurement itself in the sense that an excellent or poor measurement is asserted based on its uncertainty.

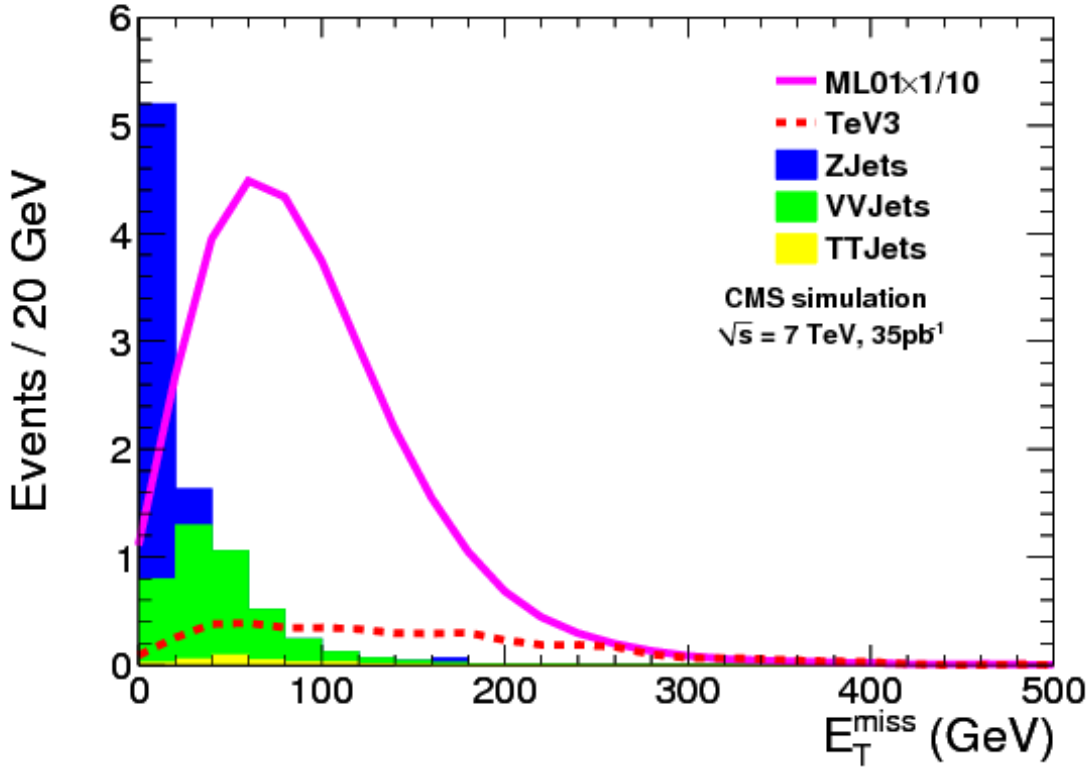

Figure 30: $E_{\mathrm{T}}^{\mathrm{miss}}$ distribution for 3 lepton events passing selection before H_T cut applied [57]. $E_{\mathrm{T}}^{\mathrm{miss}}$ is not as strong discriminator as H_{T}. However, still residual BGs can be removed with $E_{\mathrm{T}}^{\mathrm{miss}}$ cut as $E_{\mathrm{T}}^{\mathrm{miss}}$ is independent from H_{T}.

In this analysis, both signal and background MC samples are generated with realistic detector simulation, and the number of events passing the selection can be counted rather straightforward manner. The question is that with how much confidence can the counted numbers be trusted. This question has two different aspects: first, the uncertainty of the measurement itself, and second, the statistical uncertainty of the measurement. The former one is described here as a systematic uncertainty.

Systematic uncertainties come from different sources, and thus have an impact on all of the samples or just one sample depending on correlations among uncertainties. Systematics uncertainties considered in this analysis are listed in the following subsections.

5.6.1 Identification, Isolation, and Trigger Efficiencies

The relative efficiency can be extracted from data, and the absolute efficiency can be extracted from data and MC comparison. The relative efficiency does not depend on its absolute scale

($i.e.$, the cross sections) because relative quantities are ratios of other quantities. Moreover, the errors are canceled each another. In this section, the Z boson hypothesis is deployed.

- First, a pair of either electron or muon candidates is sought in an event. If no such pair is found, then the event is skipped
- Once the pair is found, then tighter requirements are applied

This method works only when the Z mass peak region is considerably background-free. It could be spoiled by QCD events if the lepton candidates are too loose, given the enormous QCD cross section. As long as the purity is guaranteed within a certain level (typically less than a percent), four regions can be defined: pass-pass, pass-fail, fail-pass, and fail-fail. To ensure higher purity, one can impose tighter conditions on one of lepton legs ($i.e.$, tagging one lepton). This change results losing one of the four regions, fail-fail. The efficiency can then be expressed as

$$\epsilon = \frac{2 \cdot N_{pass\&pass} + N_{pass\&fail} + N_{fail\&pass}}{N_{all\,tagged}}. \tag{71}$$

The tau reconstruction efficiency is the only one estimated by the other technique, template fitting, but not with the tag-and-probe technique.

Electron and Muon ID and Isolation Efficiencies

The lepton identification has a systematic uncertainty of 1% for muons and 1.5% for electrons are estimated in data. The p_{T} dependence of the efficiency is shown in Fig. 31.

The lepton isolation has a systematic uncertainty of 1.5% for both electron and muons. The p_{T} dependence of the efficiency is shown in Fig. 32.

Tau Reconstruction Efficiency

The uncertainty of tau reconstruction is dominated by the fit error from the template fitting technique. The numbers provided by the tau group do not cover the selection used in this

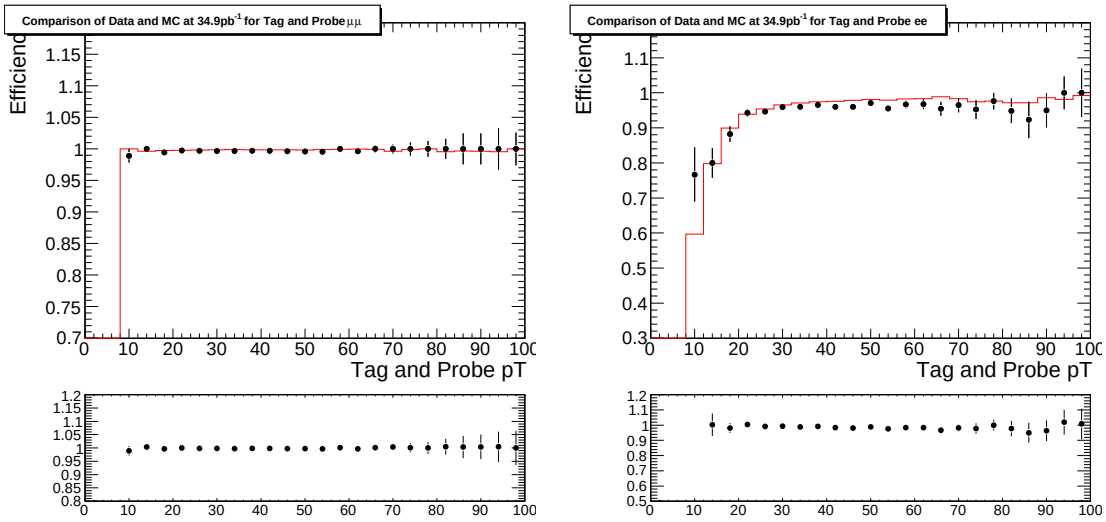

(a) μ ID efficiency (b) e ID efficiency

Figure 31: The particle ID efficiency as a function of p_{T} for muons (left) and electrons (right). Data points are overlaid on the $Z \rightarrow ll$ histogram [49].

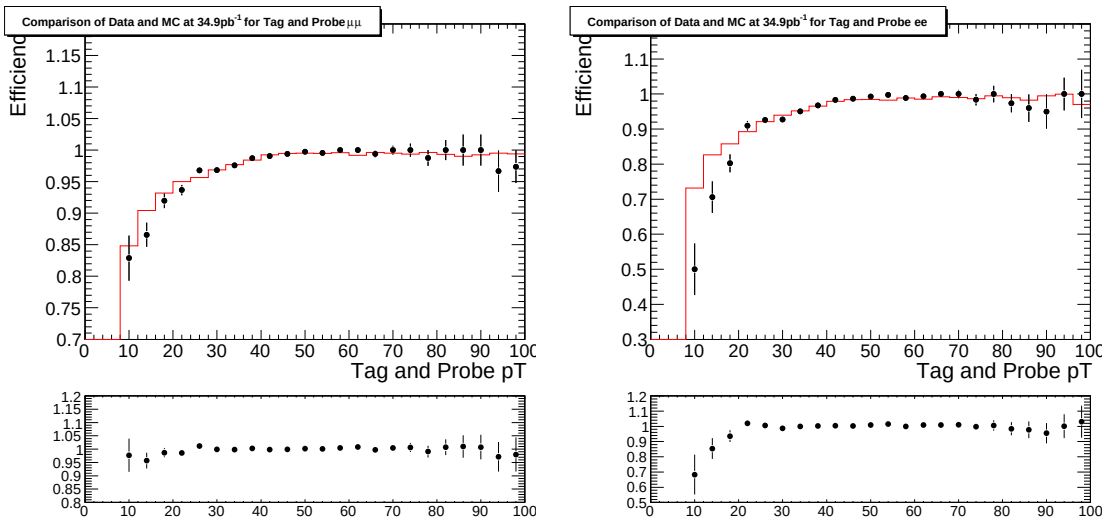

(a) μ isolation efficiency (b) e isolation efficiency

Figure 32: The isolation efficiency as a function of p_{T} for muons (left) and electrons (right). Data points are overlaid on the $Z \rightarrow ll$ histogram [49].

analysis as we want to go lower in tau p_{T}. Here an explicit check is performed although it is expected to be in the same order of magnitude. The template fitting technique, in general, works as follows:

- First, events are preselected, and fitted with MC templates
- Second tighter cuts are applied to preselected events, and fitted again with MC templates

The visible mass of a global muon and tau is fitted with templates prepared beforehand from MC samples, mainly QCD and W+jets events for the background and $Z \rightarrow \tau\tau \rightarrow \tau\mu$ events for the signal. The event selection does not have to be the same as in the main analysis except the tau part. The preselection of muons is almost identical to the one used in the main analysis. The differences for muons are the p_{T} required to be greater than 25 GeV/c, and the relative isolation required to be less than 0.06.

The event selection includes

- transverse mass of the muon and $E_{\mathrm{T}}^{\mathrm{miss}}$ less than 40 GeV$/c^2$
- one pair of a muon and tau candidate where $\Delta\phi(\mu, \tau) > 2.0$
- Z mass window cut between 60 and 120 GeV$/c^2$ for muon pairs if such a pair present in the event to reject Z events

The preselection of taus is the same as the tracking part of the selection used in the main analysis, $i.e.$, leading track with a p_{T} cut on the track. The tracking reconstruction uncertainty is 6% from the tracker group [58]. To remove muon and electron contamination, the discriminators against electrons and muons are applied as well. The uncertainty is estimated as 4% from the tau group by comparing MC and data. The tau p_{T} and η part is the same as in the main analysis.

The template fitting technique works only if there are enough signal events before and after the tighter selection. To increase purity, two additional cuts are applied:

- relative isolation, $\left(\sum p_{\mathrm{T}\,track} + \sum E_{\mathrm{T}\,PF\gamma}\right) / p_{\mathrm{T}\,\tau} < 0.2$

- tau prong cut (require one or three prongs)

This relative isolation is looser than the ECAL and tracker isolation for tau p_{T} of 8 GeV/c or higher. The uncertainty of this additional cut is estimated as the fraction of events which pass the main isolation cuts but fail the relative isolation. It is expected to be small because the relative isolation is looser than the isolation used in main analysis for most of time. The number is 0.8% for $Z \rightarrow \tau\tau$ events.

The uncertainty of the prong cut is estimated using the tracking uncertainty as following. All preselected taus have a leading track with uncertainty of 6%. If there is no additional track, it is a one prong taus, and so the uncertainty is 6%. If it is a three prong tau, then it fails the prong cut, 16% of time assuming each track has 6% reconstruction inefficiency. The larger uncertainty is taken for all taus, although there are more one-prong taus than three-prong taus. Finally, the tighter cuts are applied:

- ECAL and tracker isolation of 1.5 and 1.0 GeV
- HCAL $\sum E_{\mathrm{T}}/p_{\mathrm{T}}{}^{lead}_{track} > 0.15$ OR ECAL Strip $\sum E_{\mathrm{T}}/p_{\mathrm{T}}{}^{lead}_{track} < 0.8$

The muon-tau visible mass after all cuts applied is in Fig. 33, showing the data and a stack of MC samples overlaid.

The relative uncertainty from the template fitting technique is 26.9% computed with the propagation of error formula:

$$\epsilon = \sqrt{\frac{(n_{pass} \cdot \delta_{fail})^2 + (n_{fail} \cdot \delta_{pass})^2}{(n_{pass} + n_{fail})^4}}, \tag{72}$$

where n_{pass} and n_{fail} is the number of events passing and failing the tighter cuts respectively, and δ_{pass} is $\sqrt{n_{pass}}$. The uncertainties are from the fit in pass and fail histograms. By adding all uncertainties mentioned above in quadrature, the total uncertainty becomes $\sim 30\%$, and we use this in our limit setting.

Since taus are much more complicated object than electrons and muons, additional checks are performed. With MC Embedding technique, the effect of the pile-up results about 4% uncer-

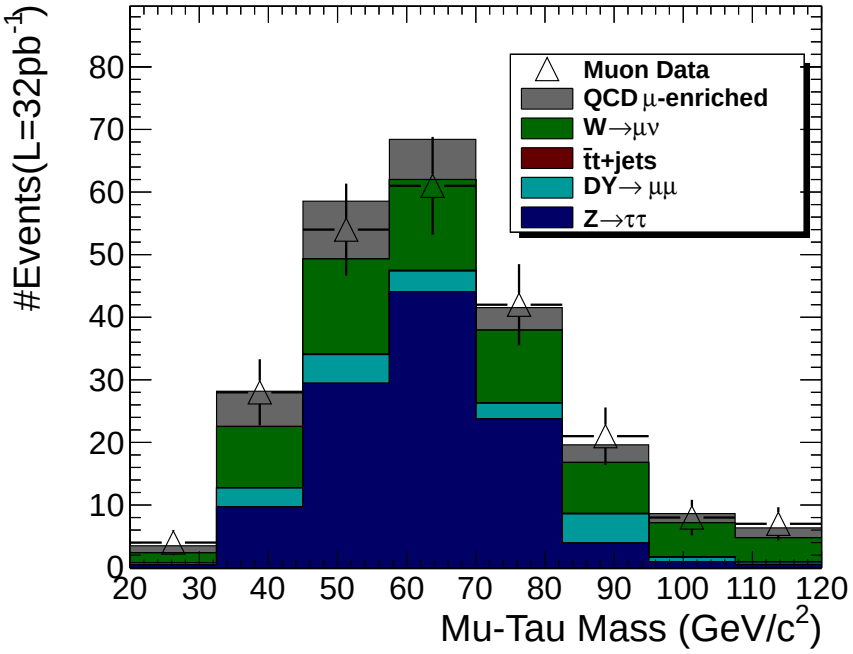

Figure 33: The invariant mass of the muon and tau. The mass between 20 and 120 GeV$/c^2$ is used for the template fitting. Data agrees with MCs within statistical fluctuations.

tainty, and Random Cone study, the effect of ΔR from the nearest jet results 1.3% uncertainty. Both uncertainties are rather small compared to the first one, and virtually no effect. The details are documented in the App. B.

Trigger Efficiencies

In order to analyze the trigger efficiencies, the tag-and-probe method analogous to the lepton isolation and identification analysis has been done requiring: offline leptons to pass the lepton selection described in Sec. 5.4, and the probe lepton is checked whether it passes the trigger under study. The efficiencies for two representative triggers are shown in Table 10 and Fig. 34 as a function of p_{T}.

The trigger is quite different in this analyses compared to other ones, like single lepton plus X. The trigger efficiency can be high just because of multiple leptons with single lepton triggers. Even if a single lepton trigger has a efficiency of 90%, the total inefficiency of trilepton events is 0.01% = $(100\% - 90\%)^3$. This estimate is always valid as long as each lepton leg is independent from other legs. This argument fails when the offline p_{T} cut does not match

Trigger	$Z \to \ell\ell$ MC	Data
HLT_IsoMu13	0.923 ± 0.003	0.874 ± 0.003
HLT_Ele17_SW_TighterEleIdIsol_L1R	0.933 ± 0.004	0.958 ± 0.002

Table 10: The trigger efficiency determined from the tag-and-probe study for electrons and muons from $Z \to ll$ MC, Muon, and Electron data (Run148822-149294). Overall efficiencies are computed for a probe lepton $p_{\mathrm{T}} > 15$ and 20 GeV/c, for muons and electrons respectively, where efficiencies are expected to be constant. The difference between data and MC is more than statistical fluctuations, although these differences are small. The cause of such discrepancies are the calibration used in MC. We assume the numbers obtained from data are right. However, few percent difference does not affect our overall high trigger efficiency.

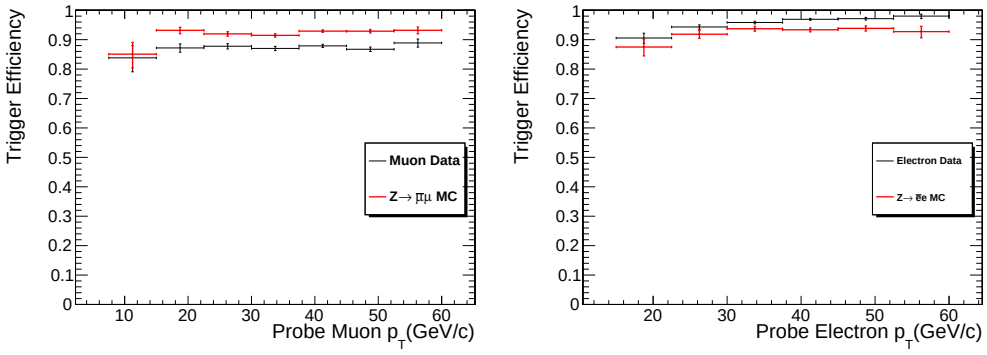

Figure 34: The trigger efficiency as a function of p_{T} for muons (left) and electrons (right). Data points are overlaid on the $Z \to \ell\ell$ MC ones.

up with the online cut. At the trigger turn-on curve, the efficiency is less than 90%. So the efficiency depends on the lepton p_{T} spectrum. And thus the efficiency varies from sample to sample. Most signal samples have an order of a percent uncertainty, just from the single lepton triggers. Since there are cross triggers and the trigger thresholds were lower at the beginning of 2010 run, the estimated uncertainties are overestimated. Also to be conservative, a 5% trigger uncertainty is assigned for SUSY parameter space where lepton p_{T} spectrum can be softer. The 5% uncertainty roughly corresponds to electron/muon single trigger inefficiency. However, the effect is rather negligible compared to other ones like the luminosity, which is described in the next subsection.

All channels considered in this dissertation contain at least two e/μ. Therefore, the trigger efficiency of taus is not explicitly checked, by relying on the high leptonic trigger efficiencies.

Triggers The trigger menu changed over the course of the 2010 run. For simplicity, a list of the useful triggers for our analysis from the 2E32 trigger menu can be found here. There were similar triggers with looser thresholds in earlier runs.

- Muon:
  - HLT_IsoMu13_v3
  - HLT_Mu15_v1
  - HLT_DoubleMu3_v2
  - HLT_Mu5_HT70U_v3
  - HLT_Mu3_Ele8_HT70U_v1
  - HLT_IsoMu9_PFTau15_v1
- Electron:
  - HLT_Ele17_SW_TighterEleIdIsol_L1R_v2
  - HLT_DoubleEle17_SW_L1R_v1
  - HLT_Ele10_SW_HT70U_L1R_v1
  - HLT_DoubleEle8_SW_HT70U_LR1_v1
  - HLT_IsoEle12_PFTau15_v1

Signal Efficiency

The SUSY signal efficiency is estimated from MC samples with corrections from the data. For the particle ID efficiency, the tag-and-probe analysis is carried out as already mentioned. The muon efficiency is near 100% and data and MC agree well. For electrons, the efficiency is somewhat smaller but data and MC still agree reasonably well and small residual background can make the data efficiency appear smaller than MC. The uncertainty on the tau efficiency is estimated from the template fitting method $\sim 30\%$.

For isolation efficiency, the agreement between data and MC is good for muons and electrons except for the lowest five p_{T} bins. The MC samples are corrected by the ratio of data and MC for these bins.

The trigger efficiency is assumed to be high in all channels, especially in the earlier runs. The problem arises only in the latter runs where the online cut is tighter than the offline for second or third electron or muon in descending p_{T} order. The highest p_{T} electron or muon is always required to be stiffer than the online cut. The ML01 signal has a moderate lepton p_{T} spectrum, corresponding only $\sim$5% of leptons being between the offline and online cuts. Thus the probability that both electrons or muons would be missed because they lie in this range is negligible. To be conservative, a 5% trigger uncertainty is assigned to all channels.

5.6.2 Luminosity

As described in the instantaneous luminosity section, there are different ways to determine the luminosity. The luminosity uncertainty of 11% is used according to the luminosity group [59]. As the number of expected events is $N_{evt} = \sigma \cdot L$ for every sample, the uncertainty is fully correlated for all samples.

5.6.3 Cross section

The cross sections of various processes can be predicted from calculation as well as measured from data. In this analysis, all processes have computed cross sections up to NNLO at most. The uncertainty is summarized in Table 11.

process	source	order	cross section [pb]	condition
$W \to l\nu$	FEWZ	NNLO	31314 $\pm$1558	n/a
$Z/\gamma* \to ll$	FEWZ	NNLO	4998 $\pm$272	m(ll) $>$ 20 GeV
$t\bar{t} + jets$	NNLL re-summation	NNLL	165 $\pm$10	inclusive
WZ	MCFM	NLO	18.2 $\pm$0.7	m(ll) $>$ 40 GeV

Table 11: Cross section and uncertainties for major backgrounds. FEWZ is described in [60]. MCFM is described in [61]. The Next-to-Next-to-Leading-Logarithm (NNLL) re-summation is described in [62]. The largest uncertainty is 9.1% of DY process. Other uncertainties are $\sim$ 5 %.

An estimate of the uncertainty is usually performed by varying the renormalization scale and the factorization scale within reasonable range ($e.g.$, factor of two) and monitoring the change in the cross section. The largest deviation is taken as the scale uncertainty. Parameters of the parton density functions that model the incoming partons, are varied to estimate the PDF uncertainty. Both estimates are added in quadrature and the result is interpreted as the cross section uncertainty. The values are less than 10% and implemented as uncorrelated for all samples.

5.6.4 Jet Energy Scale

The Jet Energy Scale (JES) uncertainty affects both the H_T linearly and $E_{\mathrm{T}}^{\mathrm{miss}}$ with a square-root dependence. This effect is determined explicitly by varying the H_T cut by $\pm 10\%$. The largest effect on the LM0 signal for non-tau channels is $^{+4.7}_{-3.8}\%$. The largest effect for the OS tau channels for LM0 is $^{+5.9}_{-7.6}\%$.

For channels without taus, the largest effect on the $t\bar{t}$ +jets acceptance is $^{+26}_{-11}\%$. For the OS tau channels, both the H_T and $E_{\mathrm{T}}^{\mathrm{miss}}$ are varied separately by $\pm 10\%$. The largest variation in $t\bar{t}$ +jets acceptance is $^{+26}_{-23}\%$. The estimated numbers are conservative in two aspects: the expected JES uncertainty is almost flat in jet p_{T} from 30 to 2 TeV, varying from 3-6% in data [43], and $E_{\mathrm{T}}^{\mathrm{miss}}$ is not affected as much as H_T while both quantities are varied by the same relative amount by ignoring the apparent correlation between the two.

5.6.5 Monte Carlo Sample Statistics

Statistical fluctuations are always expected when events are counted, since in the generation of Monte Carlo (MC) samples and detector simulation, the probabilistic nature of particle interactions is modeled using a random number generator. With a given integrated luminosity the number of expected events for a given process with cross section σ is $N_{exp} = \sigma \cdot L$. For every process a certain number of events is generated, resulting in a weight w with $w = \frac{L\sigma}{N_{sim}}$ which is applied to every generated event. However not all events make it into the final selection, hence only $N_{exp}^{cut} = w \cdot N_{sim}^{cut}$ events are expected to pass the selection. The uncertainty is then

calculated by assuming Poisson statistics (roughly speaking, $\sqrt{N_{event}}$). The random error on the number of expected events passing the selection is

$$\sigma_{N_{exp}^{cut}} = w \cdot \sqrt{N_{sim}^{cut}}. \tag{73}$$

The statistical uncertainties for the signal MC samples are negligible ($\sim$1%) for ML01 and ML02 but are closer to 10% for the mSUGRA points.

Total Systematic Uncertainty

The total multiplicative systematic uncertainty for the signal efficiency is dominated by the luminosity uncertainty for electron and muon channels. It varies from 15% to 17% for the GMSM samples while for the mSUGRA LM points, the uncertainty is 18-20% due to the larger MC efficiency uncertainty. Tau channels have higher uncertainty of 30% and 42% for one tau and two taus channels respectively.

The total systematic uncertainty for backgrounds is dominated by the effect of the JES, $\sim$ 30%, for electron and muon channels. The tau channels have a higher uncertainty, $\sim$ 40 %, with additional contribution from the tau fake rate analysis. Although the uncertainty on the background seems non-negligible, the effect on the limit setting is rather small, because the total background events itself is small ($i.e.$, varying a tiny number has almost no effect where appreciable signal is expected).

5.7 Cut-Based Selection Result

The results with the selection described in Sec. 5.4, with 34.9 pb^{-1} data, is presented here. The number of events expected for a few of the SUSY signals and the dominant backgrounds for OS and SS samples derived from the MC samples, App. 5.2, is summarized in Table 12. The 4-lepton channels are summarized in Table 13.

The total background for each mode except the OS tau channels is below 0.2 events and the

total for all four such channels is less than half an event. The tau channels have an expected background of less than a half event in each one. The total BG for OS tau channels is less than one event. The background for the 4-lepton channels is negligible.

Three events are observed in data, and these events are consistent with the SM backgrounds. The details of these events are listed in the App. F in the event display.

Sample	3 μ	$e\mu^+\mu^-$	μe^+e^-	3e	$\tau\mu^+\mu^-$	τe^+e^-	$e\mu\tau$	$e\mu^-\mu^-$	μe^-e^-	$\tau\mu^-\mu^-$	τe^-e^-	$e^-\mu^-\tau$
LM0	0.91(9)	0.72(08)	0.65(8)	0.33(6)	0.88(9)	0.41(6)	0.60(7)	0.29(5)	0.20(4)	0.15(4)	0.09(2)	0.39(6)
LM1	0.20(2)	0.17(1)	0.13(1)	0.07(1)	0.24(2)	0.15(1)	0.10(1)	0.02(0)	0.01(0)	0.04(1)	0.02(0)	0.06(1)
ML01	74.3(8)	89.0(9)	46.5(6)	52.5(7)	41.4(6)	26.6(5)	6.0(2)	1.3(1)	1.5(1)	3.2(1)	3.7(2)	6.3(2)
ML02	10.6(1)	13.1(1)	7.4(1)	8.1(1)	6.4(1)	4.3(1)	1.4(1)	0.8(1)	0.8(1)	0.6(1)	0.7(1)	1.5(1)
DY+jets	0.00(8)	0.00(8)	0.00(8)	0.12(8)	026(16)	0.00(8)	0.07(8)	0.00(8)	0.00(8)	0.00(8)	0.00(8)	0.00(8)
VV+jets	0.05(1)	0.04(1)	0.04(1)	0.01(1)	0.01(1)	0.01(1)	0.00(1)	0.00(1)	0.00(1)	0.00(1)	0.00(1)	0.00(1)
$t\bar{t}$ +jets	0.01(1)	0.01(1)	0.01(1)	0.01(1)	0.17(3)	0.13(2)	0.34(4)	0.00(1)	0.00(1)	0.00(1)	0.01(1)	0.02(1)
Tot BG	0.06(8)	0.05(8)	0.05(8)	0.15(8)	0.44(16)	0.14(6)	0.42(9)	0.00(8)	0.00(8)	0.00(8)	0.01(8)	0.02(8)
Data	0	1	0	0	0	1	0	0	0	0	0	1*

Table 12: Number of events per 34.9 pb^{-1} at 7 TeV for selected SUSY signals and the three significant background channels for OS trilepton channels (first 7 columns) and SS channels. When giving the lepton charges for the SS samples, the other charge$= +2$ combination is implied. The number in parentheses is the uncertainty from MC in the last digit. The results for the total MC and 34.9 pb^{-1} data sample are given, after the H_T cut (in the case of the OS tau channels, $E_{\mathrm{T}}^{\mathrm{miss}}$ cut is also applied). *One event passed all selection in SS e$\mu\tau$ channel and $|\Sigma Q = 3|$.

Sample	4μ	$e3\mu$	$2e2\mu$	$3e\mu$	$4e$	$3\mu\tau$	$e\mu\mu\tau$	$ee\mu\tau$	$3e\tau$	$2\mu2\tau$	$e\mu2\tau$	$2e2\tau$
LM0	0.02(1)	0.08(3)	0.05(2)	0.03(2)	0.01(1)	0.05(2)	0.02(2)	0.04(2)	0.02(2)	0.01(1)	0.04(2)	0.02(1)
LM1	0.01(1)	0.01(1)	0.02(1)	0.00(1)	0.00(1)	0.02(1)	0.01(1)	0.01(1)	0.02(1)	0.01(1)	0.04(2)	0.02(1)
ML01	52.8(7)	5.3(2)	66.5(7)	3.3(2)	21.3(4)	9.7(3)	10.8(3)	6.6(2)	6.1(2)	9.2(3)	1.3(1)	6.3(2)
ML02	10.8(1)	4.7(1)	14.0(1)	2.7(1)	4.7(1)	2.6(1)	2.9(1)	1.9(1)	1.7(1)	1.9(1)	0.5(1)	1.3(1)
DY+jets	0.00(8)	0.00(8)	0.00(8)	0.00(8)	0.00(8)	0.00(8)	0.00(8)	0.00(8)	0.00(8)	0.00(8)	0.00(8)	0.00(8)
VV+jets	0.00(1)	0.00(1)	0.00(1)	0.00(1)	0.00(1)	0.00(1)	0.00(1)	0.00(1)	0.00(1)	0.00(1)	0.00(1)	0.00(1)
$t\bar{t}$ +jets	0.00(1)	0.00(1)	0.00(1)	0.00(1)	0.00(1)	0.00(1)	0.00(1)	0.00(1)	0.00(1)	0.00(1)	0.00(1)	0.00(1)
Tot BG	0.00(8)	0.00(8)	0.00(8)	0.00(8)	0.00(8)	0.00(8)	0.00(8)	0.00(8)	0.00(8)	0.00(8)	0.00(8)	0.00(8)
Data	0	0	0	0	0	0	0	0	0	0	0	0

Table 13: Number of events per 34.9 pb^{-1} at 7 TeV for selected SUSY signals and the background channels for 4-lepton channels. Since there is no background, we do not split into SS and OS but the signal would be primarily in OS. The number in parentheses is the uncertainty from MC in the last digit. The results for the total MC and 34.9 pb^{-1} data sample are given, after the H_T cut.

The background estimates in Table 12 and Table 13 for the analysis without the H_T cut are dominated by Z+jets background. Since the H_T cut clearly removes all of this background, the fact that MC underestimates this background is not important. However, the MC number is scaled up based on #Z events in data. The two main backgrounds after the H_T cut are $t\bar{t}$ +jets (mostly for the OS tau channels) and VV+jets (WZ and ZZ events). For the latter case, fakes are not relevant since WZ and ZZ events can have 3 or 4 leptons in their decays. Thus we expect that the MC prediction for these backgrounds to be reliable and we do not scale up the background predictions.

5.8 Statistical Interpretation

Once measurements are performed, one may wish to claim a discovery of a new particle, symmetry, or exclusion of certain parameter space in a specific model. To do so, a statistical test is carried out. It is intended to quantify how likely the result is in terms of statistical fluctuations, although such a test itself may have certain assumptions built in it. In statistics, this is a hypothesis test. The simplest case is one experiment with a pass or fail outcome.

Suppose one black ball is in a bag, and there are more than one ball in the bag. One may assume that there are only black balls in the bag. This is a null hypothesis, no new contribution besides 'assumed' one. One may imagine there could be a white ball as well. That is an alternative hypothesis, known contribution plus a new one. This kind of hypothesis test is very specific to, and thus dependent on, the null and alternative hypothesis. In this analysis, the null hypothesis is the SM contributions only, and the alternative hypothesis is the sum of the SM and SUSY contributions. To perform the statistical test, a quantity that distinguishes between the two hypotheses, has to be defined. This test statistics can be freely chosen but it makes sense to choose the variable which best separates the two hypotheses and minimizes the possible mistakes. There are two types of mistakes in this context: the error of the first kind, representing the probability to falsely discover an absent signal, and the error of the second kind, stating the probability of excluding a signal albeit its presence. These two possibilities define the significance of which the hypothesis to be rejected at a certain Confidence Level

(CL, or Confidence Interval(CI)).

In order to claim a discovery, the error of the first kind is required to be smaller than $2.85 \cdot 10^{-7}$, motivated by the probability of Gaussian one-sided 5 σ deviation. This is rather arbitrary as there is no reason to believe the assumed hypothesis behaves like Gaussian and thus the interpretation of the 5 σ deviation. It should be considered as convention upon which everyone has agreed. In the absence of a signal, the error of the second kind by convention has to be smaller than 5% motivated by a Gaussian two-sided 2σ deviation. Hence an exclusion usually requires less data than a discovery. A significance can be expressed in terms of probability but it can be expressed as a Gaussian standard deviation as well. In this analysis, Bayesian statistics are used for the limit setting reviewed below. Basic facts about the statistical test and Bayesian statistics can be found for example in [63, 64, 65].

5.8.1 Bayesian Statistics

Let us start with a random experiment with a sample space and probability measure P. In the basic statistical model, we have an observable random variable X taking values in a set S. In general X can be multidimensional. For example, if the experiment consists of n different channels from a population, then $X = (x_1, x_2, ..., x_n)$ where x_i is the vector of measurements in i-th channel.

Suppose that the distribution of X depends on a parameter a taking values in parameter space A. Usually, a is a vector of real parameters, so that A is a subset of R^k for some k and $a = (a_1, a_2, ..., a_k)$. In Bayesian statistics, the unknown parameter a is always treated as a random variable. Then the conditional density of the data vector X given a is denoted $f(X|a)$. The parameter a is given a prior distribution with density h. The joint density of the data vector and the parameter is $f(X|a)h(a)$, for X in S and a in A. The unconditional density of X is the function $g(X)$ obtained by integrating in the continuous case or summing in the discrete case, the joint density over a in A.

The posterior density of a given X is by Bayes' theorem

$$h(a|X) = \frac{f(X|a)h(a)}{g(X)} \tag{74}$$

for X in S and a in A. Finally $A(X)$ is the confidence interval that is a subset of the parameter space that depends on the data variable X but no unknown parameter.

The Bayesian interpretation of probability is subjective opposed to the Frequentist one (which asserts a hypothesis either true or false). One interprets the probability associated with a hypothesis as a measure of degree of belief $i.e.$, assuming some kind of truth, and measuring how close experimental results are to that truth. It includes relative a frequency interpretation – one measures a given outcome a certain fraction of the time.

A probability for an unknown constant is not meaningful with the frequency interpretation, since if we repeat an experiment depending on a whose exact value is unknown, then its value is either never or always in a given fixed interval. The corresponding probability is Boolean but we do not know the true value. With subjective probability, a probability of $1 - r$, that the value is contained in a given interval, reflects the state of an observer's knowledge.

Flat Prior

Let us consider a random variable X assumed to be distributed according to some p.d.f $h(a)$, which depends on an unknown parameter a. The likelihood function is the joint p.d.f for the data X for a given value a and thus can be written

$$L(X|a) = h_{joint}(X|a) = \Sigma f_i(x_i|a)h_i(a). \tag{75}$$

In Bayesian statistics, all of our knowledge about a is contained in the posterior density $h(a|X)$. To find $h(a|X)$, an estimator is often taken to be the value of a where $h(a|X)$ takes maximum value. If the prior p.d.f. $h_i(a)$ is taken to be a constant, then $h(a|X)$ is proportional to the likelihood function $L(X|a)$. In this special case, the Maximum Likelihood estimator coincides

with Bayesian estimator based on uniform a prior p.d.f.. An uniform p.d.f. means that all values of a are equally likely. In this analysis, a flat prior is assumed for the limit setting.

5.8.2 Cross section Limits

Given the agreement with SM expectations, exclusion limits using the counted events in all channels are calculated for 34.9 pb^{-1}. If no signal discovered, a limit is set at 95% CL states that a realization of the SUSY at this parameter space point can be excluded at least at 95% CL as discussed in the statistical interpretation section. The Bayesian Calculator of ROOSTAT package (now integrated with ROOT [53]) derives the confidence interval for data according to the different points in signal parameter space and the SM backgrounds. The prior p.d.f. is assumed flat, and the constraints on the integrated luminosity uncertainty, background, and signal efficiencies are Gaussian. The model itself is a counting model ($i.e.$, Poisson distribution assumed for number of counted events):

$$f(k,\lambda) = \frac{\lambda^k \cdot e^{-\lambda}}{k!} \quad (76)$$

$$N_i = \epsilon_{lumi} \cdot (N_{sig,i} \cdot \epsilon_{sig,i} + N_{bkg,i} \cdot \epsilon_{bkg,i}), \quad (77)$$

where k = N_i, ϵ_x = the efficiency of variable x, and λ = $N_{expected}$ = $N_{sig+bkg}$ = N_i for i-th channel.

For the data accumulated in 2011, one each of $e\mu\mu$, $e\mu\tau$, and $ee\tau$ events are found to be passing all cuts. When the e and μ channels combined, the expected number of events from MC samples is about 0.3, and similarly the combined tau channels, about 1.0 event. The data thus fluctuates upward assuming no signal is present. 95% CL cross section upper limits σ_{95} is calculated for the mSUGRA and GMSB models.

Exclusion limits are plotted in m_0-$m_{1/2}$ plane and chargino masses for the mSUGRA model, and $m_{\tilde{g}}$-$m_{\tilde{\chi}^{\pm}}$ plane for the GMSB model in Fig. 35, 37, and 36, respectively. $tan\beta = 3$, $A_0 = 0$, and $\mu > 0$ are assumed for all of the plots. The exclusion is equivalent to the Tevatron result which are based on O(100) times more data collected. The valley region in Fig. 35 is due

to two-body decay of $\widetilde{\chi_2^0}$ with one of leptons with p_{T} less than the offline cut. Fig. 36 shows comparison of the LEP, Tevatron, and CMS results at $m_0 = 60$ GeV. A large area of parameter space is excluded as shown in Fig. 37 for co-NLSP scenario.

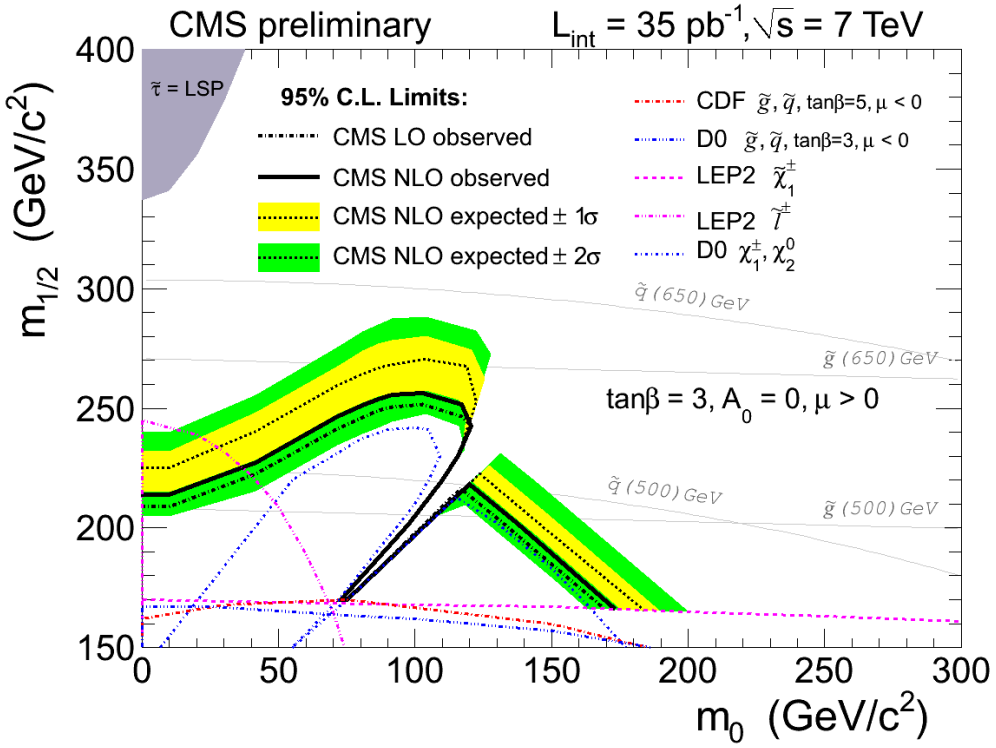

Figure 35: The scan for mSUGRA parameter space for tanβ = 3. The LEP and Tevatron exclusion limits (red, blue, and pink dashed lines) are shown together for comparison [57]. LO and NLO observed limits are drawn with black solid and dashed lines. One and two σ bands are drawn with yellow and light green shaded areas.

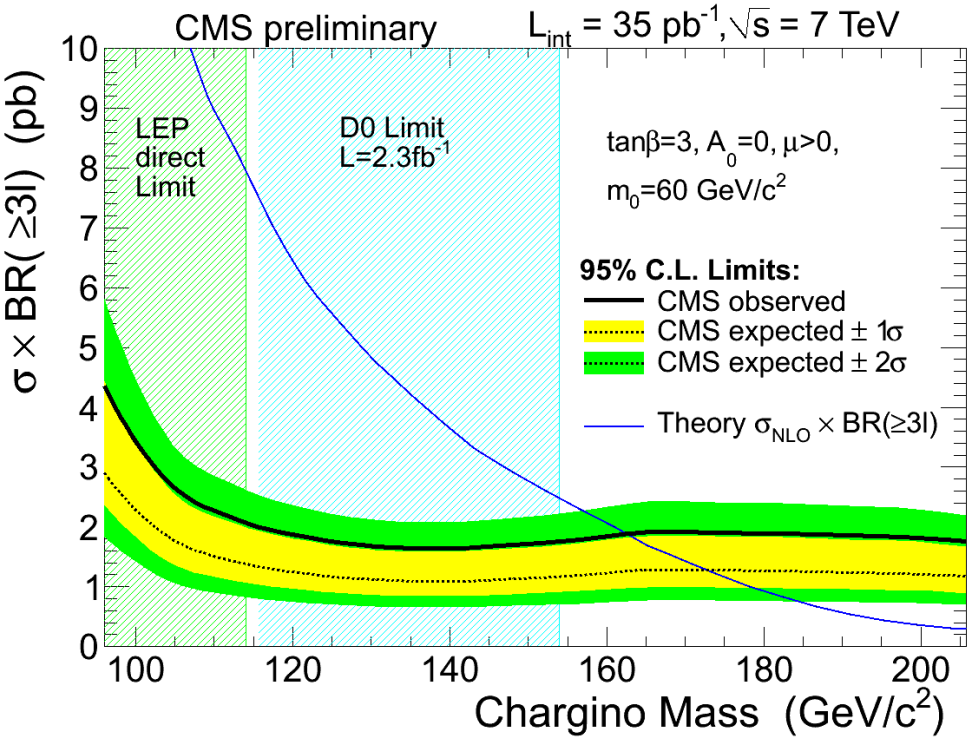

Figure 36: Expected cross section times branching ratio $\sigma \times$ BR($3l$) as function of the chargino mass. The theoretical curve crosses the observed 95% upper limit on the cross section at 163 GeV$/c^2$, thus excluding charginos below this mass for these values of the other parameters. For comparison the excluded regions by LEP (from slepton limits) and Tevatron (from chargino-neutralino production) have been indicated as well [57].

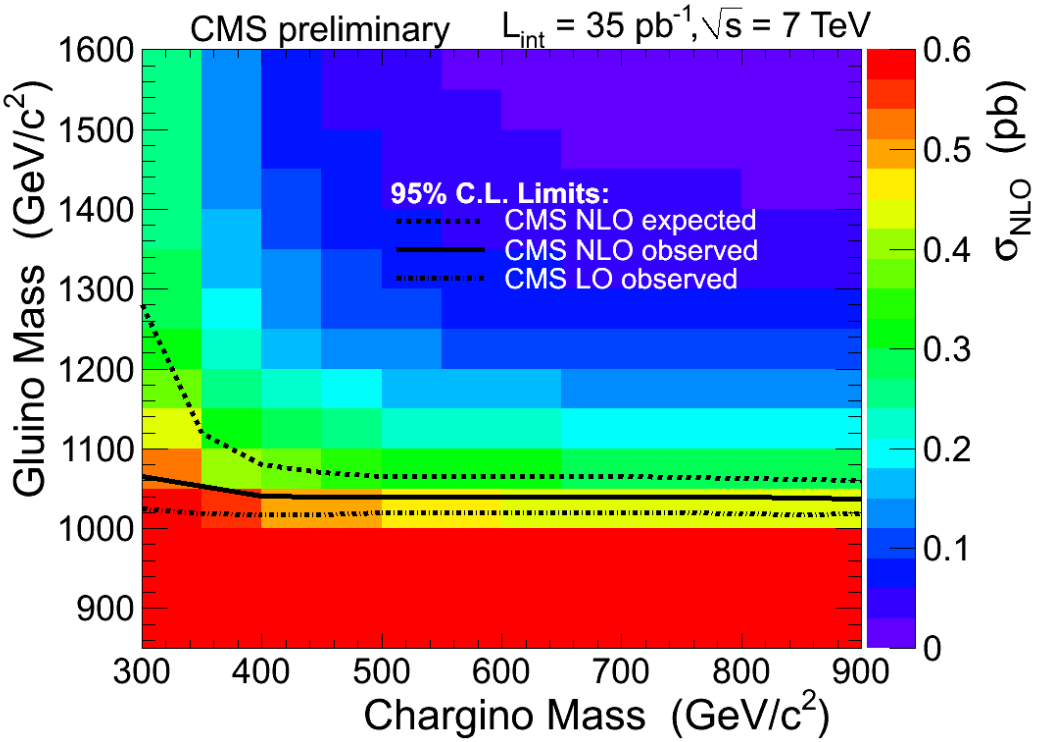

Figure 37: The scan for co-NLSP parameter space for tanβ = 3 [57]. Gluino masses up to 1040 GeV$/c^2$ are excluded with corresponding chargino masses shown here.

6 Conclusion

A search for supersymmetry in the final state with at least three leptons and substantial hadronic activities at the CMS detector has been presented in this dissertation. We use twenty-four channels, twelve channels each for the 3-lepton and 4-lepton modes.

mSUGRA with R-parity conservation has been assumed to calculate the characteristics of the new particles in a scan of benchmarks points. SUSY and SM events have been produced in MC and their detector response have been simulated making use of the CMS software framework.

All relevant standard model backgrounds have been taken into account and the effects of the main systematic uncertainties have been evaluated. An event selection is imposed in order to separate signal from background and the statistical test is performed with the Bayesian Calculator to estimate confidence levels for the exclusion limits.

The SM background rejection benefits strongly from the $H_T > 200$ GeV requirement, which preserves high signal efficiency for gluino cascade decays, where high p_{T} jets and well isolated leptons are present. Three events, one $e\mu\mu$, one $e\mu\tau$, and one $ee\tau$ event, pass with all cuts. The total backgrounds for those events are about 1.3 events at the present integrated luminosity.

The mSUGRA and GMSB parameter space has been explored with an integrated luminosity of 34.9 pb^{-1}. The exclusion region is approximately the same as that of the Tevatron experiments. Some regions of parameter space are excluded with the data accumulated so far while others need more integrated luminosity or better control over systematics. For the SUSY parameters of m_0 = 60 GeV/c^2, A_0 = 0, $tan\beta$ = 3, and $\mu > 0$, chargino masses below 163 GeV/c^2 are excluded in the mSUGRA model, and in the GMSB model, gluino masses up to 1040 GeV/c^2 are excluded in co-NLSP scenario.

In 2011, a few fb^{-1} of data is expected to be collected. With that much data, LS channels will play much stronger role in the limit setting. We did not consider the 3-lepton plus $E_{\mathrm{T}}^{\mathrm{miss}}$ signature from $\widetilde{\chi_2^0}\widetilde{\chi_1^{\pm}}$ direct production in this analysis given its smaller production cross section. It is possible to extend the search with that signature assuming more data are collected.

The challenge will be the trigger: the high trigger efficiency is no longer guaranteed by the single and double lepton triggers alone. The dedicated trilepton triggers have been proposed and implemented already in the 2011 run to ensure that the signal is retained.

References

[1] M. Dine. *Supersymmetry and String Theory*. Cambridge University Press, 2007.

[2] H. Baer et al. *Weak Scale Supersymmetry*. Cambridge University Press, 2006.

[3] M. Peskin et al. *An Introduction to Quantum Field Theory*. Westview Press, 1995.

[4] J. Terning. *Modern Supersymmetry: Dynamics and Duality*. Oxford Press, 2009.

[5] S. Martin. *A Supersymmetry Primer*. arXiv:hep-ph/9709356v5, 2008.

[6] The ALEPH DELPHI L3, OPAL Collaborations, and the LEP Working Group. *The LEP Working Group for Higgs Boson Searches*. arXive:0306033, 2003.

[7] The CDF and D0 collaborations. *Combined CDF and D0 Upper Limits on Standard Model Higgs-Boson Production with up to 6.7 fb-1 of Data*. Phys. Rev. Lett. 104, 2010.

[8] The LEP Collaborations: ALEPH Collaboration DELPHI Collaboration L3 Collaboration OPAL Collaboration the LEP Electroweak Working Group. *A Combination of Preliminary Electroweak Measurements and Constraints on the Standard Model*. arXive:0612034, 2006.

[9] The ALEPH DELPHI OPAL, SLD Collaborations the LEP Electroweak SLD Electroweak, and Heavy Flavour Working Groups. *Precision Electroweak Measurements on the Z Resonance*. Phys. Rept. 427, 2006.

[10] F. Zwicky. *Die Rotverschiebung von extragalaktischen Nebeln*. Helvetica Physica Acta 6: 110-127, 1933.

[11] G. Hinshaw et al. *Five-Year Wilkinson Microwave Anisotropy Probe (WMAP) Observations: Data Processing, Sky Maps, and Basic Results*. The Astrophysical Journal Supplement Series, 2008.

[12] J. Erler et al. *Review of Particle Physics*. The European Physical Journal C3: P. 103. Chapter 10.6, 2000.

[13] W. de Boer. *Comparison of grand unified theories with electroweak and strong coupling constants measured at LEP*. Phys. Lett. B. 260. 3-4. 447, 1991.

[14] H. Murayama. *Supersymmetry Phenomenology*. arXiv:hep-ph/0002232v2, 2000.

[15] R. Haag et al. *All possible generators of supersymmetries of the S-matrix*. Nucl. Phys. B 88. 257, 1975.

[16] S. Coleman et al. *All Possible Symmetries of the S Matrix*. Phys. Rev. 159. 1251, 1967.

[17] M. Malinsky. *MSSM Higgs sectors at the one-loop level*. Czechoslovak Journal of Physics, 2000-09-01.

[18] The CMS Collaboration. *CMS Physics, Technical Design Report Volume II: Physics Performance*. CERN/LHCC 2006-021, 2006.

[19] B.C. Allanach. *SOFTSUSY: a program for calculating supersymmetric spectra*. arXiv:hep-ph/0104145v15, 2010.

[20] T. Sjöstrand et al. *Pythia 6.4 Physics and Manual*. FERMILAB-PUB-06-052-CD-T, 2006.

[21] H. Baer et al. *The Reach of the CERN Large Hadron Collider for Gauge-Mediated Supersymmetry Breaking Models*. FSU-HEP-000328, 2000.

[22] R. L. Culbertson et al. *Low scale and gauge mediated supersymmetry breaking at the Fermilab Tevatron Run II*. arXive:hep-ph/0008070, 2000.

[23] V. E. Barnes et al. *Observation of a Hyperon with Strangeness Number Three*. Physical Review Letters 12 (8): p.204, 1964.

[24] D. Green. *The Physics of Particle Detectors*. Cambridge University Press, 2000.

[25] D. Green. *High p_T Physics at Hadron Colliders*. Cambridge University Press, 2005.

[26] The CMS Collaboration. *CMS Physics Technical Design Report Volume I: Detector Performance and Software*. CERN/LHCC 2006/001, 2006.

[27] LHC. LHC Design Report Volume I, II, III, 1997. URL http://lhc.web.cern.ch/lhc/LHC-DesignReport.html.

[28] CERN. Multimedia & Outreach, 2010. URL http://cdsweb.cern.ch/.

[29] The CMS Collaboration. Tracker Technical Design Report, 1999. URL http://cmsdoc.cern.ch/cms/TDR/TRACKER/tracker.html.

[30] The CMS Collaboration. The Tracker Project Technical Design Report, 1998. URL http://cmsdoc.cern.ch/cms/TDR/TRACKER/tracker.html.

[31] The CMS Collaboration. CMS ECAL Technical Design Report, 1997. URL http://cmsdoc.cern.ch/cms/TDR/ECAL/ecal.html.

[32] The CMS Collaboration. The CMS experiment at the CERNLHC, 2008.

[33] The CMS Collaboration. HCAL Technical Design Report, 1997. URL http://cmsdoc.cern.ch/cms/TDR/HCAL/hcal.html.

[34] The CMS Collaboration. The Magnet Project - Technical Design Report, 1998. URL http://cmsdoc.cern.ch/cms/TDR/MAGNET/magnethtml.

[35] The CMS Collaboration. CMS Muon Technical Design Report, 1997. URL http://cmsdoc.cern.ch/cms/TDR/MUON/muon.html.

[36] The CMS Collaboration. *CMS TriDAS Project Technical Designed Report Volume 1: the Trigger Systems*. CERN/LHCC 2000-38, 2000.

[37] W. Badgett et al. *Web based monitoring in the CMS experiment at CERN*. The open access Journal of Physics: Conference Series, in preparation.

[38] TOTEM Collaboration. *The TOTEM Experiment at the CERN Large Hadron Collider*. JINST 3 S08007, 2008.

[39] The CMS Collaboration. *CMS computing : Technical Design Report*. CERN-LHCC-2005-023, 2005.

[40] G. Abbiendi et al. *Muon Reconstruction in the CMS Detector*. CMS AN-2008/097, 2008.

[41] S. Baffioni et al. *Electron Reconstruction in CMS*. CMS NOTE 2006/40, 2006.

[42] M. Cacciari et al. *The anti-k_T jet clustering algorithm*. arXiv:0802.1189v2, 2008.

[43] The CMS Collaboration. *Determination of the Jet Energy Scale in CMS with pp Collisions at $\sqrt{s}$ = 7 TeV*. CMS PAS JME-10-010, 2010.

[44] The CMS collaboration. *$E_{\mathrm{T}}^{\mathrm{miss}}$ Reconstruction, Performance and Validation*. CMS AN-2008/089, 2008.

[45] The CMS Collaboration. *CMS Strategies for tau reconstruction and identification using particle-flow techniques*. CMS PAS PFT-08-001, 2008.

[46] P. Azzurri et al. *Commissioning of the Particle-Flow reconstruction in Minimum-Bias and Jet Events from pp Collisions at 7 TeV*. PFT-10-002, 2010.

[47] F. Paige et al. ISAJET 7.75, A Monte Carlo Event Generator for pp, $\bar{p}p$, and e^+e^- Reactions, 2007. URL `http://www.hep.fsu.edu/~isajet/`.

[48] W. Beenakker et al. *PROSPINO: A Program for the Production of Supersymmetric Particles in Next-to-leading Order QCD*. arXiv:hep-ph/9611232v1, 1996.

[49] M. Chertok et al. *SUSY multilepton searches with electrons, muons, and taus*. CMS AN-10-231, 2010.

[50] J. Pumplin et al. *New generation of parton distributions with uncertainties from global QCD analysis*. JHEP 0207:012, 2002.

[51] A. Djouadi et al. *Decays of Supersymmetric Particles: the program SUSY-HIT (SUspect-SdecaY-Hdecay-InTerface)*. arXiv:hep-ph/0609292v1, 2006.

[52] J. Allison et al. *Geant4 developments and applications IEEE Trans*. Nucl. Sci. 53 270-278, 2006.

[53] The ROOT team. The ROOT Users Guide, 2009. URL `http://root.cern.ch/drupal/`.

[54] M. Mulders et al. *Muon Identification in CMS*. CMS AN 2008/098, 2008.

[55] J. Alcaraz Maestre et al. *Updated Measurements of Inclusive W and Z Cross Sections at $7\,TeV$*. CMS AN-10-264, 2010.

[56] A. Harel et al. *Calorimeter Jet Quality Criteria for the First CMS Collision Data, and preparations for calibrating their efficiencies*. CMS AN-2009/087, 2009.

[57] The CMS Collaboration. *Search for Physics Beyond the Standard Model Using Multilepton Signatures in $\sqrt{s}$ = 7 TeV pp Collisions with the CMS Detector at the LHC*. CMS PAS SUS-10-008, 2010.

[58] The CMS Collaboration. *Studies of Tracker Material*. CMS PAS TRK-10-003, 2010.

[59] The CMS Collaboration. *Measurement of CMS Luminosity*. CMS PAS EWK-10-004, 2010.

[60] R. Gavin et al. *FEWZ 2.0: A code for hadronic Z production at next-to-next-to-leading order*. arXiv:1011.3540v1, 2010.

[61] J. Campbell et al. *MCFM for the Tevatron and the LHC*. arXiv:1007.3492v1, 2010.

[62] N. Kidonakis. *NNLL resummation for s-channel single top quark production*. arXiv:1001.5034v2, 2010.

[63] G. Cowan. *Statistical Data Analysis*. Oxford University Press, 1998.

[64] P. Bevington. *Data Reduction and Error Analysis for the Physical Sciences, 3rd ed*. McGraw Hill, 2003.

[65] L. Lyons. *Statistics for nuclear and particle physicists*. Cambridge University Press, 1986.

[66] The CMS Collaboration. Muon Tau Replacement with Particle-Flow, 2010. URL `https://twiki.cern.ch/twiki/bin/view/CMS/MuonTauReplacementWithPFlow`.

[67] J. Conway et al. *Estimation of Background contributions to Tau analyses via Fake–Rate technique*. CMS AN10-74, 2010.

A Background Studies

In the following sections, the SM background important for this analysis are reviewed.

QCD and Z+jets processes are estimated from the data with data-driven techniques because lepton fakes are not necessarily modeled well in the MC.

VV+jets and $t\bar{t}$ +jets are the dominant backgrounds and MC samples are trusted. Double vector boson production is an irreducible background because it contains three or four prompt leptons, and its uncertainty comes mainly from its cross section. The $t\bar{t}$ +jets background have two prompt leptons from Ws and b-quark and/or other jets. The probability of a jet faking an electron/muon is assumed to be similar to that for QCD, so the fake electron and muon contributions are negligible in electron and muon channels. For the tau channels, a fake rate analysis is done with the data and MC and appropriate uncertainty is assigned to those channels.

A.1 QCD Background

Lepton isolation has been studied for both data and MC [49]. The QCD MC sample, requiring a scattered muon with p_{T} >15 GeV, agrees with the data within 50% which is adequate. The method outlined in the reference shows that the QCD background is expected to be $\lesssim 0.002$ for the electron and muon channels. The distribution of lepton isolation is shown in Fig. 38.

The conclusion is that QCD background is negligible for this analysis.

A.2 Z+jets Background

A.2.1 Dilepton Mass

The Z+jets is one of the dominant background in the two electrons/muons plus tau(s) channels. Furthermore, it provides an interesting check of the cross selection and analysis code. Therefore this section is designated to the Z bosons. Clearly visible Z mass peak is expected at M(ll) =

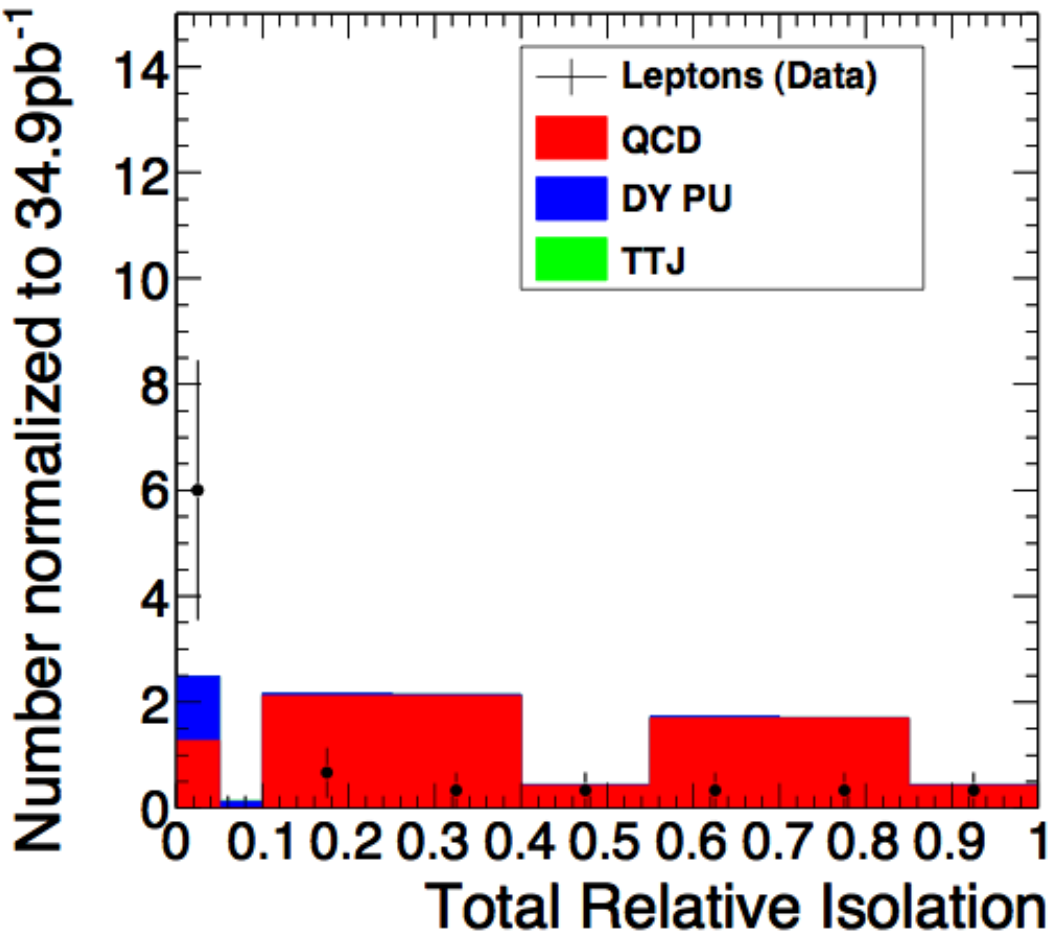

Figure 38: The distribution of relative isolation for 3μ for MC with data overlaid. The data (points with error bars) correspond to the 34.9 pb^{-1} sample available in 2010. MC is normalized to the same luminosity [49] for comparison.

90 GeV/c^2. The mass is plotted in Fig. 39 with the lepton cuts described in Sec. 5.4. The Z peak is at the expected dilepton mass in the data and MC.

The width of the peak agrees well in the data and MC particularly for SFOS muons. The one of SFOS electrons exhibits a shift toward lower value, indicating an mismatch between electron energy scale between the data and MC. A correction is not applied in this analysis since the shape of the Z peak does not affect the analysis directly, although there is indirect effect with the offline p_{T} cut, but this is small.

The SS dimuon sample has no events in the Z mass region. However for electrons, a Z peak is visible. MC predicts that there are about 0.5% as many events as in the OS signal, while the rate for data is about 20% larger. Since either electron could have the charge misassigned, the misidentified rate is about 0.3% for electrons. For the 3 and 4-lepton analysis, this does

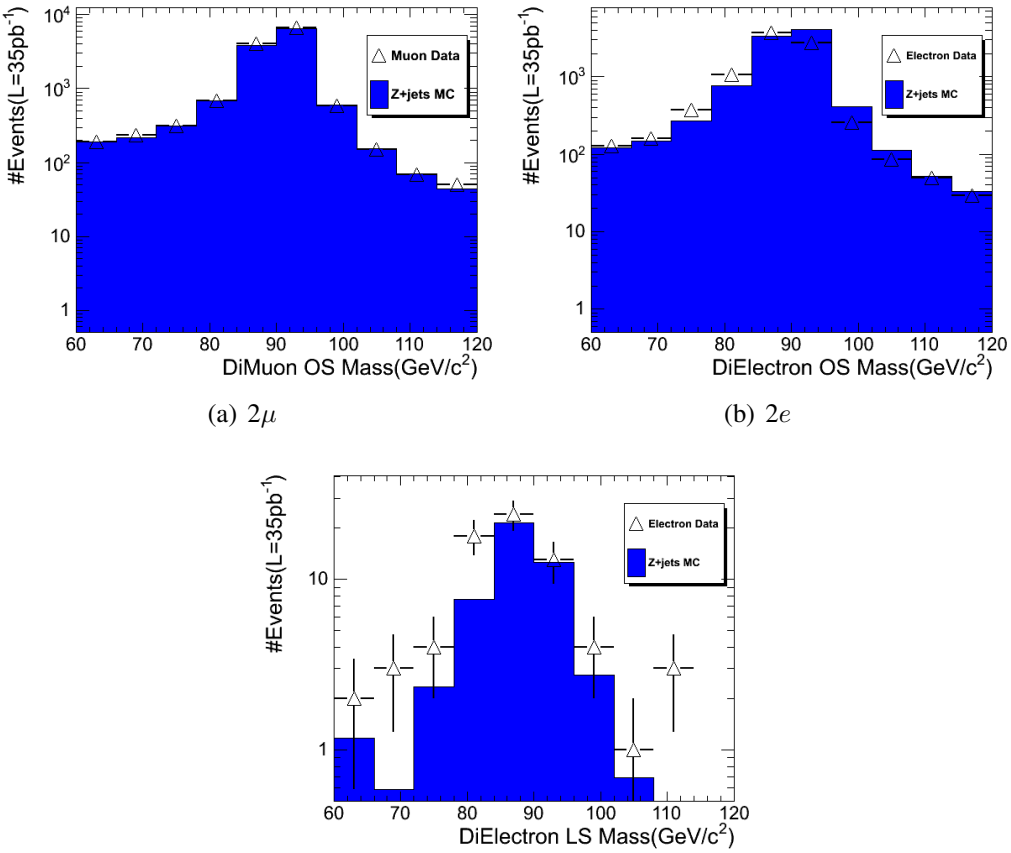

(a) 2μ (b) $2e$

(c) 2 LS e

Figure 39: The dilepton invariant mass distribution for $\mu^+\mu^-$ data and background MC and e^+e^- data. The only significant background in this region is from Z+jets events. Data agree with MC well besides the shift in M(ee) distribution. There is no event in LS muon channel both data and MC, and the agreement between data and MC is also good in LS electron channel.

not present a problem since the backgrounds are already very low for the SS pairs, even for channels with a tau.

A.2.2 Trilepton Events without H_T and $E_{\mathrm{T}}^{\mathrm{miss}}$ Cuts

An important source of backgrounds for this analysis is dilepton events where an extra isolated lepton is found. In order to compare how often the third lepton is found in data and MC, the number of events are compared with all cuts except H_T for electron and muon channels.

The comparison of data to MC for the range $80 < m_{\ell\ell} < 100$ is shown in Fig. 40.

The fake rate in data seems larger than in MC though the errors are still large.

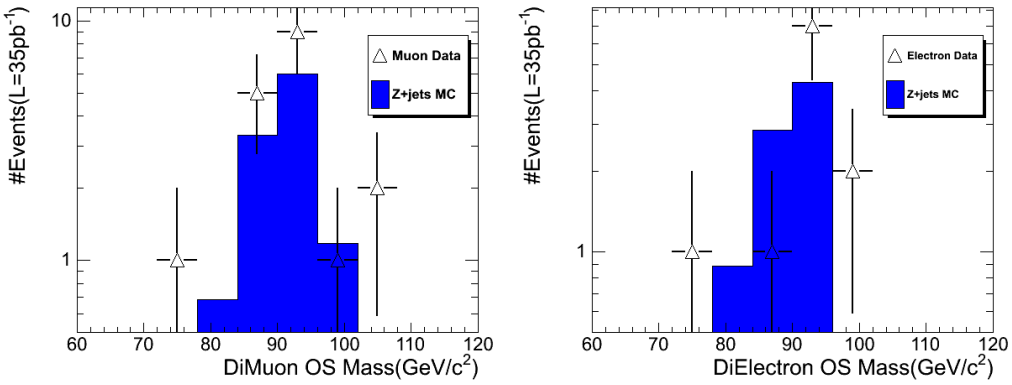

(a) 3μ (b) $3e$

Figure 40: The dimuon invariant mass distribution for 3μ and $3e$ events. There must be a well-isolated muon/electron pair. The third one passes lepton selection except isolation requirement to have sizable number of events. Data agree with MC well.

A.3 VV+jets and $t\bar{t}$ +jets Backgrounds

The backgrounds discussed in previous sections are negligible after all cuts applied. Two important backgrounds are VV+jets and $t\bar{t}$ +jets. The former is the largest background for most channels while the latter tends to be large for the channels with taus. The VV+jets background has prompt leptons, and thus the fake rate estimates discussed in the previous sections are not relevant. The MC estimated is trusted, $i.e.$, kinematics of the events, with systematic uncertainties described in Sec. 5.6.

The $t\bar{t}$ +jets background is significant for all channels, and becomes dominant for the channels with taus. The main background involves two real leptons from the decay of top quarks and a tau candidate from the b-quark or other jets. Four data events are found and three MC events expected, 90% of which is due to $t\bar{t}$ +jets process, in $e\mu\tau$ channel with $H_T > 30$ GeV ($i.e.$, at least one jet) as shown in Fig. 41.

The conclusion is that $t\bar{t}$ +jets MC sample reasonably models the data.

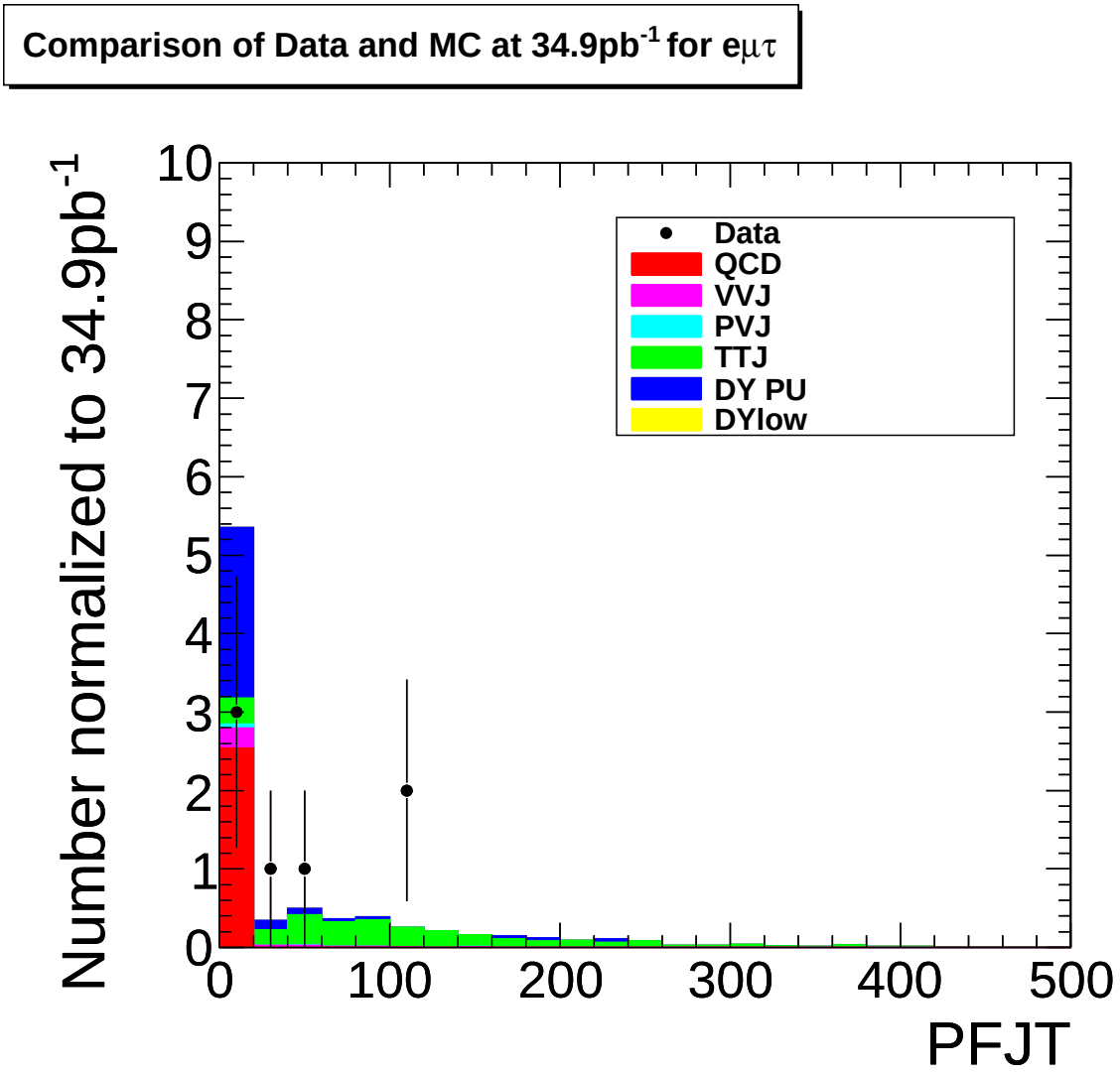

Figure 41: H_T (=J_T in the plot) distributions for $e\mu\tau$ data with MC expectations overlaid. The luminosity = 34.9 pb^{-1} [49]. To focus on $t\bar{t}$ +jets sample, at least one jet with $E_{\rm T} > 30$ GeV is required before checking the agreement between the data and MC.

B Additional Studies on Tau

The tau physics organization group uses a $Z \rightarrow \tau\tau \rightarrow \mu\tau_h$ selection to determine the uncertainty on the hadronic tau identification efficiency for 2010 data.

Comparison of data and MC is performed using template fitting of the visible muon plus tau mass and results are provided for some tau identification algorithms. In conjunction with this, we perform two studies to provide determination of effects due to pile up and the hadronic environment expected for the SUSY signal with high hadronic activity. These are small, and the dominant relative uncertainty of 30% stems from the statistical uncertainties of the template fitting method as found by the tau group.

B.1 Effect of Hadronic Environment on Tau ID Using Random Cone Technique

Taus are constructed from jets with radius of R=0.5. The constituents of a jet are mostly contained inside the cone, because most of the hadrons go in the direction of the original color particle. However some jet particles may end up outside of the cone. There is no resulting effect in the events where only a few jets are present, because prompt leptons are likely to be well-separated from the jet.

The situation is quite different if many jets are present in the events. In this case, such as SUSY production of squarks plus gluinos, there is a non-negligible effect on lepton isolation from particles leaking out from the jet cone. To quantify such an effect, we study the jet data and QCD ($\widehat{p_{\mathrm{T}}} > 120$ GeV) MC samples, where $H_T > 200$ GeV is required. The choice of the $\widehat{p_{\mathrm{T}}}$ is motivated from the single jet trigger threshold, 140 GeV. A cone of R= 0.5 is randomly added, and the isolation used for tau reconstruction is determined.

The isolation efficiency computed this way depends on jet multiplicity of events, which is not the same in the both cases. The relevant quantity we are interested in is not the absolute isolation efficiency but the isolation efficiency dependence of ΔR from the nearest jet. This dependence

is plotted in Fig. 42, and the agreement between the data and MC is excellent between the range of $0.5 < \Delta R < 0.95$.

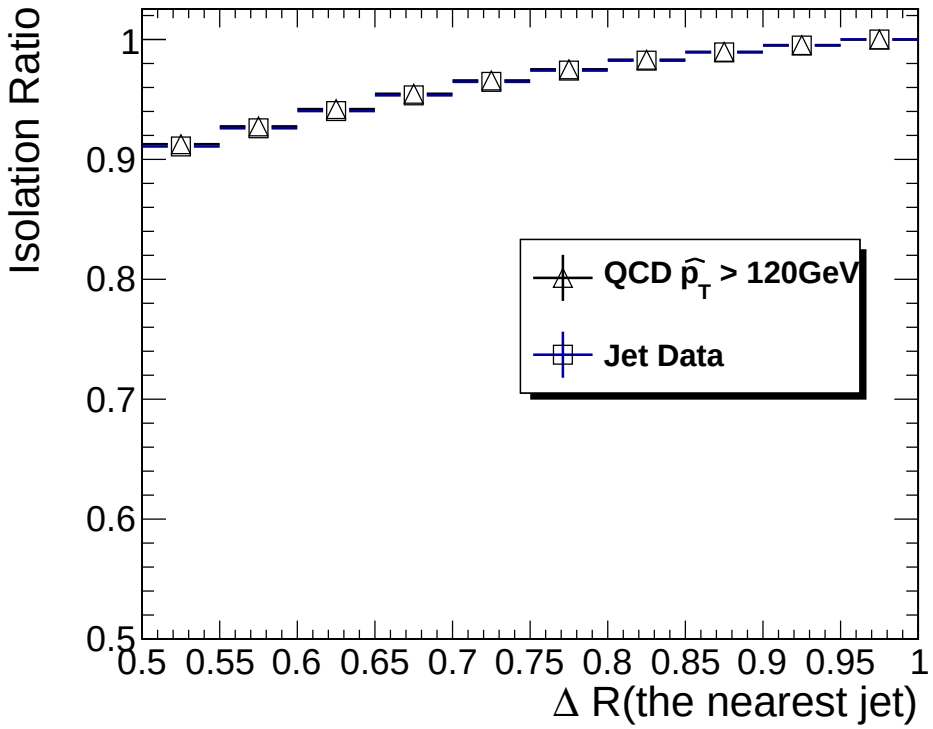

Figure 42: The effect on isolation from the jet products leaking outside the jet cone, in the data and MC. The ΔR is computed with respect to the nearest jet with at least having $E_{\mathrm{T}} > 10$ GeV. The effect, isolation ratio, is measured as a difference from the isolation efficiency at ΔR = 0.95 ($i.e.$, normalized to the value at ΔR = 0.95).

The difference of the ΔR dependance in this region is an order of one percent, which is much smaller than the other systematic uncertainties ($e.g.$, the luminosity error alone is $\sim$ 10 %) and thus we conclude this specific effect is negligible.

B.2 Monte Carlo Embedding Technique

We use a MC Embedding technique [66] to estimate the effects of pileup events on the tau efficiency assuming an electroweak event environment (with Z event selection). This is performed as follows.

- Z$\rightarrow \mu\mu$ events are selected with Vector Boson Task Force (VBTF) selection [55] from muon data

- a muon leg with relative isolation less than 0.06 is tagged, while no isolation required on the other muon leg as a probe
- the two muon legs are replaced with MC taus in the direction of the muons
- the tau reconstruction efficiency is computed with the replaced taus. The tagged muon is not used for computation of tau reconstruction efficiency

The underlying event is independent of how the Z boson decays: $Z \rightarrow \tau\tau$ events are affected in the same way as $Z \rightarrow \mu\mu$ events. OS muon pairs with invariant mass between 60 and 120 GeV$/c^2$ are replaced with MC taus from Z bosons while the rest of the event content is kept unaltered. Thus, these MC events are Z$\rightarrow \tau\tau$ events that are affected by real underlying event activity. The MC events are then reconstructed in the standard way. The reconstructed taus are expected to have lower reconstruction efficiency compared to those in MC events after detector simulation.

Due to pileup events, extra tracks in the signal cone can cause the candidates to fail the prong cut, and extra tracks or electromagnetic energy deposits in the isolation annulus can cause the isolation requirement to fail. The tau selection is the same as the main analysis. We compare data from Runs 145762-148058 with $Z \rightarrow \tau^+\tau^-$ MC. The ratio of data (embedding) to MC efficiency is $0.97\pm$0.02. The effect is negligible compared to other systematic uncertainties.

B.3 Tau Reconstruction Efficiency

The tau reconstruction efficiency is plotted as a function of MC tau p_{T} (ν momentum not subtracted) and η in Fig. 43.

The denominator is the number of jets with $p_{\mathrm{T}} > 8$ GeV and $|\eta| < 2.1$. The numerator is the denominator passing the requirements described in the subsection 5.4.3. The results indicate that the efficiency is still non-zero even at the lowest p_{T}. As hadronic tau decays from SUSY production can be quite soft, this analysis makes a point to reconstruct their hadronic decays as low in p_{T} as possible.

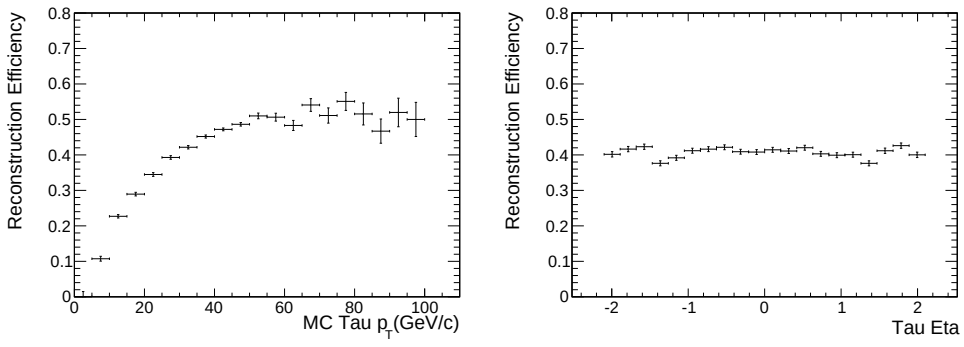

(a) p_{T} (b) η

Figure 43: Tau reconstruction efficiency as a function of MC tau p_{T} (ν momentum not subtracted) and η. The MC sample is $Z \rightarrow \tau\tau$.

C Tau Fake Rate Method

The dominant background in the OS dielectron and dimuon plus tau channels before all cuts are applied comes from Z+jets. We derive and employ a fake rate method to estimate its contribution. We start with events containing a well-isolated muon pair and then search for an additional jet. By weighting each jet with a fake rate, we predict the number of events in the tau channels. This number can be compared with actual number of events after the tau ID is applied. The SUSY signal is still swamped by Z+jets process at this point: however, event level cuts can be applied to reduce these to a manageable level.

For this study, jets with $E_{\mathrm{T}} > 8$ GeV and $|\eta| < 2.1$ are counted in an event. The probability of such a jet faking a tau can be measured with real data as well as MC samples by calculating the ratio:

$$\frac{\text{\#(Jets passing tau requirements)}}{\text{\#(Jets with } E_{\mathrm{T}} \text{ and } \eta \text{ cuts)}} \tag{78}$$

in events where the vast majority of jets are not true taus decaying to hadrons. For this purpose we choose samples, from MC and data, containing exactly one isolated muon.

Following the tau group, we parametrize the fake rate in E_{T}, $|\eta|$, and E_{T} weighted jet width, $R_{jet} = \sqrt{E(\eta^2) + E(\phi^2)}$, where $E(\eta^2)$ is a second moment of η as described in [67]. The fake rate in E_{T}, η, and ϕ and quark flavor dependence from MC is given in Fig. 44. Evaluation of the fake rate is summarized in Table 14 with W+jets, Z+jets, $t\bar{t}$ +jets MC, and muon data, where we select $Z \to \mu\mu$ candidates in data, and apply the parametrized fake rate (from each sample) to each jet to measure the probability of promoting a Z+jets event to a $\ell\ell\tau$ candidate.

The worst agreement is between the Z (data) and estimate with $t\bar{t}$ +jets MC samples: We interpret the $\sim 30\%$ difference as a measure of the systematic uncertainty of the fake rate method. The origin of this disagreement can be seen in Fig. 44.

The fake rate for b quarks is lower than other quark flavors. There are more b quarks with high enough p_{T} to be reconstructed as a jet in $t\bar{t}$ events. We note that some care must be taken to apply the fake rate method in MC-data comparisons. Any disagreement in the distribution of

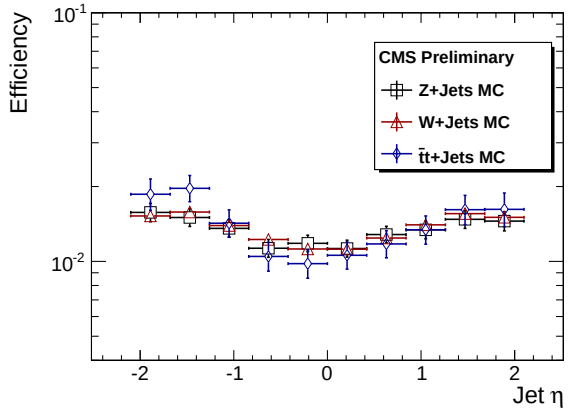

(a) Fake Rate vs η.

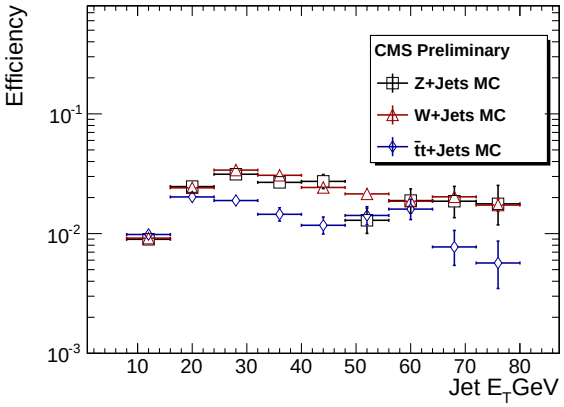

(b) Fake Rate vs E_{T}.

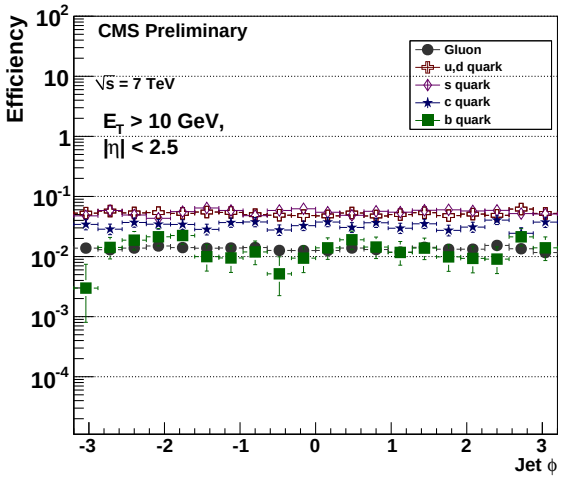

(c) Quark flavor dependence in ϕ.

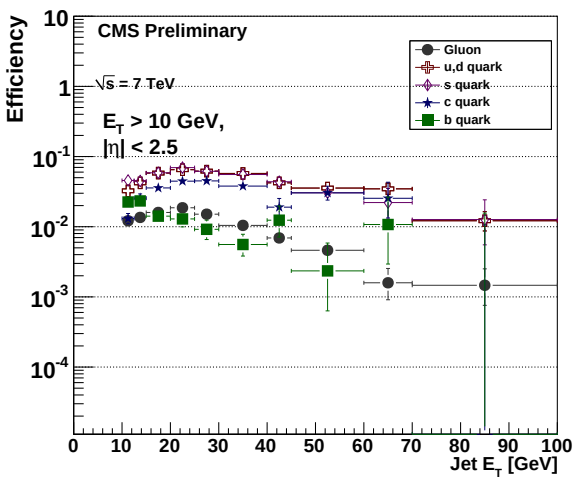

(d) Quark flavor dependence in E_{T}

Figure 44: Tau fake rate comparison among W+jets, Z+jets, $t\bar{t}$ +jets MC samples, and quark flavor dependence from QCD (Pythia8) MC sample.

the number of jets must first be adjusted before the fake rate method can be applied.

Sample	Estimated #Events / #Events after tauID (%)
W+jets MC	101.6 $\pm$7.9
Z+jets MC	96.8 $\pm$7.6
$t\bar{t}$ +jets MC	73.0 $\pm$5.7
1μ + $E_{\mathrm{T}}^{\mathrm{miss}}$ Data	115.5 $\pm$9.0

Table 14: Evaluation of the tau fake rate method with data. First, fake rates are extracted from W+jets, Z+jets, $t\bar{t}$ +jets MC, and muon data having exactly one isolated global muon with $p_{\mathrm{T}} > 8\mathrm{GeV}/c$, $|\eta| < 2.1$, and $E_{\mathrm{T}}^{\mathrm{miss}} > 20$ GeV. Then, #events is computed with those fake rates in muon data having exactly two isolated global muons with $p_{\mathrm{T}} > 8\mathrm{GeV}/c$, $|\eta| < 2.1$, and OS dimuon mass between 60 and 120 GeV$/c^2$. As the conditions differ, there is no overlap at all between one and two muon selection for the data ($i.e.$, the event used only once if used). Statistical uncertainty is from #events after tauID in 2μ data. The muon data used for this section is 8 and 19 pb^{-1} for 1μ + $E_{\mathrm{T}}^{\mathrm{miss}}$ and 2μ selection respectively.

D L1 Tau Trigger Algorithm

The tau trigger is not a main trigger used in this analysis as we rely on leptonic triggers in 2010 run. The high trigger efficiency relies on electron, muon, and cross triggers. Like other physics objects, online taus are reconstructed in a similar way in offline. While the HLT is almost identical to offline reconstruction, the L1 tau trigger is quite different because of the lack of tracking information.

L1 tau trigger starts with trigger primitives of calorimeter towers, with a certain threshold value. Hadronically decaying taus are reconstructed as jets. It is, in general, hard to distinguish taus from QCD jets. The jets are characterized by their transverse energy distribution, in terms of collimation and isolation, as they are in offline reconstruction. To quantify jet collimation, the shape of the active region is grouped into tau-like and QCD-like ones. The tau-like ones do not have an active calotower separated from other active towers. The QCD-like ones have active towers which have at least one separated calotower from the rest of them. The pattern of active regions is shown in Fig. 45.

Once the active region is checked in the core region of 3×3 sliding window algorithm, the transverse energies of eight neighbor regions are checked to determine the isolation of the jet (at the endcap transition area, 2×3 window is used by considering the gap region). The threshold value for the isolation requirement can be different from the threshold used to determine the active region. QCD jets tend to deposit energy in a wider area, while taus tend to be isolated by assuming a heavy particle as a mother of the taus.

The use of the isolation cut reduces QCD jets by ~ 30 %, while almost no effect for tau jets. The efficiency is plotted in Fig. 46.

This was proposed before the data taking and thus implemented in the 2010 run. It is expected to be the same for the 2011 run, with possible change in threshold values for the activity and isolation cuts. In the HLT, the tau triggers use PF algorithm as in offline reconstruction.

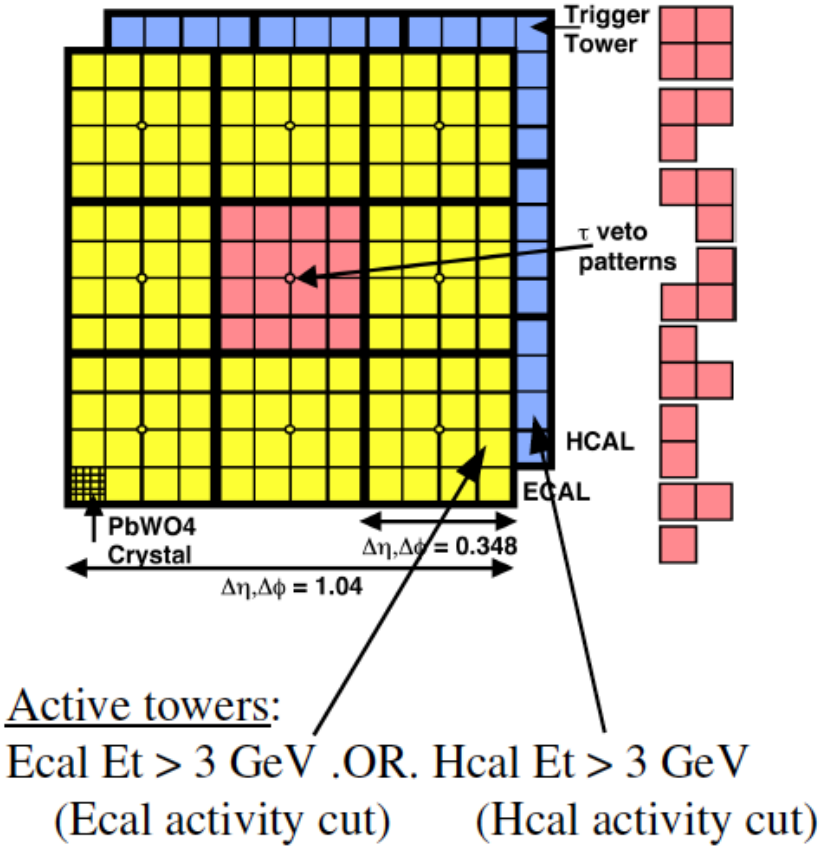

Figure 45: Level 1 tau trigger algorithm [36]. Yellow cells are ECAL towers, and blue cells are HCAL towers. The good patterns of active trigger towers are summarized on the right.

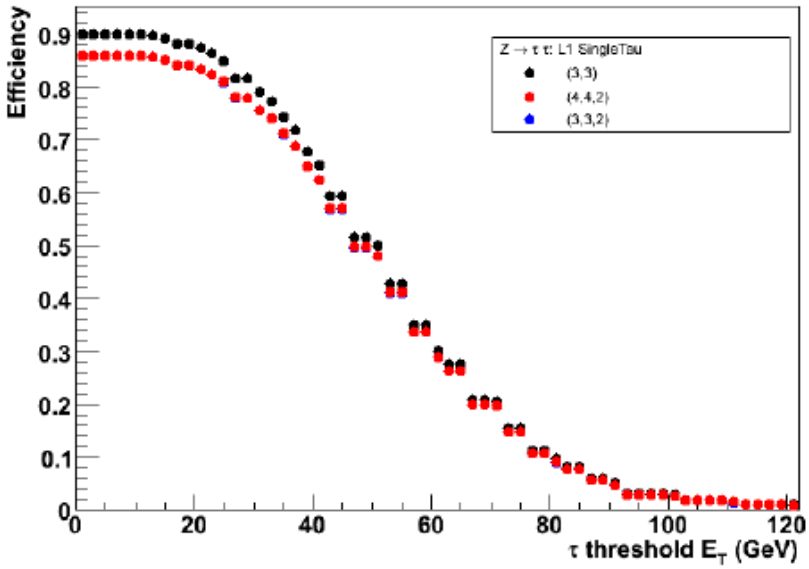

Figure 46: Level 1 tau trigger efficiency for different configurations. (3,3) one is an older algorithm without isolation. (4,4,2) and (3,3,2) are newer an algorithm with different threshold values. The first two are threshold values for ECAL and HCAL active towers, and the last one is for the isolation requirement. For the $Z \rightarrow \tau\tau$ sample, there is almost no effect on its trigger efficiency, as expected from the Lorentz boost.

E Trigger Cross section Monitor

Since triggering is of vital importance at the LHC, extreme rate environment, it is critical to monitor trigger performance during every shift of data taking. We have created Trigger Cross section Monitor (TXMon) for this purpose. The goal of this task is two-fold:

- Provide trigger rate projection for higher luminosity to help trigger menu design
- In online, monitor rates of each trigger and alarm appropriately if they are out of allowed bounds. In order to do that the process must know
  - current instantaneous luminosity
  - expected rates and acceptable bounds of each trigger
  - current trigger rate of each trigger
  - trigger menu including prescale factors

Here, we describe how data are obtained and processed. Application to offline is full-fledged, in the sense that all implemented features are available.

E.1 Application to Offline

E.1.1 Inputs

TXMon is a java servlet and it sends queries to database to obtain following information:

- TSCSummaryKey from CMS_WBM.RUNSUMMARY
- L1Menu from CMS_GT.GT_SETUP
- GTRunSettingsKey from CMS_GT.GT_RUN_SETTINGS_KEY_HISTORY

- LUMISECTION, INSTLUMI, and INSTLUMIERROR from CMS_RUNTIME_LOGGER.LUMI_SECTIONS
- BIT, LUMISEGMENTNR, TIME, and GTALGOCOUNTS from CMS_WBM.LEVEL1_TRIGGER_ALGO_CONDITIONS
- BIT, LUMISEGMENTNR, TIME, and GTTECHCOUNTS from CMS_WBM.LEVEL1_TRIGGER_TECH_CONDITIONS

The first three items are used to filter runs to ensure the same run and trigger conditions. The last three items are used to compute trigger rate and cross sections.

E.1.2 Matching

When instantaneous luminosity information is used, matching between LUMISECTION and LUMISEGMENTNR in the same run is performed. If INSTLUMI is negative or zero, the corresponding LUMISEGMENTNR is ignored. When INSTLUMI information is not used at all, no matching is performed and no point is dropped.

E.1.3 Calculation

The trigger rates are calculated as following:

$$Rate = \frac{Counts}{LumiSection} \tag{79}$$

where LumiSection (LS) is pre-defined as about 23.1 seconds for 7 TeV collision runs. The trigger cross section is defined as following:

$$\sigma_{trigger} = \frac{TriggerRate}{instantaneous\,Luminosity} \tag{80}$$

The uncertainties are propagated as follows. The only exception from computation of error is LS. The uncertainties of trigger rate is defined as

$$\delta Rate = \frac{\delta Counts}{LumiSection} = \frac{\sqrt{Counts}}{LumiSection} \tag{81}$$

The error of trigger cross section is defined as

$$\begin{aligned} \delta\sigma_{trigger} &= \sqrt{\left(\frac{\delta Rate}{L}\right)^2 + \left(\frac{Rate}{\delta L}\right)^2} \\ &= \sqrt{\left(\frac{\sqrt{Counts}}{LS \times L}\right)^2 + \left(\frac{Rate \times L\,Error}{(L)^2}\right)^2} \end{aligned}$$

where instantaneous lumi error is obtained from database, and L = instantaneous luminosity.

E.1.4 Fit

Currently, there are five fit options available: from zero to third degree polynomials and inverse plus second degree polynomial functions. The fit is done in ROOT with a function call: TGraphAsymmErrors::Fit().

The default fit mode is to try all formulae, and choose a formula with the smallest normalized χ^2. If any point has a zero count, the normalized residual squared is computed instead to keep ROOT from crashing. In other words, both rate and cross section have a zero error when its count is precisely zero. Having zero error causes computation of χ^2 fail because it takes a ratio of value and its error. One may argue that computation of χ^2 fails because the error of zero count is ill-defined. In the fit, we just avoid complexity of definition of an error with zero count, by switching from χ^2 to residual squared.

One may force TXMon to use a fit formula when only one of formulae is expected to describe rate or cross section. There are eight types of plot options are available

- L1 Algo Rate vs Time
- L1 Tech Rate vs Time

- L1 Algo Ratio vs Time
- L1 Tech Ratio vs Time
- L1 Algo Ratio vs L1 Tech Rate
- L1 Tech Ratio vs L1 Tech Rate
- L1 Algo Cross section vs Instantaneous Lumi
- L1 Tech Cross section vs Instantaneous Lumi
- L1 Algo Rate vs Instantaneous Lumi

When ratio of L1 trigger rate is chosen, a user must specify which L1 Tech bit is to be used. Available plot options are:

- Run range or Run list
- Cut off value
- Reference L1 Tech Bit

Note that not necessarily all runs from a run range or run list that a user enters are actually used for fit based on possibly different run conditions. The points below a cut off value are not used for fit.

E.1.5 Limitation

The user interactive fitter service has a limitation on number of runs, which is 100 in run range and 20 in run list. The fitter service is for trigger experts only to check few recent runs. An example is shown in Fig. 47.

In case of unbearable heavy traffic to database connection originated from the fitter, the service may be dropped from production machine at any moment.

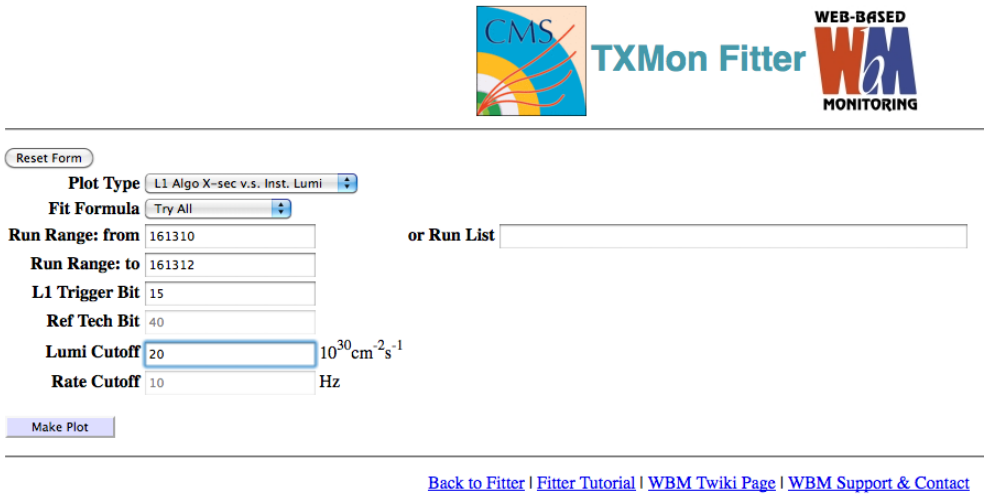

(a) an example query

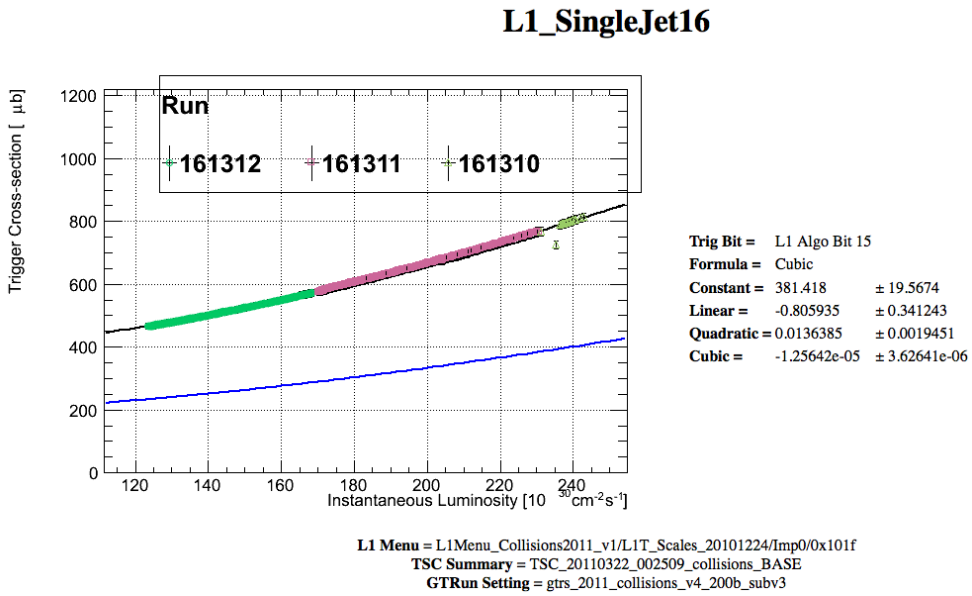

(b) the resulting plot and fit

Figure 47: The interactive TXMonFitter service is developed for trigger experts who want to check the instantaneous lumi dependence of trigger rates. It provides various fit options and returns a plot with fit result.

The HLT version of TXMonFitter is not yet available. However, the trigger cross sections of HLT paths are computed as for L1 paths. All plots are replaced with new ones daily on the 'TriggerHistory' page of WBM.

E.2 Application to Online

Fit results are prepared with following conditions:

- Fit formula set to the inverse plus second degree polynomial
- 7 TeV Runs in 2010-11

The fit results are put into database and read from ‘TriggerRates’ servlet. We will prepare new a set of fit results when instantaneous luminosity significantly increases.

F Candidate Events

F.1 Candidate Trilepton + H_T Event #1

The following table and event displays give the details of this event.

Event Type	$\mu^+\mu^-e^+$		
Run #	148864		
Event #	594577419		
H_T (GeV)	246.4		
pfMET (GeV)	39.1		
Lepton/Jet	p_T or E_T (GeV)	η	ϕ
μ^-	21.8	0.18	-0.43
μ^+	14.5	0.68	2.34
e^+	129.5	0.87	-2.00
Jet 1	172.0	-1.34	0.83
Jet 2	74.4	-1.13	1.62

Table 15: Trilepton + H_T candidate #1. Dimuon mass is 36.0 GeV

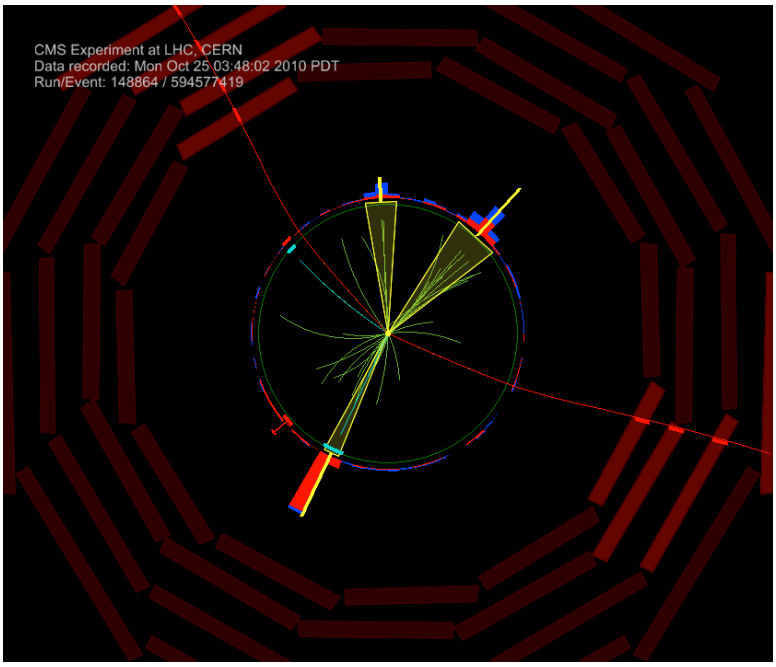

Figure 48: $\mu^+\mu^-e^+$ event. The high energy positron is visible at 7:00.

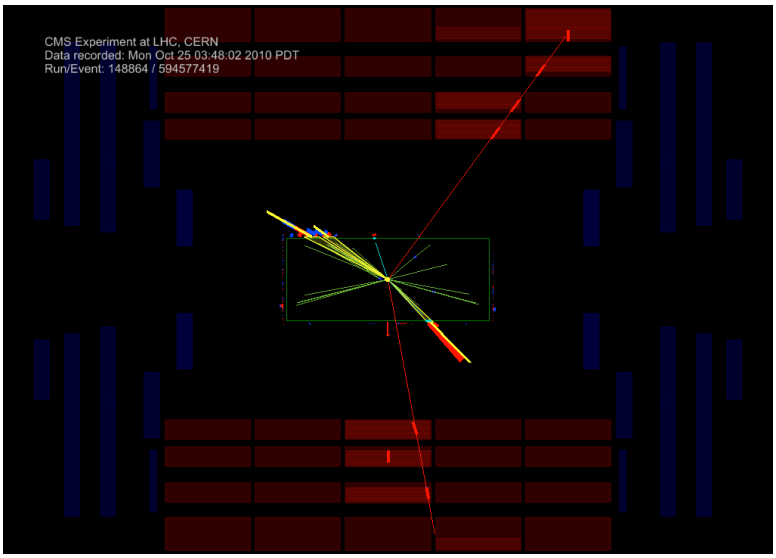

Figure 49: $\mu^+\mu^-e^+$ event

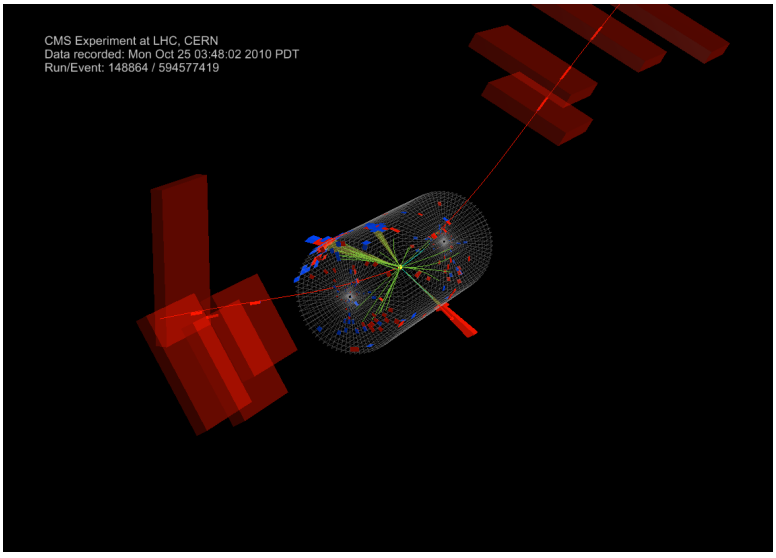

Figure 50: $\mu^+\mu^-e^+$ event

F.2 Candidate Trilepton + H_T Event #2

The following table and event displays give the details of this event.

Event Type	$e^+e^-\tau^+$		
Run #	149011		
Event #	701132117		
H_T (GeV)	384.3		
pfMET (GeV)	79.5		
Lepton/Jet	p_T or E_T (GeV)	η	ϕ
e^+	106.7	-1.98	2.12
e^-	29.5	-0.73	0.13
τ^+(1-prong)	13.1	-1.61	0.95
Jet 1	138.0	-0.82	2.74
Jet 2	107.3	0.68	-1.09
Jet 3	84.5	0.21	-0.18
Jet 4	54.4	-1.46	-2.80

Table 16: Trilepton + H_T candidate #2. Dielectron mass is 119.7 GeV. This event is accepted in the top quark pair analysis. One jet contains a low p_T muon, and the hadronic tau decay track, plus other nearby tracks, create a tagged secondary vertex.

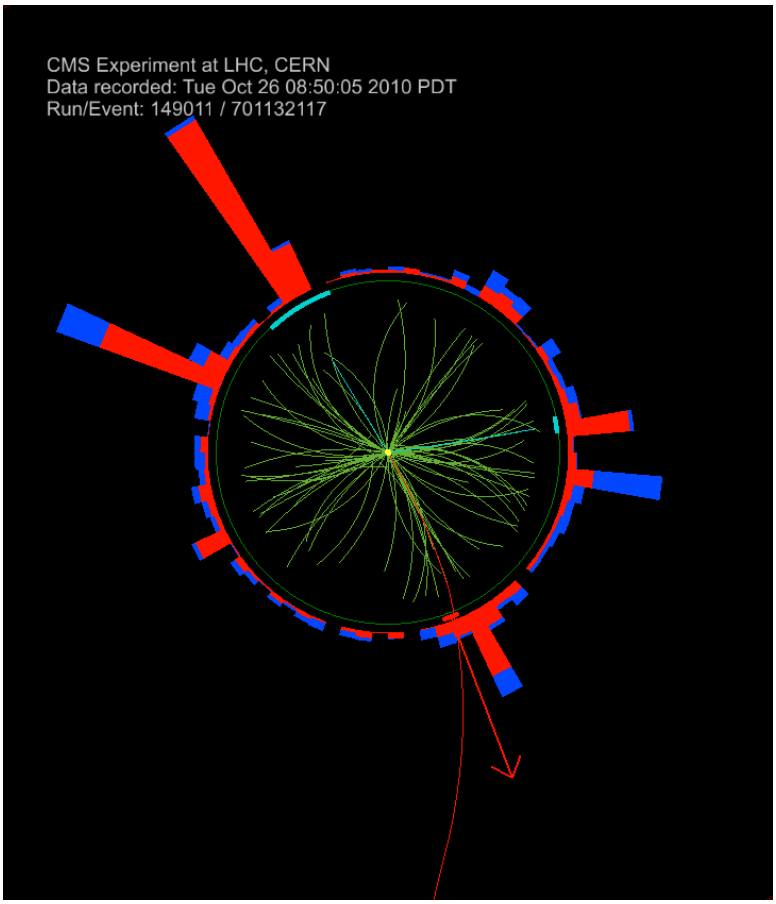

Figure 51: $e^+e^-\tau^+$ event. The hadronic tau decay is visible around 1:00.

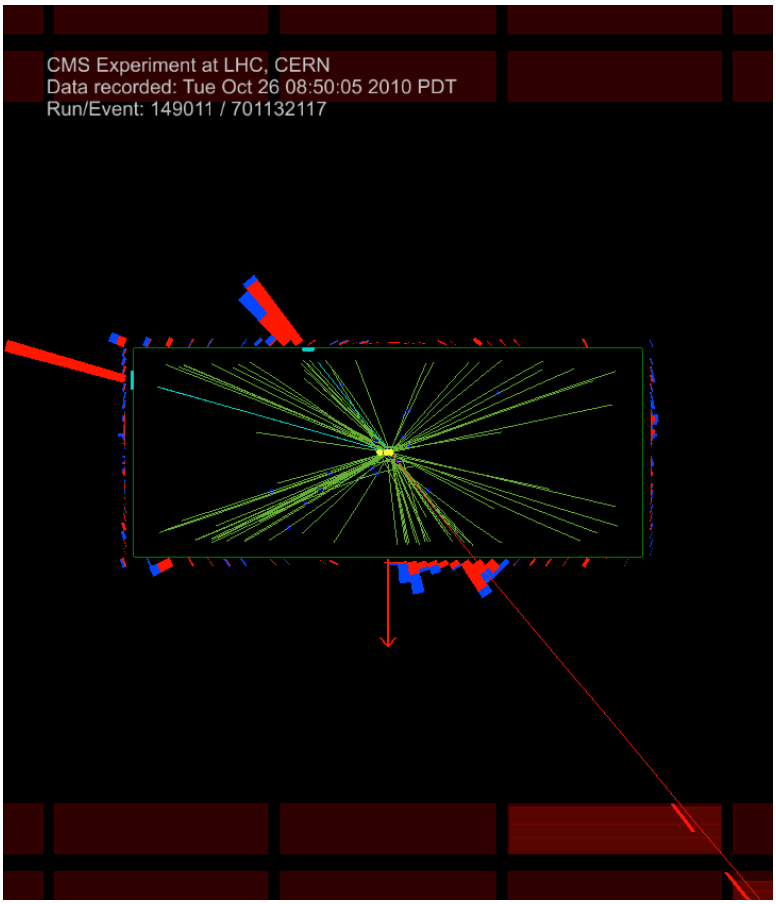

Figure 52: $e^+e^-\tau^+$ event

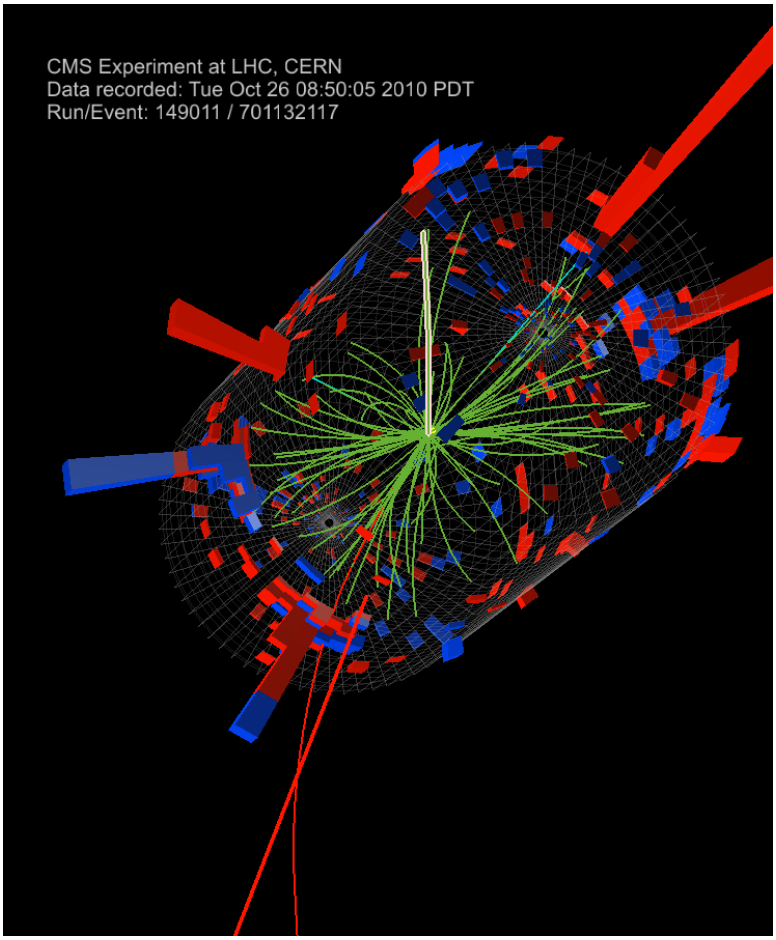

Figure 53: $e^+e^-\tau^+$ event. Highlighted track is lead track in 1-prong hadronic tau decay, with p_T = 7.3 GeV.

F.3 Candidate Trilepton + H_T Event #3

There was one flavorful event, having e, μ, and τ one each, although it has the trilepton charge of $|\Sigma Q_i| = 3$. The following table and event displays give the details of this event.

Event Type	$e^+\mu^+\tau^+$		
Run #	146804		
Event #	59056344		
H_T (GeV)	279.9		
pfMET (GeV)	129.0		
Lepton/Jet	p_T or E_T (GeV)	η	ϕ
e^+	32.7	-2.02	0.36
μ^+	16.7	0.57	1.69
τ^+(3-prong)	31.6	-0.91	-0.70
Jet 1	177.7	0.81	2.74
Jet 2	53.2	0.81	-1.37
Jet 3	49.0	0.13	2.09

Table 17: Trilepton + H_T candidate #3. The electron track has only 5 strip hits and appears to bremsstrahlung. One possibility is that this is a $t\bar{t}$ event with a sign-flip on the electron due to the mismeasurement.

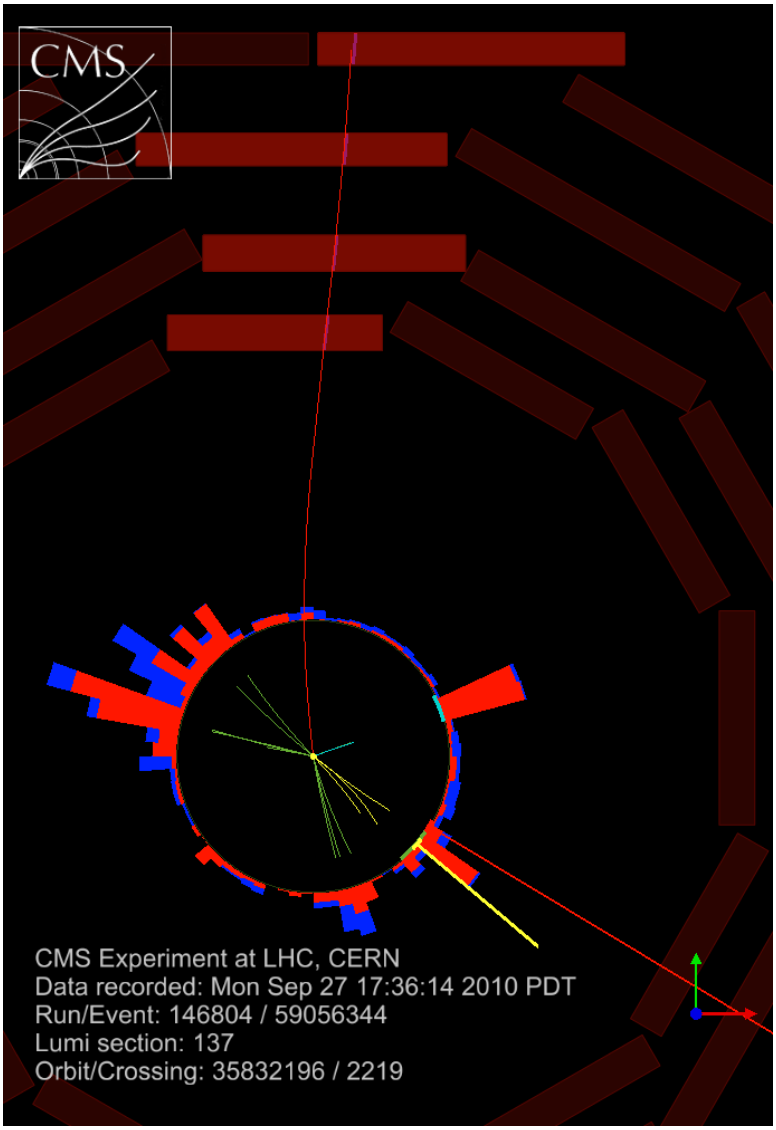

Figure 54: $e^+\mu^+\tau^+$ event.

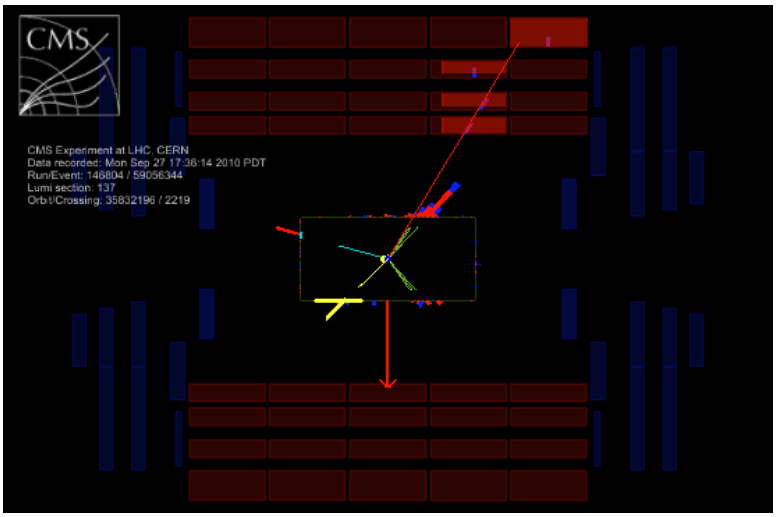

Figure 55: $e^+\mu^+\tau^+$ event

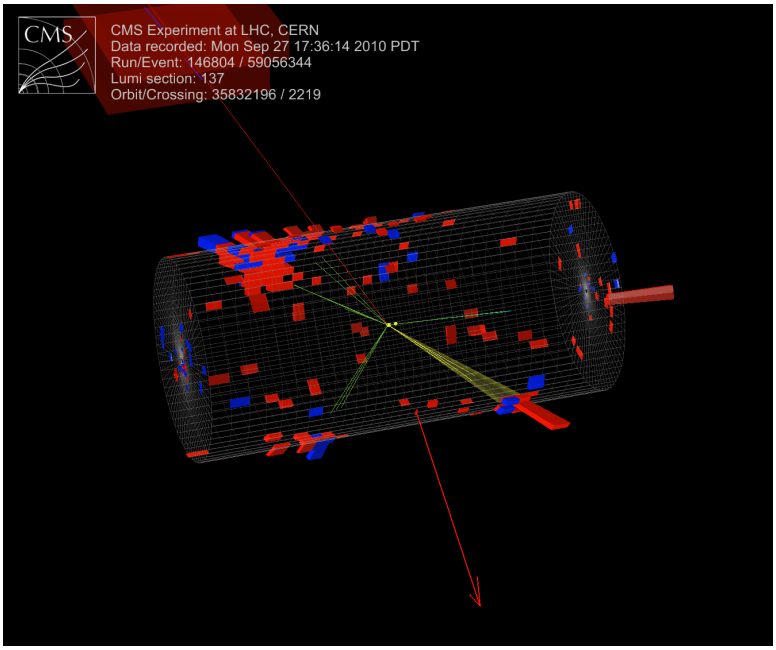

Figure 56: $e^+\mu^+\tau^+$ event.

List of Figures

List of Tables